ABSTRACT

Title of dissertation: SEARCH FOR GAMMA-RAY COUNTERPARTS OF GRAVITATIONAL WAVE EVENTS AND OTHER TRANSIENT SIGNALS WITH HAWC

Israel Martinez Castellanos
Doctor of Philosophy, 2019

Dissertation directed by: Professor Jordan A. Goodman
Department of Physics

In recent years we have seen major advances in multi-messenger astronomy. A milestone was achieved by identifying the electromagnetic counterpart of the gravitational wave event GW170817 detected by LIGO and Virgo. Similar efforts led to a set of neutrinos detected by IceCube to be associated with the blazar TXS 0506+056. Both demonstrate the potential of using multiple types of probes to study an astrophysical source.

The High-Altitude Water Cherenkov Observatory (HAWC), located in the state of Puebla, Mexico, is a wide field instrument ($\sim$2 sr) sensitive to very-high-energy gamma rays ($\sim$0.1–100 TeV) which can operate with a large duty cycle (>95 %). These characteristics make it well suited to look for transient events correlated with other astronomical messengers. In this work we present a maximum likelihood analysis framework developed to search and analyze signals in HAWC data of arbitrary timescales.

We apply this method to search for very-high-energy gamma-ray counterparts

of gravitational waves in short timescales (0.3–1000 s). We show that we would be able to either detect or meaningfully constrain the very-high-energy component of a gamma-ray burst within the binary neutron star merger horizon of current gravitational wave detectors if it occurs in our field of view. We did not find evidence for emission for any of the events analyzed. The source location of GW170817 was not observable by HAWC at the time of the merger.

We also set flux upper bounds for TXS 0506+056 during the periods when the neutrino flares were identified. For the flare between September 2014 and March 2015 these are the only available limits at very high energy, and are consistent with the low state in high-energy gamma rays reported by the Fermi-LAT Collaboration.

SEARCH FOR GAMMA-RAY COUNTERPARTS OF GRAVITATIONAL WAVE EVENTS AND OTHER TRANSIENT SIGNALS WITH HAWC

by

Israel Martinez Castellanos

Dissertation submitted to the Faculty of the Graduate School of the
University of Maryland, College Park in partial fulfillment
of the requirements for the degree of
Doctor of Philosophy
2019

Advisory Committee:
Professor Jordan A. Goodman, Chair/Advisor
Professor Peter S. Shawhan
Professor Julie McEnery
Professor Gregory Sullivan
Professor Suvi Gezari

Acknowledgments

This work, and in general going through graduate school, would have been either not possible, harder or less rewarding without the help of many people. Here I want to thank them, approximately in order of appearance.

A mi papá y mi mamá, quienes siempre me han apoyado en todo. Gracias.

A mis tías, tíos, primos y primas, una familia unida con la que siempre he podido contar. Gracias a todos.

A mis profesores, quienes me dieron las bases que necesitaba. Una mención especial a Carlos Hinojosa, Julio Gutiérrez y Raúl Hernández. Gracias.

A Kris, quien hace que cada día me sienta afortunado. Me es difícil imaginar haber vivido tan felizmente estos años de no haber compartido el día a día contigo. Gracias.

A Limón, quien quizá no tiene ni idea de cómo me ayudó, pero lo hizo. A él mejor le voy a dar una salchicha porque no sabe leer.

A la raza latina que me encontré por aquí. Luis, quien ha sido clave para que conociera a todos. Ana, Andrea, Ale, Alex, el otro Alex, Carlos, Dalia, Fernanda, Héctor, Maggie, Mónica, Pablo, Paco, el Wong y Yumhali, quienes siempre esta puestos para la pachanga y me hacen sentir más cerca de casa. Gracias a todos.

To the UMD Particle Astrophysics group. Especially to my advisor Jordan, my second advisor (in all but name) Andy, Colas and Josh, from whom I've learned many of the things that are part of this document; Liz, for her helpful comments on neutrino astronomy; and Naomi, who excels at her job and shielded me from

paperwork headaches. Thank you all.

To the entire HAWC Collaboration, past an present members. The analysis presented here represents just a small fraction of the efforts of more than a hundred people over several years. I want to especially mention Robert Lauer and Ignacio Taboada, who contributed directly to the follow-up of TXS0506+056 presented here. Thank you all.

And to my dissertation committee members, for their helpful comments and suggestions that improved this work. Thank you.

Table of Contents

List of Tables

List of Figures

List of Abbreviations

AGN Active Galactic Nucleus.

BBH Binary Black Hole.

BNS Binary Neutron Star.

CL Confidence Level.

CMB Cosmic Microwave Background.

Dec Declination.

EAS Extensive Air Shower.

EBL Extragalactic Background Light.

EM Electromagnetic.

FoV Field of View.

FSRQ Flat-Specturm Radio Quasar.

GRB Gamma-ray burst.

GW Gravitational Wave.

HA Hour Angle.

HAWC High-Altitude Water Cherenkov Gamma-ray Observatory.

HBL High-Frequency BL Lac.

HE High Energy.

HEALPix Hierarchical Equal Area isoLatitude Pixelization.

IGMF Intergalactic Magnetic Field.

ISM Interstellar Medium.

LBL Low-Frequency BL Lac.

NSBH Neutron Start - Black Hole Binary.

PE Photo-electron.

PMT Photomultiplier Tube.

PSF Point Spread Function.

PWN Pulsar Wind Nebula.

RA Right Ascension.

RPC Resistive Plate Counter.

SED Spectral Energy Distribution.

SNR Supernova Remnant.

SSC Synchrotron Self-Compton.

TOT Time over threshold.

TS Test Statistic.

VHE Very High Energy.

WCD Water Cherenkov Detector.

Chapter 1: Introduction

The sky as seen is gamma rays is rich in transient and variable phenomena occurring in a broad spectrum of timescales starting from a fraction of second to years. They are the result of extreme processes happening in our Universe. Short timescales, especially, serve as probes of high-density compact objects full of interesting physics.

Wide field of view (FoV) gamma ray observatories have proven valuable to advance our understanding of the emission mechanism of these kind of events. Having a wide field of view and high duty cycle allows both to notify other observatories based on self-triggered events and to have simultaneous observations available when external alerts are received.

This work presents various efforts to improve our understanding of such transient phenomena using data from the High-Altitude Water Cherenkov Gamma-ray Observatory (HAWC), sensitive to gamma-rays with energies from $\sim$100 GeV to 100 TeV. In particular we present a search for counterparts of gravitational waves and the neutrino source candidate TXS 0506+056, as well as a blind all-sky online search sensitive to flares in the timescale of hours to a few days.

This chapter contains an introduction of gamma-ray astronomy and explains

the motivation for this work. We discuss the known type sources we expect to detect, such as Active Galative Nuclei (AGN) and Gamma-ray Burst (GRB) progenitors. We also explain their connection with signals detected by gravitational wave and neutrino observatories, and the importance of such multi-messenger observations.

In Chapter 2 we explain the HAWC data-taking process. This includes a brief description of each component, the data-acquisition system, calibration and event reconstruction. The simulation of the detector is also discussed here as it is fundamental to extract physical information from the data.

Chapter 3 presents the method used for data analysis in this work, both to search for significant emission and to estimate physical parameters, such as flux. We describe how the data is aggregated into maps, the background is estimated and the source model is computed and fitted. This chapter also contains the search strategy used when either the location or emission time of the source is not known.

The maximum likelihood analysis presented here was developed to exploit peculiarities of the HAWC data in order to improve its sensitivity with respect to previous short timescale searches using a cut-and-count analysis. It is however also very general, and applicable to arbitrary timescales. It can then be used to search and study many different phenomena. In particular, presented in this work, we search for VHE gamma-ray counterparts of gravitational waves (Chapter 4) and from TXS 0506+056, a blazar which has been identified as a likely source of neutrinos detected by IceCube (Chapter 5).

Finally, in Chapter 6 we provide some insight on how to study other phenomena with this analysis, some of which are already being developed by members of

the HAWC collaboration. Different paths for improvement are also discussed.

1.1 Gamma-ray astronomy

The field of gamma-ray astronomy is intimately related to the study of the cosmic rays. Cosmic rays are charged particles of cosmological origin that were accelerated up to very high energies. Since Victor Hess' balloon experiments in between 1911 and 1913, where he measured a increase in radiation as a function of the altitude, cosmic rays have been detected over 10 decades in energy. Despite these efforts no single source responsible for this emission has been resolved by cosmic rays detectors. Magnetic fields bend the trajectory of charged cosmic rays such that not even the highest energy cosmic rays detected point back at their source with a sufficient accuracy to identify their their progenitors.

In this context, in 1958, Phillip Morrison published *On gamma-ray astronomy* [1], considered by some the seminal paper of gamma-ray astronomy. Since gamma rays are produced by nuclear and high-energy non-thermal processes where cosmic-rays interact, but are not deflected by magnetic fields, they can serve as probes of the sources and emission mechanisms of cosmic rays.

While the technology to detect gamma rays already existed, resolving individual cosmological sources was not easy. Gamma ray cannot be focused by reflection or refraction, with makes it hard to improve the signal to noise ratio. Cosmic rays themselves are in this case the primary source of background. Furthermore, the fact that the atmosphere is opaque to gamma rays forced observers to either use

satellites or to find other creative solutions.

Gamma-gamma ray astronomy has specialized into Low Energy (LE), from ∼0.1 MeV to ∼1 MeV; Medium Energy (ME), from ∼1 MeV to ∼30 MeV; High Energy (HE), from ∼30 MeV to ∼100 GeV; Very-High Energy (VHE), from ∼100 GeV to ∼100 TeV; and Ultra-High Energy (UHE), beyond 100 TeV. This division corresponds mostly to the energy window available to different detection techniques, described in Section 1.2, and there is some overlap between them. LE, ME and HE emission typically can be detected by space-based telescopes while the VHE and UHE energy window is available to ground-based telescopes, such as HAWC.

Although gamma rays are not deflected by magnetic fields, a problem that arises is that they can be absorbed by the medium between the source and Earth. This can be either material surrounding the source itself or in the interstellar medium. In the VHE regime the Extragalactic Background Light (EBL) is the main source of attenuation and considerably limits the volume that can be observed (see Section 1.3).

The first cosmological gamma-ray source to be identified was the Crab Nebula, by the Whipple telescope in 1980. It is a strong and mostly steady source that has become a reference source in the field, and is used for calibration by many experiments, including HAWC. Many other sources and phenomena have been observed in gamma rays since then. Sections 1.4.1 and 1.4.2 discuss two of these of particular relevance for this work, Active Galactic Nuclei (AGN) and Gamma-Ray Bursts (GRBs), respectively.

These types of sources have motivated the synergy not only between gamma

rays and other wavelengths, but also using other messengers besides photons. In the past decade is has become possible to detect neutrinos of cosmological origin, and in the last couple years gravitational waves as well. These messengers each carry unique information about the source that produced them. Section 1.5 briefly discusses some key aspects of neutrino and gravitational wave astronomy related to this work.

1.2 Gamma-ray detection

The techniques to detect gamma rays of astrophysical origin generally fall into two categories: direct and indirect. This refers as to whether the gamma rays interact with the components of the detector directly or the detector infers the existence of the primary gamma ray based on secondary particles produced after the interaction with an external target —e.g. the Earth's atmosphere—. The direct technique then correspond to balloon or spaced based telescopes while the ground-based experiments implement an indirect technique.

Coincidentally, indirect detection starts to be viable at around the end of the the energy range available for direct detection, making them quite complementary. The following sections briefly discuss the working principle of each technique, advantages and disadvantages, and mentions a (non-exhaustive) list of experiments that will serve as reference during the following chapters.

1.2.1 Direct detection

Gamma rays are quickly absorbed by the atmosphere, so in order to detect them directly one needs to go above it. The first cosmic gamma ray detectors used balloons, while current experiments are satellites.

Since gamma rays cannot be focused through refraction or reflection, the effective area is limited to the physical size of the detector. The natural size constraints of a satellite results in a effective area too small to detect the low flux values in the VHE range. Although there is some overlap with ground-based telescopes, direct detection is used for the low, medium and high energy range.

The energy range and type of detector is determined by the dominant process through which a gamma ray interact with matter. Above $\sim$30 MeV pair-production dominates, so the HE detectors work by converting a gamma ray into an electron-position pair and then tracking their trajectories. This is the case of the current Large Area Telescope (LAT), part of the Fermi satellite, and its predecessor the Energetic Gamma Ray Experiment Telescope (EGRET), part of the Compton Gamma Ray Observatory (CGRO) satellite [2].

These have proven very successful experiments. The gamma ray trajectory can be estimates based on the electron-position pair, with a angular resolution from $\sim$0.1° to $\sim$1°, depending on the gamma ray energy. The energy can be estimated to high precision (<10 %), thanks to a calorimeter that measures the energy of electron-position pair. The whole detector is surrounded by an anti-coincidence shield with detects charged particles, allowing it to operate virtually free of background. Also,

they have a large FoV ($\sim$2 sr) only limited by the physical aperture of the tracker.

Below $\sim$30 MeV Compton scattering dominates over pair-production. Telescopes in this regime have two main components: an upper low-Z tracker from which a gamma ray can easily Compton scatter an electron; and a lower high-Z detector that can serve both as a tracker and a calorimeter, completely absorbing the scattered gamma ray to measure its energy, and registering its position to reconstruct the primary direction. The direction of an individual gamma ray can only be constrained to a cone, with an opening angle which depends on the energy. The location of a source can be however determined using multiple events. The now retired Imaging Compton Telescope (COMPTEL), also part of CGRO, operated under this principle.

In the keV-MeV energy range gamma rays beams can be detected directly by arrays of scintillators. Three-dimensional arrays calculate the location of the source using triangulation. Examples are the Gamma-ray Burst Monitor (GBM), part of the Fermi satellite, and its predecessor the Burst and Transient Source Experiment (BATSE), part of the CGRO satellite. These experiments can have a 4π sr FoV (except for the portion blocked by the Earth) but have an angular resolution of a few degrees.

Another possibility to detect low-energy gamma-rays (and x-rays) is to use coded masks. These are grids with a known pattern which casts a shadow on the detector array which can then be processed to reconstruct the source location. Examples of experiments that utilize this technology are INTEGRAL (IBIS and SPI), Swift-BAT and AGILE-GRID. While this limits the FoV to 1–2 sr, they can

reach an angular resolution of $\sim 0.2^{\circ}$.

1.2.2 Indirect detection

While gamma rays cannot penetrate the atmosphere, at energies above $\sim 10\,\mathrm{GeV}$ the interaction produces enough secondary particles that the properties of the original gamma ray can be inferred from them. This is known as an extensive air shower (EAS), and is discussed in section 1.2.2.1.

One of the main challenges of indirect detection is that cosmic rays, which are more abundant by several order of magnitude than gamma rays, also produce EAS composed on their majority by the same particles as gamma-ray induced showers (electrons, positrons and gamma rays). Detectors make use of slight differences in the characteristics between a gamma-ray and a cosmic-ray showers to try to identify them. These are commonly called gamma-hadron separation techniques.

There are two main types of indirect detection techniques: Imaging Atmospheric Cherenkov Telescopes (IACTs) *photograph* the evolution of the shower as it moves through the atmosphere (Section 1.2.2.3); and Extensive Air Shower Arrays such as HAWC detect the secondary particles at ground level taking a transverse *snapshot* (section 1.2.2.4). The former typically have a greater sensitivity, and better energy and angular resolution. The latter on the other hand have a wide FoV, can operate almost continuously and usually can reach higher energies.

Since Cherenkov radiation plays a very important role for many ground based detectors, including HAWC, we include a short description in Section 1.2.2.2.

1.2.2.1 Extensive air showers

The first interaction of a high-energy gamma ray with the atmosphere is usually through pair production. The gamma ray interacts with an air nucleus and typically generates an electron-position pair. The production of other leptons such as muons are highly suppressed. The electron and positron then interact with another air nucleus, mostly through bremsstrahlung, generating additional gamma rays. These gamma rays again pair-produce, rapidly multiplying the number of particles and generating an extensive air shower. Figure 1.1 contains a schematic of a gamma-ray shower.

The process continues until the resulting secondary particles have a low enough energy ($E \approx 84\,\mathrm{MeV}$) that the absorption through ionization processes of electrons and positrons begins to dominate over gamma-ray production through bremsstrahlung. At this point the shower has reached the maximum number of particles, which then starts to decrease. This is called shower maximum, and depends on the energy of the primary particle, as shown in Fig. 1.2.

This relatively simple process results in a smooth and azimuthally symmetric lateral profile. This was estimated analytically by K. Kamata and J. Nishimura [6] and, after an approximation made by K. Greisen [7], is know as the NKG function:

$$\rho(r) = \frac{N}{r_M^2} \frac{\Gamma\left(4.5 - s\right)}{2\pi\Gamma\left(s\right)\Gamma\left(4.5 - 2s\right)} \left(\frac{r}{r_M}\right)^{s-2} \left(1 + \frac{r}{r_m}\right)^{s-4.5}, \tag{1.1}$$

where ρ is the electron density, N is the total number of electrons, r is the perpendicular distance to the shower axis, r_M is the characteristic length of Molière scattering

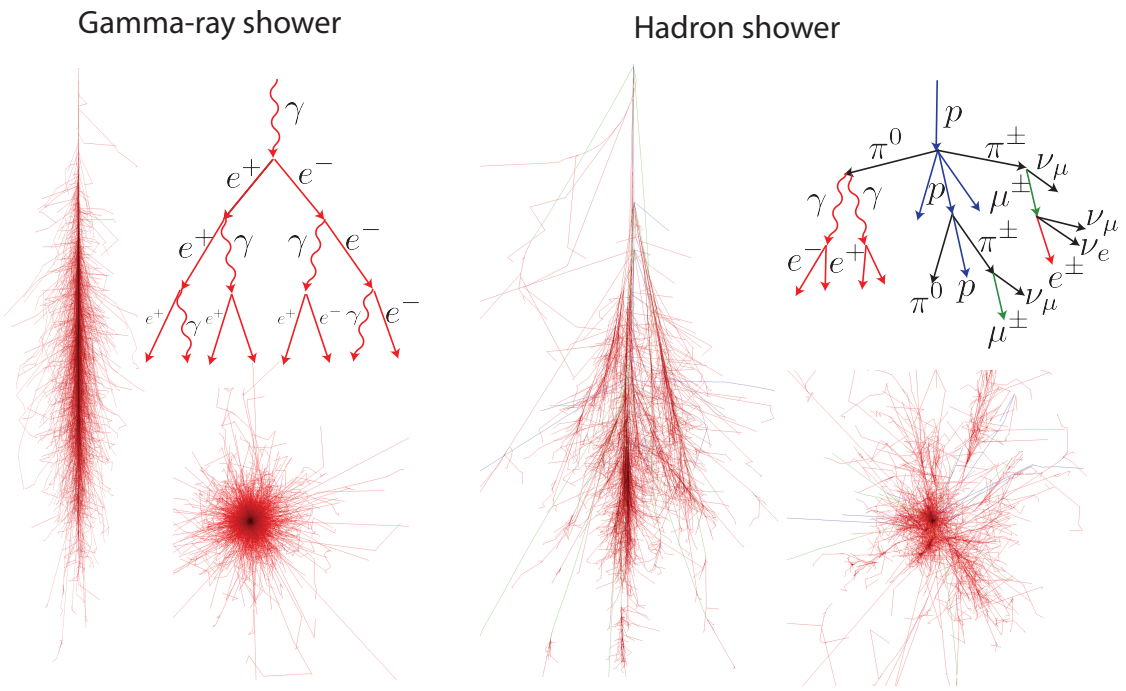

Figure 1.1: Depiction of a shower generated by a gamma ray (left) and a proton (right). For each, the simulated showers are projected in the planes parallel (left) and normal (lower right) to the shower axis. In the upper right there is a schematic of the main processes generating secondary particles. The tracks of electrons, positrons and gamma rays are colored in red, muons in green, hadrons in blue. The shower images were generated using CORSIKA by F. Schmidt and J. Knapp [3].

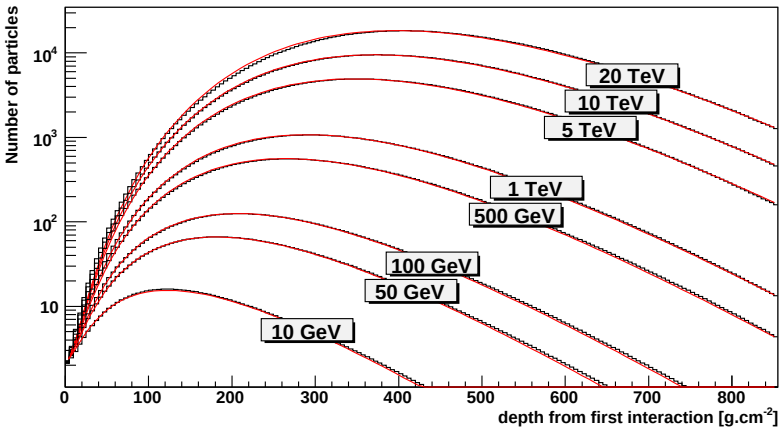

Figure 1.2: Number of charged particles in the shower after the first interaction versus the interaction depth, for various values of the primary gamma ray energy. Reproduced from [4]. For reference, at 4100 m.a.s.l., HAWC is at a vertical depth of 620 g/cm^2 [5].

and s is the *age* parameter. This parameter s is related to the development of the shower, $s = 1$ at shower maximum and increases continuously.

Hadron induced showers, on the other hand, are far from simple. During the first interaction with an air nucleus the main processes are [8]

$$\begin{aligned} p + p &\rightarrow p + \pi^{\pm} + \pi^0 \\ \pi^0 &\rightarrow 2\gamma \\ \pi^{\pm} &\rightarrow \mu^{\pm} + \nu_{\mu} \\ \mu^{\pm} &\rightarrow e^{\pm} + \nu_{\mu} + \nu_{e}\,, \end{aligned} \tag{1.2}$$

where p represents one or more hadrons or nuclei, and the difference between neutrino and anti-neutrino was omitted. There can be multiple pions generated in an interaction, as well as kaons and other particles, although pions dominate. The

resulting nuclei continue to interact with other air nuclei, multiplying the number of particles, until they fall below the energy required to produce a pion. See Figure 1.1 for an schematic.

First, note that gamma rays are produced from π^0 decay, and electrons and positrons from $\pi^{\pm}$ decay. Each of this —the former being dominant— initiates an electromagnetic shower in the same way a primary gamma ray would do it. Hadron induced showers represent then the main background for indirect detection experiments, but fortunately there are differences that allows us to distinguish them to some degree.

The first difference is in the electromagnetic component of the hadron induced shower itself. While the gamma-ray induced shower is azimuthally symmetric and smooth, a hadron shower is irregular and has multiple "sub-showers". This is caused by the different hadronic particles that move far from the axis of the shower before generating an electromagnetic shower. Note also that the resulting electromagnetic component is the result of a superposition of sub-showers with various degrees of development.

Hadronic showers are also distinguished from gamma-ray shower by their muon content, produced by $\pi^{\pm}$ decay. While gamma-ray showers have a non-zero chance of containing muons, their production is highly suppressed. Muons can travel all the way to the ground without decaying, generating a clear signature in the detector that can be used to identify them as background events.

1.2.2.2 Cherenkov radiation

Cherenkov radiation is produced when a charged particle travels in a dielectric medium faster than the speed of light in that medium. As it moves, the charged particle polarizes the surrounding medium, followed by relaxation. If it travels at low speed this happens slowly enough that it does not result in a measurable emission, while if it travels faster than the speed of light a shock wave is obtained.

Using geometrical arguments we can obtain that the angle of emission, θ, with respect to the charged particle trajectory, traveling at a speed βc, is related to the refraction index of the medium, n:

$$\cos\theta = \frac{1}{\beta n}\,. \tag{1.3}$$

We can see that there is a speed threshold for this emission to occur, which corresponds to $\cos\theta = 1$. Since the total energy of a particle is $E = mc^2/\sqrt{1-\beta^2}$, then the energy threshold is

$$E_{min} = \frac{mc^2}{\sqrt{1-\frac{1}{n^2}}}\,. \tag{1.4}$$

For an electron ($m = 0.51\mathrm{MeV/c^2}$) in water ($n \approx 1.33$) the threshold is $E_{min} = 0.8\mathrm{MeV}$. In air ($n \approx 1.0003$) we have $E_{min} = 21\mathrm{MeV}$. While Cherenkov light is emitted over a broad band, the refraction index depends on the light frequency. For frequencies higher than a certain value the refraction index becomes less than unity and no more Cherenkov emission is generated.

Lastly, we can also see that there is a maximum angle, $\theta_{max} = \arccos(1/n)$, corresponding to particle traveling at the speed of light in vacuum. For water this

is θ_{max} =41° and for air θ_{max} =1.4°.

1.2.2.3 Imaging Atmospheric Cherenkov Telescopes

Charged particles in the extensive air shower generate Cherenkov radiation as they travel in the atmosphere. While this emission is dim, it can be observed from the ground and used to record a picture of the shower, from which we can then estimate the direction. The instruments that use this technique are known as Imaging Atmospheric Cherenkov Telescopes (IACTs).

IACTs consist of a large segmented mirror which focuses the received Cherenkov photons into a camera. The camera trigger needs to be fast, as the whole emission arrives in a time window of a few nanoseconds. While looking for very short timescale emission allows the telescope to reduce various sources of noise, the observations still need to be taken under dark conditions and clear skies. Their duty cycle is of the order of 10–15 %.

Since the Cherenkov cone in air is narrow ($\sim$1.4°), the shower can be completely recorded in the camera as an slightly elongated ellipse (except for extremely energetic events). Since the angle from the center of the field of view to the shower axis is known —i.e. equal to the Cherenkov angle— this is enough to reconstruct the direction of the primary particle. This results in a very good angular resolution ($<$0.1°). The downside is that the field of view of the telescope is only a few degrees wide.

The total amount of light recorded is proportional to the energy of the shower.

Since they are built at an altitude below the shower maximum, the whole development of the shower is recorded and the shape can be further uses to improve the energy estimation. The energy resolution is typically about 15 %.

The background rejection is based on the shape of the image recorded from the shower. Gamma-ray showers look like a smooth, thin and regular ellipse, while hadron showers look irregular and broader. In addition, the Cherenkov light produced by muons that passed near the detector leave a characteristic ring pattern in the cameras which can be used as a discriminator. Good background rejection, angular resolution and effective area —approximately the area illuminated by the Cherenkov cone— make these telescopes very sensitive detectors.

This technique was pioneered by the Whipple telescope in the '70s. Even though a single telescope is able to reconstruct the direction of the shower, the advantage of having a stereoscopic view using an array of detectors was demonstrated by HEGRA in the late '80s. Current IACTs include MAGIC, HESS, VERITAS and FACT.

1.2.2.4 Extensive Air Shower Arrays

So far we have discussed direct detection —when the primary gamma ray interact with the detector itself— and indirect detection by IACTs —where a picture of the extensive air shower is taken using the Cherenkov photon generated by secondary particles. Another option is to detect the secondary particles themselves, which is performed by EAS arrays, such as HAWC.

EAS arrays, which are also used by experiments primarily interested in cosmic rays, consist off a series of detectors laid on the ground sensitive to particles with energies typically greater than 1MeV. One of the challenges is that while these experiment typically extend over at least several thousand of square meters —depending on their energy range—, they need to be built a high altitude, otherwise the air shower dies out before reaching the ground.

Various type of technologies have been used to detect these secondary particles. CYGNUS, one of the pioneer experiments of this technique, used a series of scintillators paired with photomultipliers (PMTs). It also incorporated a muon detector, which helped to identify hadron showers. Tibet-AS used a similar scintillator array, and incorporated an array of muon detectors underground. ARGO-YBJ utilizes an array of Resistive Plate Counters (RPCs), parallel conductive plates filled with gas and held at high voltage such that discharge is produced near the crossing of an ionizing particle.

Milagro —and Milagrito, its predecessor— used a series of PMTs submerged in a water pond which detected the Cherenkov radiation generated by charged particles in the shower after they interacted with the water. Gamma rays quickly pair produce and also contribute to the observed Cherenkov radiation. Milagro is the predecessor of HAWC, discussed in detail in Chapter 2, which uses the same mechanism although with a modular design of separated water tanks instead of a pond.

All of these detectors operate in a light-tight environment, eliminating external sources of light, including the Sun. The interaction of secondary particle with clouds and rain, as well as with passive elements of the detector, is negligible. This allows

them to operate with a theoretical 100 % duty cycle, limited only by maintenance.

Good timing is critical. The direction is reconstructed using the arrival time of the secondary particles, effectively mapping the shower front which at first order is a plane. The angular resolution is $\sim 0.1^\circ$ at best, usually greater than IACTs. However, the advantages of this technique are a high duty cycle and a wide field of view, limited only by the increasing thickness of the atmosphere and the decreasing effective area with respect to the zenith angle.

Muons, present for the most part only in hadronic showers, play a big role in background rejection. Muons can either be identified by dedicated detectors or by the signature they leave in the array —usually a large energy deposition observed by only a few detectors—. The pattern of the footprint left by the shower can also be used to do background rejection, with gamma-ray showers having smooth and symmetric lateral particle distribution, while hadronic showers being irregular. At low energies not many particles make it to the ground, and there are only a few muons —easy to miss—, making background rejection difficult. IACTs typically have better sensitivity over most of their energy range. However, at energies above ~ 10 TeV EAS arrays begin to excel.

Lastly, the energy of the primary particle is proportional to the amount of energy deposited in the detector. This needs to be corrected mainly by the zenith angle —the atmosphere thickens—, and by the shower stage of development. The latter refers to when the primary particle underwent the first interaction, a value that can be derived based on the lateral distribution and is related to the shower age in Eq. 1.1.

1.3 Extragalactic Background Light

The Extragalactic Background Light (EBL) is the set of remnant photons from star formation and emitted from Active Galactic Nuclei (see Section 1.4.1). This radiation ranges from UV to infrared, and represents the main source of attenuation of VHE photons, which interact with EBL through photon-photon pair-producing interactions. Although this process cross section might be small, it becomes important for extragalactic objects due to the long distance that must be traveled.

Figure 1.3 provides the attenuation factor versus energy and redshift[1]. It can be seen that, even at the start of the VHE window, EBL severely constrains how far we can observe with a detector like HAWC. It also limits our ability to set meaningful upper-limits when the redshift of a source is not known. Once the redshift is known the intrinsic spectrum can be derived from the measured spectrum. At about $z > 0.5$ even the 100 GeV photons, about HAWC energy threshold, start to be severely attenuated, making it hard to provide useful results.

[1]The redshift, z, is expressed as the fractional change in frequency caused by the expansion of the Universe. Up to a few hundred megaparsecs ($z \lesssim 0.1$) there is a linear relation between redshift and distance, $D = zc/H_0$, where c is the speed of light and H_0 the Hubble constant ($c/H_0 \approx$4200 Mpc [9, 10]). While higher redshift values still imply longer distances, the relation is not linear and depends on the evolution of Hubble constant during the history of the Universe.

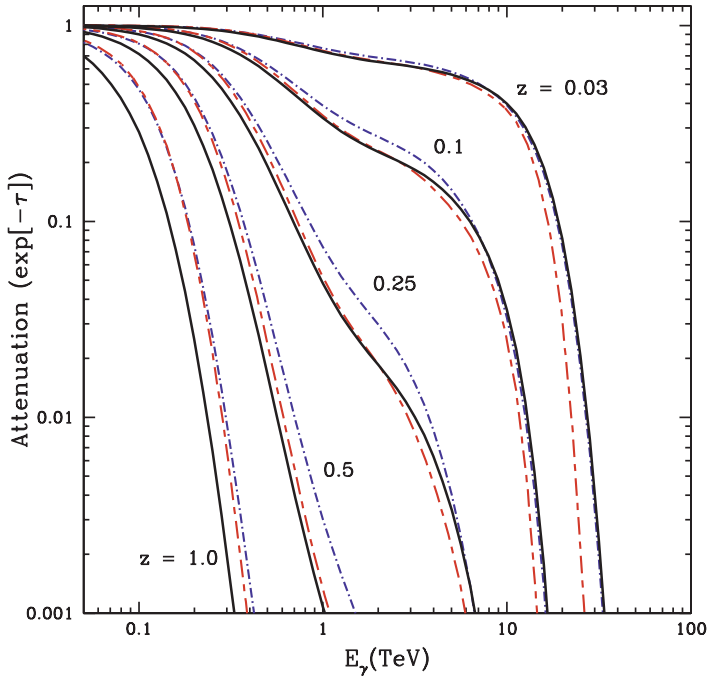

Figure 1.3: EBL attenuation versus energy for various redshifts for three different models. Reproduced from [11].

1.4 Sources of gamma-ray signals

There are several types of cosmological gamma-ray emitters and signals. By no means a comprehensive list, in the VHE range we have for example binaries — stars orbiting compact object, such as a neutron star or a black hole—, supernovae, supernova remnants (SNRs), pulsars, pulsar wind nebulae (PWN), active galactic nuclei (AGN) and gamma-ray bursts (GRBs).

We discuss here AGN and GRBs, which are directly related to this work. Although very different in size, both are are composed of highly relativistic jets resulting in non-thermal emission, powered by a central engine containing a compact object such as black hole. They are capable of generating very fast transients or highly variable signals which can potentially be observed in VHE gamma-rays.

1.4.1 Active Galactic Nuclei

Active Galactic Nuclei includes various categories historically classified as different objects, such as quasars, blazars and radio galaxies. Today it is believed that they are all generated by emission powered by the supermassive black holes in the center of galaxies, with different observed properties depending on the viewing angle.

Figure 1.4 provides a schematic of an AGN. It consists off a accretion disc or material orbiting around a supermassive black at the center of a galaxy, powering two opposite relativistic jets along the axis of rotation. An observer along the jet would report a blazar while when viewed at an angle a radio galaxy is observed.

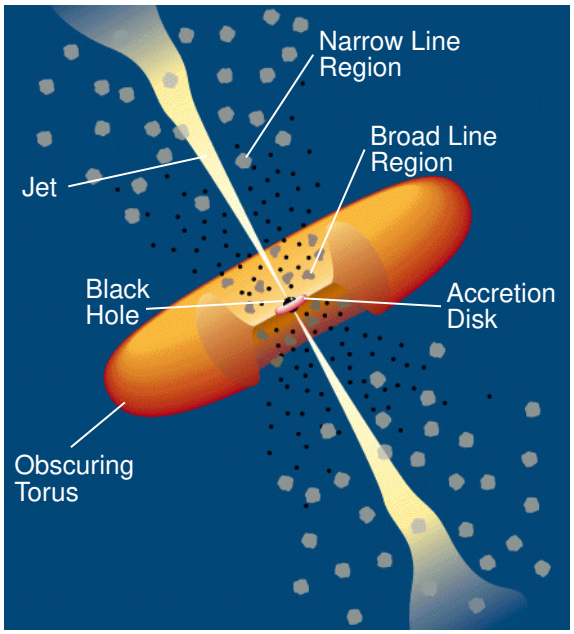

Figure 1.4: Schematic representation of an AGN, see text for description. Reproduced from [12].

Different classification exists depending on whether narrow line emission can be observed —presumably from low density gas clouds far from the center— or there is only broad line emission —presumably from high density clouds near the core, which would be absorbed for an observer viewing from the side by an obscuring torus—.

Gamma-ray emission is observed from blazars. These can be further divided into BL Lac objects —named after the prototype object BL Lacertae—, and Flat-Spectrum Radio Quasars (FSRQs). The main distinction is that emission lines can be seen in FSRQs objects but not in BL Lacs. BL Lacs are further subdivided into Low-frequency BL Lacs (LBLs) and High-frequency BL Lacs (HBLs), depending on whether they were detected with radio or x-rays. Most of the AGN detected in VHE

gamma-rays are HBLs.

Markarian 421 and Markarian 501 are two prominent HBLs. Markarian 421 was the first extragalactic source to be detected in VHE gamma rays, and Markarian 501 the first one to be detected in VHE before being detected in HE gamma rays. These sources are nearby (z=0.031 and z=0.034, respectively), highly variable and can reach fluxes several times the Crab Nebula.

Figure 1.5 shows a multi-wavelength lighcurve for Markarian 421, showing its variability and correlation between VHE gamma-rays and x-rays. There are indications that the VHE gamma-ray spectrum hardens during flares [13]. Figure 1.6 shows the average Spectral Energy Distribution (SED) across several decades of energy. This shows a *double-humped* structure, with one peak in x-rays frequencies and another peak in gamma rays. The variability, double-humped structure of the SED and correlation between these two peak are general properties of blazars and some of the main constrains for emission mechanism models.

While the details of the models vary, there is general consensus that gamma rays are emitted somewhere along the jet, which is composed of bulk material moving at relativistic speeds. This means that due to Doppler boosting the energies of the photons we observe are considerably higher than the energies in the rest frame of the bulk material. It also means the observed luminosity is boosted due to relativistic beaming. This observations explain why the gamma rays can escape from the source, as they would otherwise pair-produce through interactions with other photons.

The emission mechanism involves accelerating charged particles which then result in gamma-ray emission. It is belived they are accelarated either by shocks in

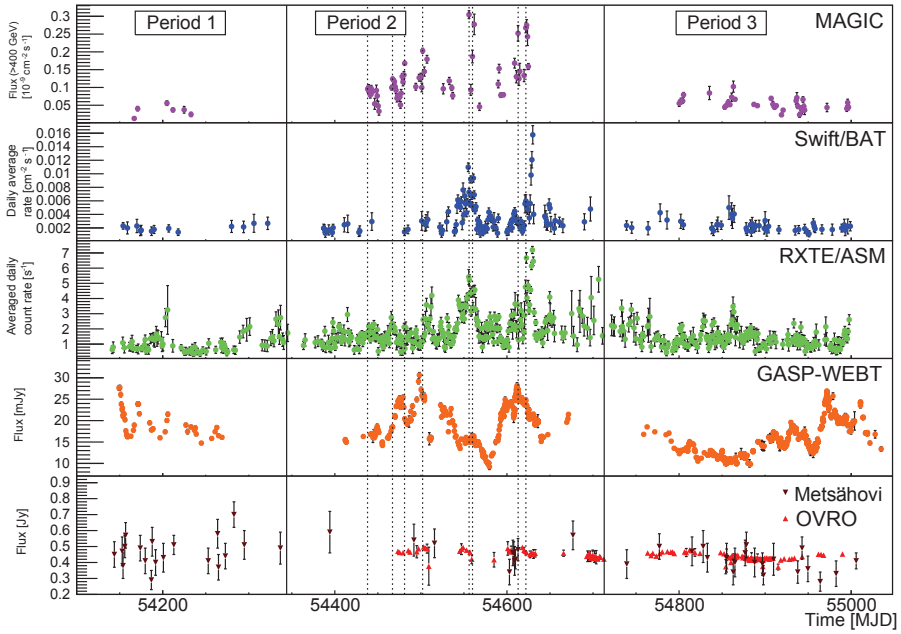

Figure 1.5: Markarian 421 lightcurve for various wavelenghts: VHE gamma-rays (MAGIC), x-rays (Swift/BAT and RXTE/ASM), optical (GARM-WEBT) and radio (Mets ahovi and OVRO). This shows high variability and correllation between x-rays and gamma rays. Reproduced from [14].

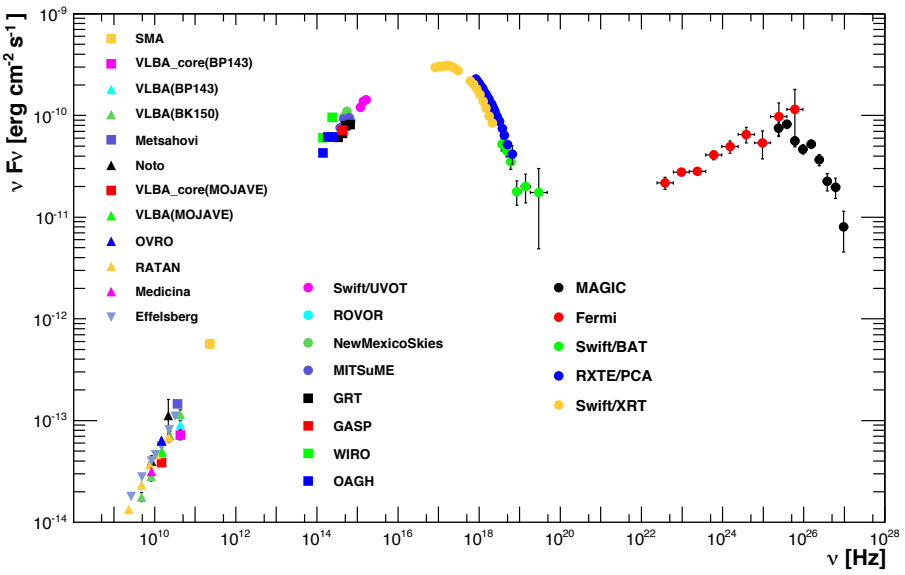

Figure 1.6: Markarian 421 spectral energy distribution using time average data from various experiments. The *double-humped* structure with peaks in x-rays and gamma-rays if clearly visible. Reproduced from [15].

the jet or by magnetic reconnection [16]. In the former case, particles are accelerated when sections of the jet traveling a different speed collide with each other and produce shock fronts that particles can cross several times, gaining energy on average during each crossing. On the latter case, particles are accelerated when magnetic fields reconfigure, producing the movement of charged particles.

Depending of which charged particles compose the main population responsible for the emission, the acceleration models can be classified as leptonic or hadronic. In the leptonic model electrons are accelerated an then undergo synchrotron radiation in the magnetic field of the jet; this is associated with the first peak present in the double-humped SED. Synchroton photons serve as targets for other accelerated electron, producing the gamma rays we observe in the second peak through inverse

Compton scattering. This is known as the Synchrotron Self-Compton emission (SSC).

In hadronic models protons conform the main population of accelerated charged particles. Protons can interact with low energy photons and, through a delta resonance, produce pions. Neutral pions convert to gammas and charged pions convert to neutrinos and muons. The latter can then decay into electrons and more neutrinos. This is known as $p\gamma$ interactions:

$$\mathrm{p} + \gamma \rightarrow \begin{cases} \mathrm{p} + \pi^0 \\ \qquad \pi^0 \rightarrow 2\gamma \\ \mathrm{n} + \pi^+ \\ \qquad \pi^+ \rightarrow \mu^+ + \nu_\mu \\ \qquad\qquad \mu^+ \rightarrow e^+ + \nu_e + \bar{\nu}_\mu \end{cases} \tag{1.5}$$

Note that, due to isospin conservation, the number of neutral pions produced by this interaction is twice the number of charged pions. Also, the energy carried by a muon neutrino is approximately half of the gammas, for each pion [17]. Additionally, not shown here, the neutron can decay and generate another neutrino, although of significantly lower energy.

Protons can also interact with gas, that is other protons and nuclei, also producing pions which can decay into similar products. This set of processes, known as pp interactions, are the same as the ones that generate hadronic extensive air showers (Eq. 1.2). The pp contribution is usually assumed small based on the proton density of the jet [18]. Whether we have pp or $p\gamma$ interaction, the low energy of

peak in the double-humped SED is explained by synchrotron emission of secondary particles in the resulting cascade.

Hadronic models are attractive because they can explain both the cosmic rays and the gamma rays that we observe. However, it is generally hard to disentangle leptonic from hadronic models using gamma-ray observation alone, as both can produce the double hump SED (albeit with some differences in shape and relative normalization).

Note that only the hadronic models predict neutrinos, and that these should be correlated with gamma rays. Neutrino sources have not been clearly identified yet though, since they are very hard to detect. This is the reason combined gamma ray and neutrino observations are promising as a way to understand the source of cosmic rays and AGNs. In Section 5 we search for VHE gamma rays from TXS 0506+056, a neutrino source candidate from which a high energy neutrino was detected while it was undergoing a flare in gamma rays.

Simultaneous observations between VHE gamma rays and other wavelengths have greatly helped to constrain the emission model of blazars. For example, simultaneous observations of x-ray flares and VHE gamma rays constrain the magnetic field strength and bulk Lorentz factor, as only certain values allow the gamma rays to escape. Also, the presence and delay between flares for photons of different energies illuminates the possible structure of the jet, for example the sometimes observed VHE flares without a counterparts flare in x-rays —called *orphan flares*— suggest more than one emission region [19]. Simultaneous observations between HE and VHE gamma rays can also constrain the modeling. For example, in the SSC model

high energy electrons release energy more rapidly, resulting in shorter timescale variability in VHE than in HE.

Simultaneous observation are usually hard to obtain though. The well established IACT detectors (see section 1.2.2) used to detect VHE gamma-rays, although very sensitive, have a small FoV. This result in the telescopes using their limited resources on sources from which a flaring state is expected based on observation from other experiments. This bias has been minimized though by pursuing observation campaigns with regular observations or by dedicating telescopes —e.g. the FACT experiment— to observing daily a pre-defined list of sources. The large FoV of HAWC allows it to monitor the sky in an unbiased manner, looking for flares and with the possibility of triggering other experiments.

1.4.2 Gamma-ray bursts

Gamma-ray bursts are brief, intense and not repetitive flashes whose SED peaks from hundreds of keV to a few MeV. They were first detected by the Vela satellites [20], which where designed to detect the resulting radiation from nuclear tests which were banned during the Cold War. They reported 16 bursts with durations from 0.1 s to 30 s on the 0.2–1.5 MeV range with a fluence of $\sim 1 \times 10^{-5}\,\mathrm{ergs\,cm^{-2}}$ to $2 \times 10^{-4}\,\mathrm{erg\,cm^{-2}}$.

It was quickly noted that their arrival direction was distributed isotropically, as depicted by detections of the current experiment Fermi-GBM in Figure 1.7a. While their integral flux distribution hinted a homogenous distribution[2], it was not clear if

[2]The argument goes: $dN \propto r^2 dr$, where N is the number of GRBs and r is the distance. Also,

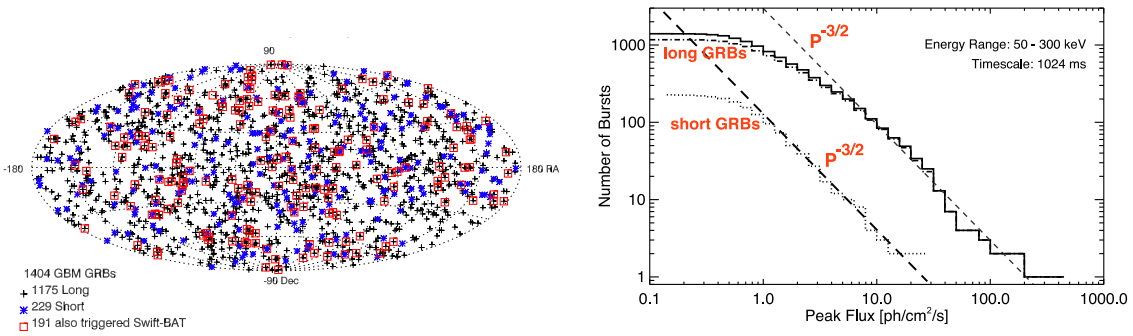

(a) (b)

Figure 1.7: **(a)** Sky localization of GRBs detected by GBM. GRBs are distributed isotrotropically. **(b)** Integral distribution of GRBs peak flux. A power-law with slope -3/2 is included, which is the expectation for objects homogeneously distributed in Euclidean space. Figures reproduced from [21]

the deviation from this hypothesis on the lower end was caused by detector effects and high redshifts, or because their distribution was not really homogenous. These observations pointed to an extragalactic origin, but because of their high luminosity their energetics were hard to explain.

We now know they are of extragalactic origin thanks to rapid follow-ups in x-rays and optical bands, such as the ones performed by BeppoSAX, which allows for a better localization and to measure the redshift of their host galaxies. It was also observed that after the initial burst in gamma rays on the order of seconds —called prompt emission—, there is a long decaying emission in other wavelengths, lasting days or even months —called afterglow.

GRBs are now routinely detected in HE gamma rays, currently by Fermi-LAT

$s \propto 1/r^2 \rightarrow ds \propto dr/r^3$, where s is the detected flux. We then have $dN \propto s^{-5/2} \rightarrow N(>s) = s^{-3/2}$.

and previously by EGRET. The HE emission was found to last about an order of manitude longer than the keV-MeV range emission [22]. The HE lightcurve usually shows a high rise with a short delay with respect to keV burst start, typically of a few seconds but sometimes considerably longer, and is followed by a long decreasing tail. Sometimes there is a dimmer emission before the main pulse, known as a precursor, which is sometimes also observed in the keV-MeV range.

The Fermi-LAT spectral fits for many GRBs do not show indication of a cutoff in energy. High energy photons up to 95 GeV (from GRB 130427A) have also been observerd (128 GeV corrected to the source reference frame based on its redshift) [23]. This suggests the emission can extend up to the VHE range, at least for some events.

Detection in the VHE range has proven to be difficult though. While it might be due to an intrinsic cutoff in the spectrum in most events, the volume the VHE experiments can see is severely limited by EBL attenuation (see Section 1.3). Milagrito reported a 3σ post-trials observation from GRB 970417a [24]. Recently, the MAGIC collaboration reported a clear detection from GRB 190114C in a 20 min observation started 50s after the Swift-BAT trigger time [25]. Also, the HESS collaboration reported detection of GRB 180720B [26] from observation started $\sim$10 hr after the Fermi-GBM trigger. Note that these two recent observations are still unpublished results, so details are lacking at the time of this work.

Regardless of what the GRB progenitor is, the consensus is that emission comes from a relativistic jet. Following similar arguments as for AGN (see Section 1.4.1), a large bulk Lorentz factor alliviates the energy requirement the high observed

luminosity imposes, and allows HE gamma rays to escape which would otherwise be absorbed at the source by photon-photon interactions. This means that the GRBs are only detected from a narrow cone along the axis of the jet. Based on afterglow measurements the opening angle is estimated to vary between $\sim 3^\circ$ and $\sim 30^\circ$ [27]. In this model the afterglow emission is caused by the external shock of the jet with the interstellar medium (ISM).

Most of the current models explain the emission through the collision of shells of matter in the jet traveling at different speed. This creates shocks, which accelerate charged particle which most likely emit gamma-rays through synchroton radiation, although inverse Compton scattering may play a role as well [28]. This is known as the *fireball model*. The jet is believed to be powered by a central engine with a compact object in the center, such as a black hole.

The time duration distribution of GRBs is bimodal, as shown in Figure 1.8a. This suggests there at at least two difference classes of object that are GRB progenitors. The difference between these two groups is further accentuated by observing a correlation between the duration and the steepness of the SED, as shown in Figure 1.8b, which has led to the classification of GRBs into short-hard and long-soft.

Long GRBs are believed to be produced by supernovae, which is supported by multiple associations [29] and characteristics of their host galaxies [30]. The progenitors of short GRBs have long believed to be binary neutron star (BNS) mergers, proposed by Paczynski [31] and Eichler, et al. [32] based on energetics and a match between the BNS merger rate and the observed short GRB rate. While this hypothesis was supported by afterglow observations that locate possible counterparts

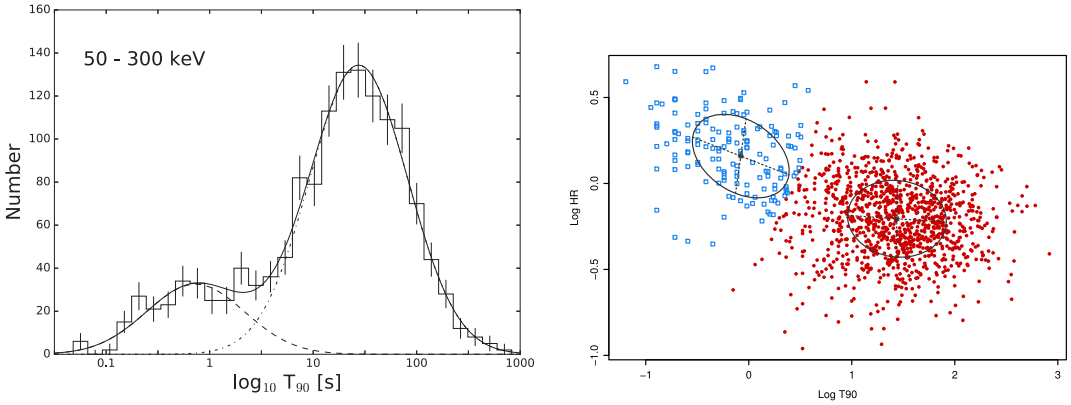

(a) (b)

Figure 1.8: **(a)** Duration distribution of detected GRBs by Fermi GBM. T90 represent the time where 90% of the counts arrived. **(b)** Hardness ratio vs T90. The hardness ratio is the ratio between the counts in the 10-50 keV and the 50-300 keV bands. These plots show a distinction between short-hard and long-soft GRB populations. Figure reproduced from [21]

outside the host galaxies [33] —expected by the *kick* resulting from the supernova explosion during the formation of one of the neutron stars composing the binary—, it was not until recently that a decisive observation was made.

BNS mergers should release energy in many forms besides gamma rays. As depicted in Figure 1.9a, there is an isotropic electromagnetic emission from the interaction of the ejected material with the ISM and from radioactive decay of heavy elements generated from the material in the neutron star. Gravitational waves are also expected (see Section 1.5.2) to be emitted in all directions, as shown in Figure 1.9b. The multi-messenger and multi-wavelength detection of a BNS merger was long expected and finally became a reality with GW 170817 [34].

GW 170817 and its corresponding EM observation proved the great potential of multi-messenger and multi-wavelength observations to understand this type of phenomena. With the goal of contributing with measurement during the prompt emission in VHE gamma-ray, and possibly helping other EM experiments performing observation —e.g. by reducing the location uncertainty—, we run a follow-up of gravitational waves as discussed in Section 4.

1.5 Multi-messenger astronomy

Most of the information we have obtained from extrasolar objects has been through light of different wavelengths. In the 20th century there were a couple of exceptions, mainly cosmic rays from the Sun and neutrinos from supernova SN 1987A. In recent years there has been a tremendous increase in coordinated efforts

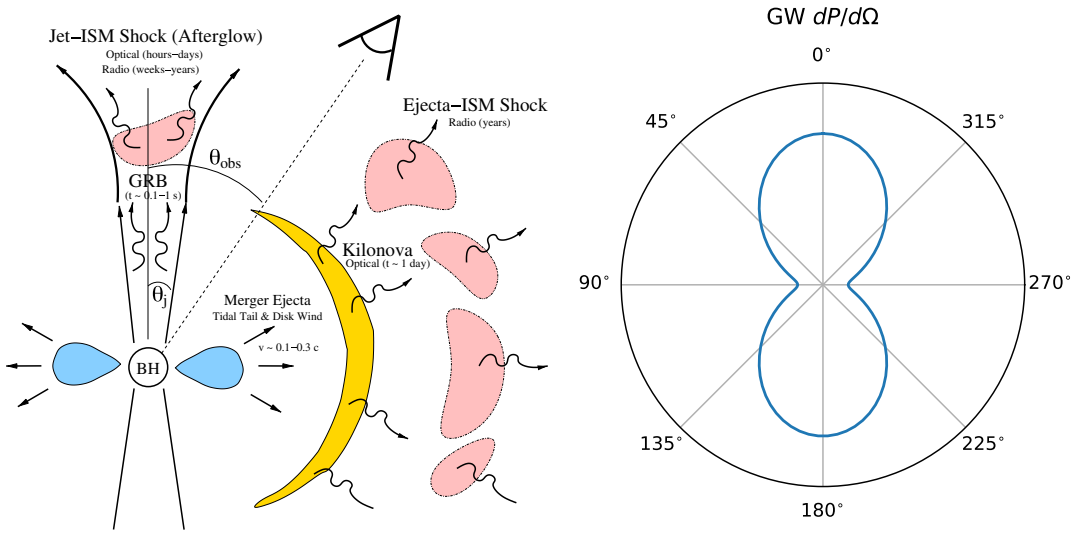

(a) (b)

Figure 1.9: **(a)** Potential electromagnetic emission after a BNS merger. Note the dependence on the viewing angle and the different emission timescales for each wavelength. Reproduced from [35].**(b)** Power emitted in gravitational waves per solid angle as a function of the angle from axis of rotation. See for example [36] for a derivation.

to simultaneously observe the same object using multiple types of messengers, for which there are already successful examples.

The connection between some gamma-ray sources and their counterparts in neutrinos and gravitational wave signals was introduced in Section 1.4. Here we present a brief description of key aspects of the detection of this messengers that are relevant for this work.

1.5.1 Neutrino astronomy

Neutrinos of cosmological origin are mainly produced by the interaction of accelerated protons with background radiation ($p\gamma$ interactions) or with gas (pp interactions). As can be seen in Eq. 1.5 and 1.2, respectively, both of these sets of processes result in gamma rays as well, and open the possibility to detect both types of messengers from a given source, such as AGN and GRB progenitors. Furthermore, while gamma rays can be attenuated either at the source or during their travel —e.g. through EBL, Section 1.3—, neutrino interactions are very weak, allowing us to look further in distance or closer to the interior of a source.

Neutrinos interacting weakly is also the same reason why they are hard to detect. Current astrophysical neutrino detectors consist of a large volume of naturally occurring water that is instrumented to detect light from Cherenkov photons generated by secondary particles produced when a neutrino interacts with a nucleus. For example, IceCube makes use of the sheet of ice at the south pole and the ANTARES detector is located in the Mediterranean Sea.

Neutrinos can interact with a nucleus via the Z boson (neutral current) or through the W boson (charged current). Both of them scatter the nucleus and result in a hadronic shower. Charged current interactions in addition result in a charged lepton which can then be tracked in the detector by means of the Cherenkov photons it generates. While long tracks allow to reconstruct the direction to within $\sim 1^\circ$ [37], the energy is hard to estimate when the event is not fully contained in the detector.

Due to neutrino oscillation we receive all three flavors of neutrinos, and therefore all three flavors of leptons are generated. However, electrons scatter easily and taus decay rapidly, so most of the tracks are due to muon neutrinos. As seen in Section 1.2.2.4, cosmic rays also produce muons when interacting with the atmosphere, making them the main source of background. One way to reduce this is to use the Earth as a muon shield and select only upward traveling neutrinos.

Another possibility is to only select events with a starting track inside the detector. The outer layer of the array is used as a veto, since it would detect light from a muon generated by cosmic rays. This allows to detect down-going neutrinos as well as neutrinos of other flavors by mean of the hadronic shower produced by the scattered nucleus. When no track is identified they are called *cascade events*, and while they allow to estimate the energy relatively well —the detector fully contains the events and act as a calorimeter—, their direction can only be reconstructed to within 10°-20°.

Both of these methods leave an irreducible background composed by the neutrinos produced also in cosmic-ray induced air showers, known as atmospheric neutrinos. However, the spectrum of atmospheric neutrinos falls much more rapidly

versus energy than the spectrum of neutrinos of cosmological origin. This makes detected neutrinos more likely to be of cosmological origin the higher their energy is. The existence of a cosmic neutrinos excess above 30 TeV was first reported by IceCube in 2013 [37].

Although the existence of cosmic neutrinos is clear, it has not been possible to resolve any individual source with the angular resolution and sensitivity of current detectors. One possibility to remedy this is to look for space and time correlations with other experiments. The first evidence of the identification of a source was a product of such an effort: the detection of the IceCube-170922A neutrino, consistent with the direction blazar TXS 0506+056, also detected in an enhanced state in gamma rays by Fermi-LAT and MAGIC [38]. In Chapter 5 we look for emission from this source using HAWC data.

1.5.2 Gravitational wave astronomy

Gravitational waves (GWs) are disturbances in the curvature of the spacetime. They have been long predicted to exist since a wave equation is a solution of Einstein field equations. They manifest as a change of proper distance in the plane transverse to the direction of propagation.

Currently operating GW observatories measure this change of distance by means of kilometers-long interferometers. Due to the nature of the gravitational waves amplitude —i.e. a strain $s = \Delta L/L \sim 10^{-20}$ or less— these must be extremely sensitive detectors, and are therefore subject to multiple sources of noise. Strong

non-Gaussian noise, known as glitches, can sometimes mimic GW signals. Although many can be identified by requiring a detection by more than one detector with a physical time delay between them, some still need human intervention to distinguish them from real events.

There are three currently operating GW observatories which have detected gravitational waves: LIGO, with one detector in Hanford, Washington, and another in Livingston, Louisiana; and Virgo, located near the city of Pisa, Italy. LIGO made the first detection of a gravitational wave in 2015 [39].

The collaboration between different detectors is crucial for GW astronomy. The sky localization cannot be determined with only one detector, it is rather calculated through triangulation based on multiple detectors. Using two detectors the sky localization is constrained to a great circle in the sky, and can be further refined to about half a great circle based on the relative sensitivity versus the incoming direction —known as *antenna patterns*—. This results in an typical localization uncertainty of $\sim 1000\,\mathrm{deg}^2$. Using a third detector can further constrain the sky localization down to $\sim 10\,\mathrm{deg}^2$ [40].

Gravitational waves are produced by any object with a changing quadrupole moment over time, the simplest case being a rotating binary system. These objects need to be very massive in order to have a chance to detect them. Candidates are binary black holes (BBHs), binary neutron stars (BNSs) and a neutron star-black hole binaries (NSBHs). Supernovae might also result in a spinning object that have a quadrupole moment, although the waveform of the GW signal is not clear.

LIGO and Virgo are sensitive to the last moments of these binaries around the

time they merge. For binary systems, the signal produced in the detector is known, as is a function of the mass of each object, the distance from Earch, the sky location and the relative orientation with respect to the detector —an possibly the spin of each component—. This allows to use templates and infer these parameters from the observed inspiral waveform [41]. Besides the approximate sky localization and distance, the nature of each component can also be inferred. Since the maximum mass of neutron star is most likely $<3M_{\odot}$ [42], while the mass of a blackhole is usually $>5M_{\odot}$ [43], for most events we can conclude if at least one of the components of the binary was a neutron star [44]. All these are important pieces of information used by observers looking for electromagnetic counterparts.

BBH mergers are not expected to produce electromagnetic emission, except under some special circumstances [45], as there is no surrounding material left. Binaries that involve neutrons stars, on the other hand, are believed to be progenitors of short GRBs, as explained in Section 1.4.2, motivating multi-messenger follow-up campaign of gravitational waves by telescopes in all wavelengths and neutrinos. Supernovae, connected to long GRBs, are also of great interest. During such campaigns large FoV instruments can play an important role since GWs are for the most part not very well localized. These efforts led to the observation of the electromagnetic counterpart of GW 170817 from radio to gamma-ray [34]. No emission in VHE was detected though.

A couple points are worth noticing about joint observation of gravitational waves and gamma rays. First, as depicted in Figure 1.9, while gravitational wave are emitted in all direction, the emission of gamma rays is collimated and restricted

to a narrow cone. There is then the possibility of detecting gravitational waves without any gamma-ray counterpart.

Second, the current gravitational wave detectors will be able to observe BNS mergers up to ∼400 Mpc ($z \sim 0.09$) [46] [3]. Note that the neutron stars mass distribution is very narrow, $\sim 1.4 M_{\odot}$ [48], and that the rate of NSBH mergers is much lower than NSNS mergers [49]. This means that, if there is gamma-ray emission from a gravitational wave event, it will be most likely barely attenuated by EBL (see Section 1.3), making gravitational waves a good candidate to look to VHE gamma-ray emission. Note that the bulk of the GRBs occurs at rather large redshifts, and most of the VHE emission is attenuated. This motivated a dedicated analysis to look counterparts of gravitational waves with HAWC, presented in Section 4.

1.6 Summary

We presented a short review of gamma-ray astronomy. We saw how different types of instruments complement each other, either by observing different energy ranges or by making use of their strengths —e.g. some might have better sensitivity and while other have a wider field of view—. Two types of transient gamma-ray sources were discussed: Active Galactic Nuclei and Gamma-ray Bursts. They are both characterized by their relativistic jet emission and either variable or transient

[3] The range, defined as the distance at which a BNS merger can be observed by LIGO after averaging in direction and relative orientation, is of ∼200 Mpc (at design sensitivity). The horizon, defined as the maximum distance a BNS merger can be observed, that is for an event at zenith and oriented along the axis of rotations, is a factor of 2.26 larger [47].

nature. The study of such phenomena have the potential to benefit from observations by wide field of view instruments. It was also explained how they are connected to gravitational wave and neutrino astronomy. These are the main motivations for this work.

Chapter 2: The HAWC observatory

The High Altitude Water Cherenkov (HAWC) observatory is a gamma-ray detector sensitive from ∼100 GeV to ∼100 TeV. It is located on the flanks of the Sierra Negra volcano, in the state of Puebla, Mexico (18° 59′ 41″ N, 97° 18′ 27″ W), at an elevation of 4100 meters above sea level. It consists of an array of 300 Water Cherenkov Detector (WCDs)[1], covering an area of 22 000 m^2. WCDs are light-tight tanks, each containing approximately 2×10^5 liters of water and equipped with 4 Photomultiplier Tubes (PMTs).

HAWC operates under the same working principle of an extended air shower array described in Section 1.2.2.4. When the secondary particles in the shower front plane interact with the water in the WCDs, discussed in Section 2.2, they generate Cherenkov radiation. Some of these Cherenkov photons are then detected by the PMTs at the bottom (a *hit*), whose operation is explained in Section 2.3. The charge and timing of each hit is recorded (Section 2.4) and calibrated (Section 2.5),

[1] At the time of this writing the HAWC detector has been upgraded with another 345 small WCDs with a single PMT each, known as *outriggers*. These were placed in the surroundings and are expected to help to reconstruct events that land outside the detector, mostly events with a primary particle energy greater than 10 TeV. This improvement is not yet fully integrated with the main array and was not used in this work.

and then used as a snapshot of the shower which enable us to reconstruct back the direction of the primary particle (Section 2.6).

Both cosmic and gamma rays produce particle showers that trigger the detector. The vast majority of shower are due to cosmic rays, and therefore they are the dominant background. Differences in the pattern left by cosmic-ray versus gamma-ray shower are exploited to reduce this background, as explained in Section 2.6.3.

Finally, simulation is required to relate the observed number of detected events to physical values. The several steps performed in a Monte-Carlo simulation are described in Section 2.8, which involve the simulation of the shower evolution through the atmosphere, the propagation of the shower particles the arrived to the ground through the different components of the detector and the signals measured by the PMTs.

2.1 The HAWC array

The HAWC WCDs are arranged as shown in Fig. 2.1b. The specific arrangement in rows and aisles is motivated to facilitate deployment and maintenance. The data acquisition system is located approximately at the center of the array. Cables carrying high voltage and analog signals radiate from here to each of the channels.

The number of tanks and active channels has changed over time. Part of the advantages of using tanks —i.e. as opposed to a pond, as in its predecessor Milagro (see Section 1.2.2.4)— is that data could be taken during construction,

which facilitated the developing of analysis and calibration methods at an early stage. Also, channels can be taken down because of maintenance or identified issues with negligible impact to data taking.

The data used in this work starts on November 26th, 2014, at which point 240 tanks and 800 channels were active. Since May 2015 the number of active tanks and channels has remained fairly constant at ∼290 tanks and ∼1100 channels.

2.2 Water Cherenkov Detectors (WCDs)

The Water Cherenkov Detectors (WCDs) are each of the detector units composing the HAWC array. The goal of each WCD is to detect secondary particles from Extended Air Shower (EAS) with a precise timing. Each unit consists of a steel tank filled with water, which serves as the target material that convert the energy of the secondary particles into Cherenkov photons, and 4 PMTs at the bottom, which are the sensitive components which detects low energy photons (see Section 2.3). A schematic is shown in Figure 2.2.

The tanks were built in place out of steel plates. The water is contained by a light and water tight lining, with a hatch at the top for easy deployment and maintenance. At the top of the tank there is a spherical dome to avoid rain accumulation. The interaction of all of these passive components with the particles detectable at ground level is negligible.

Each tank is 5 m tall and has a diameter of 7.3 m. The water level is approximately 4.5 m high while the top of the PMTs are about 45 cm above the ground. The

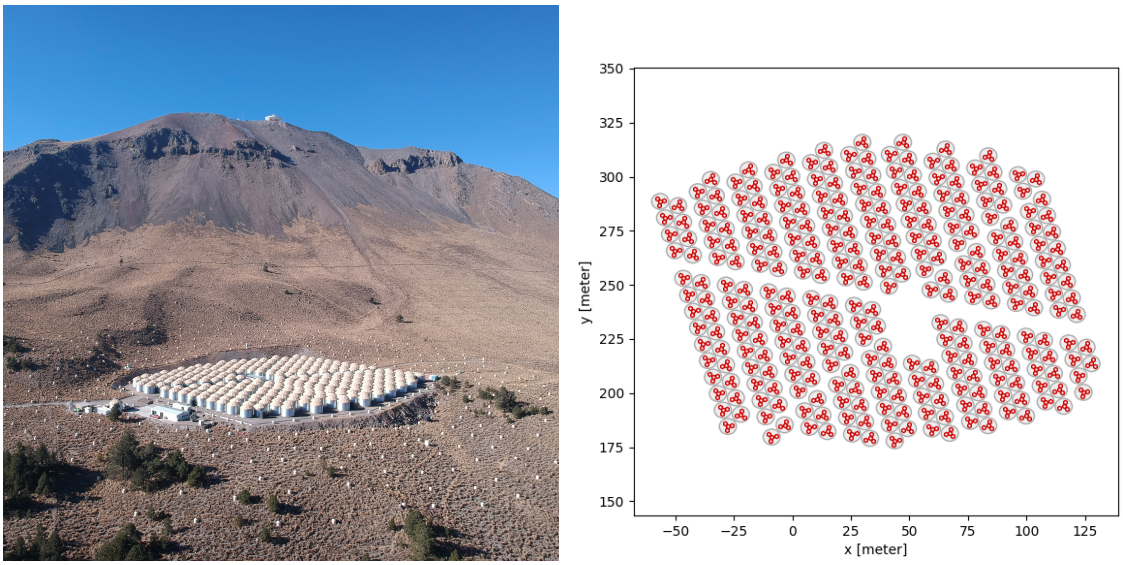

(a) (b)

Figure 2.1: **(a)** Recent picture of HAWC, showing in the background the Large Millimeter Telescope at Sierra Negra. The small WCDs surrounding the main array will help the event reconstruction, however they are not fully integrated with the main array at the time of this work and therefore were not used. [credit: Eleazar Sandoval] **(b)** HAWC main array arrange. Positive x and y axes are align with East and North, respectively. Gray circles correspond to tanks, each containing 4 PMTs, depicted as red circles. Except for the PMTs, this figure is drawn to scale. The empty space in the center contains the data acquisition system. The whole array is mostly level, with a difference in height of only a few centimeters between opposite sides.

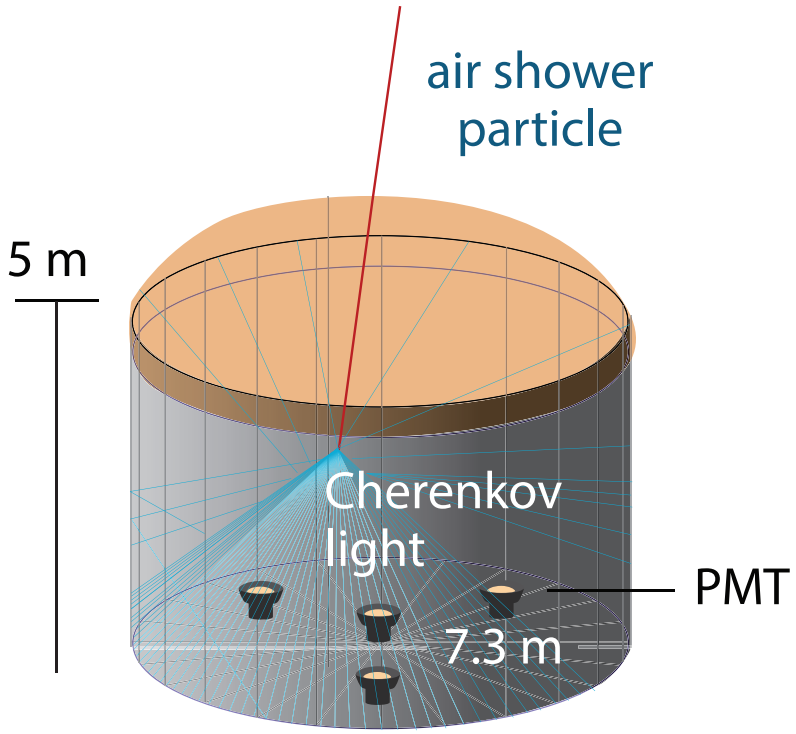

Figure 2.2: WCD schematic depicting the arrival of an air shower particle. The charged particle (or gamma ray, which quickly pair produce charged particles) generates Cherenkov photons when it interacts with the water, which are then detected by the PMTs. The WCD is light and water tight, and has a spherical dome to avoid rain accumulation.

water is purified before filling the tank which decreases absorption and scattering of Cherenkov photons, and perhaps more importantly, prevents mineral deposition or biological growth on the face of the PMTs (decreasing their efficiency).

The height was chosen such that the energy of electrons and positrons (and gamma rays, which after entering the water rapidly either Compton-scatter electrons or pair-produce) part of the EAS secondary particles reaching the detector level would be completely absorbed before reaching the PMTs, which both ensures a good measurement of the energy reaching the ground and prevents these particles from hitting or passing near a PMT. If they hit or pass near a PMT it would result in a strong and localized signal, something characteristics of muons since they pass through the WCD without stopping. As will be explained in 2.6.3, HAWC background reduction algorithm relies heavily on the identification of muons produced by hadronic showers and heavily suppressed in gamma-ray shower. And electron or positron hitting or passing near a PMT could then lead the misclassification of a gamma-ray shower as a hadron shower.

The diameter was chosen such that for a vertical charged particle arriving at the center of the tank, all the PMTs would be illuminated uniformly. For a height of 4 m and considering than the Cherenkov cone in water has an opening of $\sim$41.2° (see Section 1.2.2.2) this illuminates the bottom with a radius of 3.5 m, approximately the radius of the tank.

The plastic liner, or bladder, contains the water and prevents external light from producing noise signals in the PMTs. This allows HAWC to operate with a high duty factor (>95 % of the time), independently of the Moon or Sun light. The

interior of the bladder is black, preventing light from bouncing back and ensuring that the light detected by the PMT is direct, improving the timing. This is also motivated by fact that, as will be explained in Section 2.4, HAWC measures deposited charge in the PMTs not by measuring the waveform, but by measuring time-over-threshold. Reflected light could deform the assumed waveform and produce spurious measurements.

Lastly, at the bottom there is one high quantum efficiency R7081 Hamamatsu PMT in the center and three equidistant R5912 Hamamatsu PMTs 1.85cm from the center. The working principle of a PMT is explained in Section 2.3.

2.3 Photomultiplier Tubes (PMTs)

Photomultipliers tubes (PMTs) are devices that allow detection of extremely low levels of light, even single photons. They produce relatively low noise levels and can have a large collection area. HAWC uses PMTs to detect Cherenkov photons produced by secondary particles (MeV electrons and gamma rays) when they interact with the water. Using them we can measure the number of photons that arrive at the PMTs and the time when this happens with sub-nanosecond accuracy.

Figure 2.3a has an schematic depicting of the working principle of a PMT. The first interaction occurs with the photocathode, a thin conductive layer. Through the photoelectric effect, a photon is converted into an electron (commonly called photoelectron). This material sets the photon wavelength range over which the PMT is sensitive, as shown in Figure 2.4a

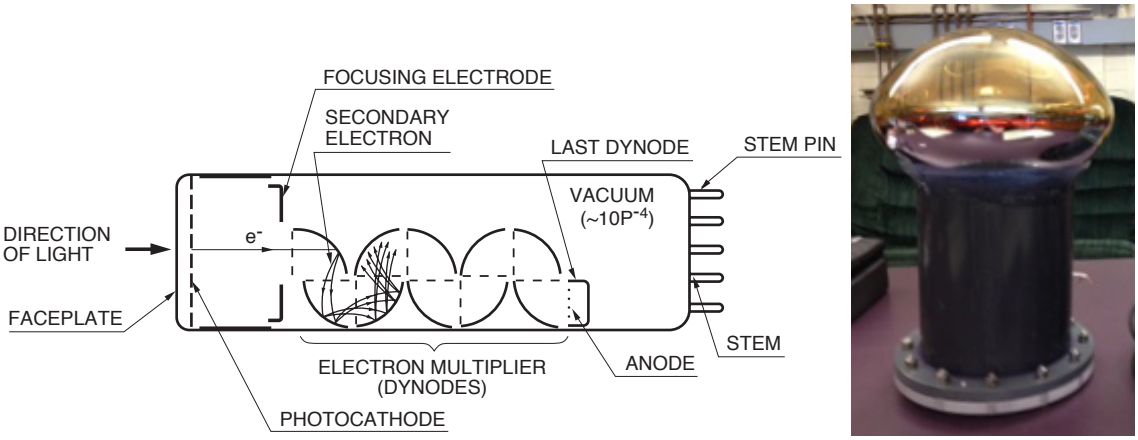

(a) (b)

Figure 2.3: **(a)** PMT schematics. See text for the working principle description. Reproduced from [50]. **(b)** Photo of the R7081 Hamamatsu PMT showing the large photocathode area (253 mm in diameter) to increase the collection of photons. The base of the PMT is sealed before placing it in the tanks to avoid the contact with water. The R5912 Hamamatsu PMT has a similar shape, although with a smaller diameter (202 mm) [credit: Miguel Mostafá]

This photoelectron is accelerated and focused due to strong electric fields into an electrode set at a higher voltage, called dynode. Through secondary emission, this electron produces another pair of electron after the impact with the first dynode, which are then accelerated and focused into the next dynode, set at a higher voltage. This multiplicative process creates an avalanche of electrons than are collected by the last electrode, the anode, producing a small signal in the form of a current that is analyzed as explained in Section 2.4. This charge amplification, called *gain*, is of the order of 10^7 for the PMTs used in HAWC.

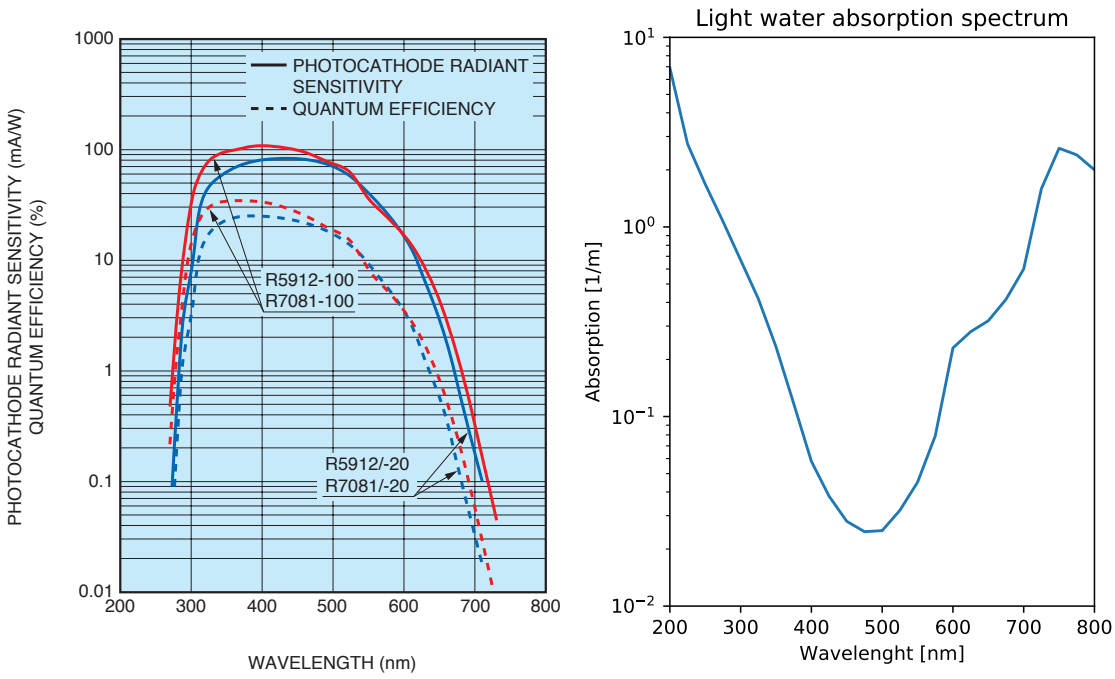

(a) (b)

Figure 2.4: **(a)** PMT photocathode efficiency versus incident photon wavelength. Quantum efficiency is defined as the number of photoelectrons emitted from the photocathode divided by the number of incident photons. Radiant sensitivity is the photoelectric current from the photocathode, divided by the incident radiant power at a given wavelength. Reproduced from [51]. Compare this with **(b)**, the absorption coefficient versus wavelength [52], the distance at which the intensity is decreased to $1/e$. While Chrenkov radiation is a broad band emission, the wavelengths the PMTs are sensitive to match approximately the wavelength that can travel the characteristic length of the tank.

2.4 Data acquisition

During data acquisition we gather the output signal from the anode of the PMT and process it in such a way that allows us to compute the charge and timing of the pulse. HAWC electronics characterize the PMT pulses by the time spent over certain voltage threshold (time-over-threshold, or TOT). Although the current is not integrated over time to obtain the charge, there is a strong correlation between TOT and the total charge —or more specifically, the logarithm of the charge—, which allows us to estimate it.

HAWC electronics use a set of two thresholds at different voltage values, shown schematically in Figure 2.5. These low and high thresholds are set approximately equal to the peak you would expect by a pulse from 0.25 PEs and 5 PEs, respectively. We refer to the time-over-threshold for these two voltages as LoTOT and HiTOT, respectively. Although in principle only one threshold would suffice, the LoTOT of hits with multiple PEs can be significantly affected by the early or late arrival time of a single photon. HiTOT allows a more precise estimate of the charge in those cases and avoids missadentifying a small hit as big one.

The digital output of the DAQ corresponds then to the points in time each pulse crosses the low and high discriminating voltages. This is done with a time-to-digital converter device (TDC), which combines the output of both thresholds into a single digital signal (see Figure 2.5). This values are then related to physical properties of the hit: the light level —i.e. the number of PEs detected— and the timing —i.e. the time at which the first photon arrived to the photocatode—. This

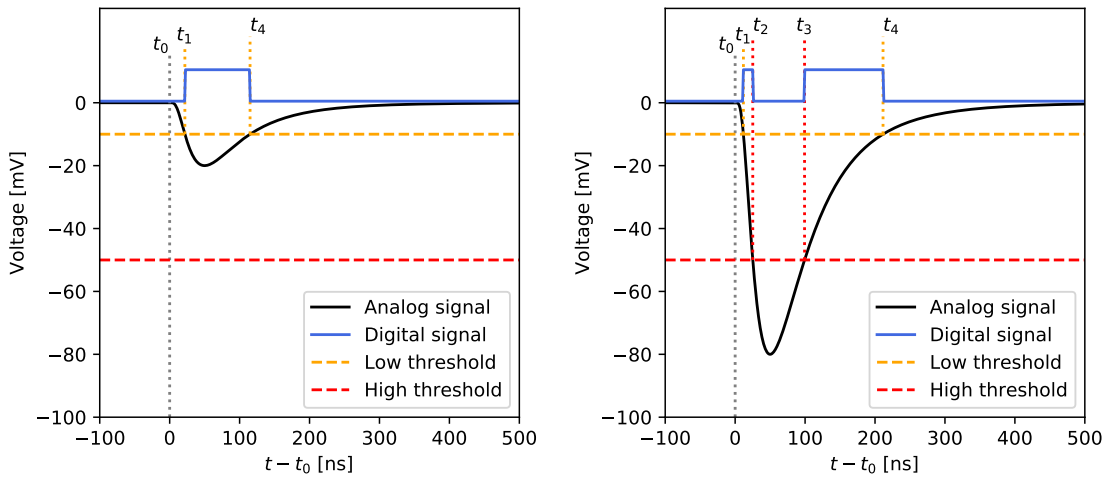

(a) (b)

Figure 2.5: **(a)** Representation of the digital output of the discriminator when an idealized pulse crosses the low threshold value. This is called a 2-edge hit: the first edge is during the rising part of the pulse (labeled t_1) and the second during the falling (t_4). LoTOT $= t_4 - t_1$. Here t_0 represents the time at which the idealized pulse begins to rise. The difference between t_0 and t_1 is called slewing. **(b)** Represents the case of a larger hit, in which the pulse surpasses the high voltage discriminator. This is known as a 4-edge pulse, since the outputs of the low and high threshold are subtracted by the TDCs to produce a single digital signal. HiTOT $= t_3 - t_2$. The fact that the pulses are not symmetric allows us to distinguish two 2-edge hits —-which result in two similar length square pulses- from a single 4-edge hit —which results in a short square pulse followed by a longer square pulse—. Only about 1% of the 4-edge hit events are misidentified as 2 2-edge hits. These are typically already small hits that barely surpassed the high threshold and have a long $t_2 - t_1$ delay. Finally, note how the slewing time $t_1 - t_0$ depends on the amplitude of the pulse, a factor that needs to be corrected afterwards.

is done through the calibration process explained in Section 2.5.

The data acquisition systems continuously processes the individual hits from each PMT and uses a trigger criteria to group hit into events. Currently the trigger condition is 28 hits in a 150 ns time window. The data for all hits is saved starting 500 ns before the trigger condition is met and 1000 ns after. Note that any shower front, traveling close to the speed of light, would take less than 1000 ns to completely cross the HAWC array at any angle.

This multiplicity trigger results in a trigger rate of ∼25 kHz, which can be reconstructed in near real-time by the on-site computers (with a latency of ∼5 s). Note that practically all of these events constitute real air shower events, as the rate at which this multiplicity trigger is met by random coincidence of the noise PMT hits —with an individual rate of ∼40 kHz for the center PMTs and ∼25 kHz for the outer PMTS— is several orders of magnitude lower than the expected and measured trigger rate from cosmic rays.

2.5 Calibration

The goal of calibration is to reconstruct the physical properties of a PMT hit, number of PEs and time of arrival, based on the low and high threshold crossings from the TDCs.

The calibration system consists of a green (532 nm) pulsed laser and a set of neutral density filter wheels that allows varying the light intensity over several order of magnitude. The light is transmitted to the tanks through fiber optics of the same

length, which are buried underground to reduce temperature-dependent variation in propagation time. Lastly, the light is passed through a diffuser located at the top of the tank and centered to uniformly illuminate the bottom of the tank.

The laser light is shined into the tanks repeatedly for brief periods of time ($\sim 2\,\mu$s) using computed controlled optical switches. This allows data taking to continue while performing calibration, since later the time windows during which laser light could have been in the tank are excluded from the analysis.

The charge calibration relates TOT measurements to the number of PEs, and results in curves similar to the one shown in Figure 2.6a. These calibration curves are obtained by shining low levels of light and measuring the resulting TOT distribution, which is then compared to the expected number of PEs distribution. A one-to-one relation between these two quantities is deduced by matching the quantiles of both distributions. Different settings of the filter wheel are then used to increase the light intensity and study pulses with increasing number of PEs and longer TOT values.

During reconstruction we use an effective charge, which is computed by multiplying the number of PEs detected by the central PMT by 0.46, and the outer PMTs by unity. This accounts for the higher efficiency and larger size of the central 10-inch PMT compared to the outer 8-inch PMTs. The effective charge is then directly related to the light level in the tank. While there is still a $\sim$10% PMT-to-PMT efficiency variation, which is accounted for in simulations, it has a negligible impact during reconstruction.

Very accurate timing is needed in order to reconstruct events with an accept-

able angular resolution. A back of the envelope calculation[2] shows that we need sub-nanosecond precision. This level of accuracy is obtained through a series of consecutive steps which methodically reduce the systematic timing offsets. The first steps are described here, as they concerned directly the calibration system, while further timing corrections, which bring the timing accuracy from a few nanoseconds to sub-nanosecond, are discussed in Section 2.7, as they are performed using real data after reconstruction, still to be discussed in Section 2.6.

The first step done by calibration is to adjust the timing of the full array based on the estimated time between firing the laser and receiving the signal. This includes the time it takes for the light to go through splitters, optical fibers and the water, the intrinsic PMT delay, and the signal propagating in the cables and the electronics. Since the optical fibers and cables were set to have the same length, this period of time is mostly known and gets the timing calibration really close to the desired level of accuracy. Different sources of systematic uncertainties on this measurement are further corrected for as discussed in Section 2.7.

Slewing is another source of timing systematic, which is unrelated to the uncertainties in the light and signal travel time. This is the pulse-height-dependent time it takes for a pulse to cross the discriminator voltage threshold: a large hit will cross the threshold quicker than a small hit, even if they both arrived to the

[2]The angular resolution for large events is $\sim 0.1^\circ$ (~ 0.002 rad). The footprint for high energy events is ~ 100 m wide. This implies a maximum systematic timing error of less than 100m $\times$ $0.002/c = 0.6$ns. The fact the the shower front is not a real plane, but has curvature, results in even stricter requirements.

photo-cathode at the same time (see Figure 2.5). This effect is calibrated for each channel by measuring the time delay as a function of TOT after correcting for the light and signal travel time. This effect is of the order of 10 ns, as shown by the typical calibration curves in Figure 2.6b.

Some hits are excluded by the calibration from reconstruction for various reasons. At high light levels the chances of a photon skipping the photocatode and hitting directly the first dynode is not negligible. This is known as prepulsing and causes a small signal previous to the main pulse. This produces erroneous LoTOT measurements. At all high levels, but particular relevant for large hits, there is a chance of ionizing residual gases inside the PMT, generating positive ions that travel back to the photocathode and produce electrons, causing a spurious late arriving signal known as afterpulses. We apply a veto time window after big hits to suppress this effect. For very big hits afterpulsing interferes with the TOT measurement, and sets the maximum TOT that can be calibrated —i.e. hits with a longer TOT than a certain value are excluded. Besides exclusions due to prepulsing and afterpulsing, hits in general are excluded from reconstruction if the LoTOT and HiTOT pattern is inconsistent with a real pulse.

2.6 Event reconstruction

In Section 2.5 we described how to reconstruct the physical properties of the PMT hit: number of PEs and timing. In this section we describe how these measurements are used to reconstruct the physical properties of the primary particle

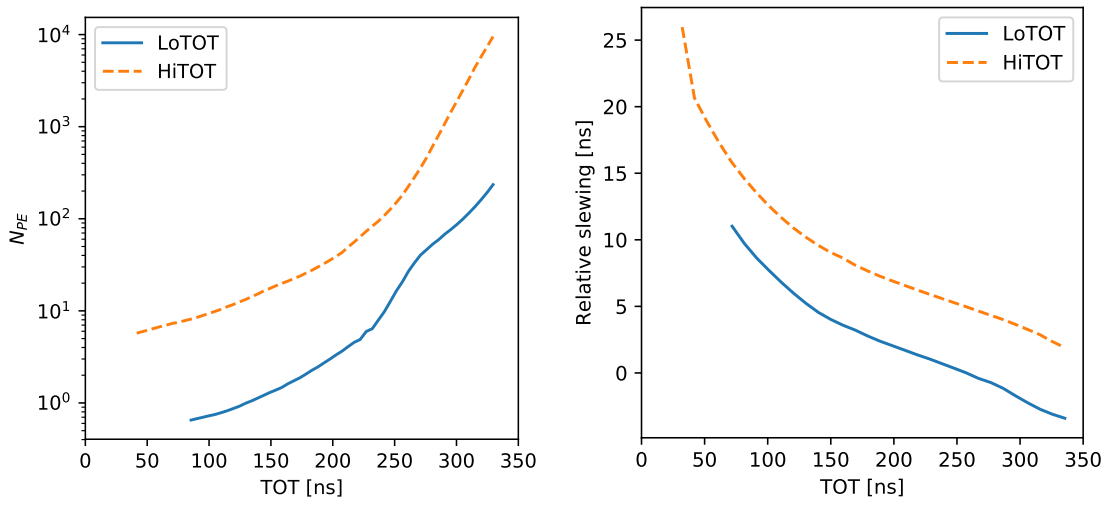

(a) (b)

Figure 2.6: These two plots show the main output of the calibration. **(a)** shows the relation between LoTOT/HiTOT and the number of PEs in the PMT signal. LoTOT is used to measure the number of PEs when the high threshold is not crossed. Both LoTOT and HiTOT have an imposed minimum value. The minimum LoTOT value prevents misidentifying the 4 edges produced by two 2-edge hits with a real 4-edge hit (See Figure 2.5), while the minimum HiTOT is based on the ability to resolve two continuous edges. **(b)** shows the relative timing correction that accounts for the longer time it takes for small hits to cross the voltage threshold in the discriminator (slewing).

generating the extended air shower.

There are three main properties of the primary particle we are interested in reconstructing: the direction of the primary particle, the type — e.g. gamma ray or cosmic ray— and the energy. The direction reconstruction is discussed in Section 2.6.2 while the parameters used to try to distinguish gamma rays from cosmic rays are discussed in Section 2.6.3. Lastly, in this work we use the fraction of PMT hits as a crude estimate of the energy, as explained in Section 2.6.1.

The HAWC Collaboration has recently developed energy estimation algorithms [53] that, among other variables, use the charge distribution versus the core and the reconstructed zenith angle direction to provide a more precise measurement. These algorithms have an considerable impact above 10 TeV, a regime mostly important for sources in our own Galaxy, since EBL would strongly attenuate emission above that energy otherwise (see Section 1.3). These energy reconstruction algorithms were not used in this work and are therefore not discussed.

2.6.1 Fractional hits binning scheme

Events in HAWC can have considerable variation in quality, mostly determined by the size of the shower footprint when it reaches the HAWC ground level. Figure 2.7 shows a small and large size typical events for comparison. Small events near the trigger threshold are susceptible to noise caused from other events landing far from the detector which impair our ability to reconstruct its direction and discriminate between a gamma ray and a cosmic ray. Large events are much richer in information

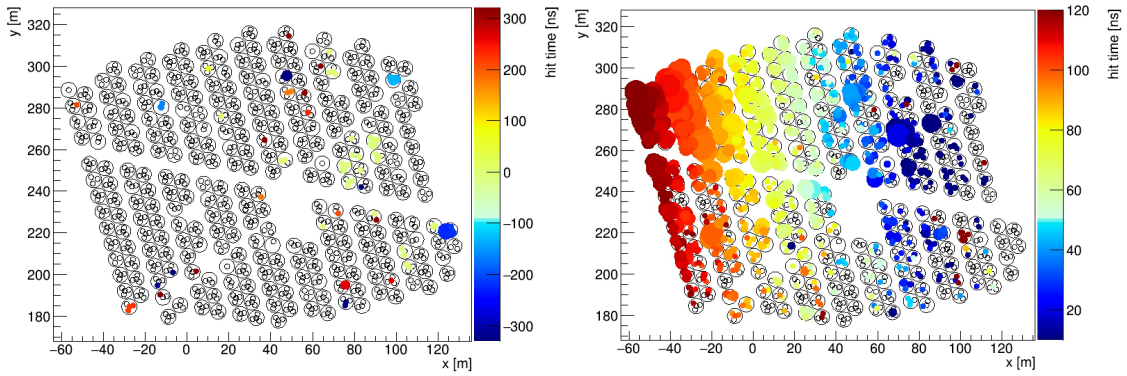

(a) (b)

Figure 2.7: Typical small **(a)** and large **(b)** size events. Each colored circle represents a PMT hit. The fill color represent the timing while the size is proportional to the number of PEs detected.

that can constrain the direction and event type, and makes them less susceptible to noise from other events.

While both the angular resolution and the gamma-hadron separation power increases with the size of the shower, the flux of most of the sources we can observe is rapidly decreasing as a function of energy —i.e. the SED peaks below our energy range. As a result, combining all events using a simple counting analyses would result in a considerable loss of sensitivity, since the low number of high quality events would not have an important contribution due to the large background of low quality events. We thus divide our data into multiple analysis bins based on the fraction of PMTs hit. These bins are tag by a number $\mathcal{B}$ as defined in Table 2.1. A view of the Crab Nebula for each of these analysis bins is shown in Figure 2.8.

The size of the shower footprint is strongly correlated with the energy of the

$\mathcal{B}$	PMTs hit	PINCness cut	Compactness cut	All-sky rate [Hz]
1	6.7–10.5 %	<2.2	>7.0	430
2	10.5–16.2 %	<3.0	>9.0	140
3	16.2–24.7 %	<2.3	>11.0	38
4	24.5–35.6 %	<1.9	>15.0	4.8
5	35.6–48.5 %	<1.9	>18.0	1.1
6	48.5–61.8 %	<1.7	>17.0	0.19
7	61.8–74.0 %	<1.8	>15.0	0.11
8	74.0–84.0 %	<1.8	>15.0	0.030
9	>84 %	<1.6	>3.0	0.044

Table 2.1: The analysis bins $\mathcal{B}$ are defined based on the fraction of PMTs hit with respect to the total PMTs available. In addition to the fraction of PMTs hit being in between the defined range, each event must pass the PICNness and compactness cuts, two gamma-hadron separation parameter discussed in Section 2.6.3. The average all-sky rate after cuts, which fluctuates over time by ∼10 %, shows the very different statistical regimes between the analysis bins.

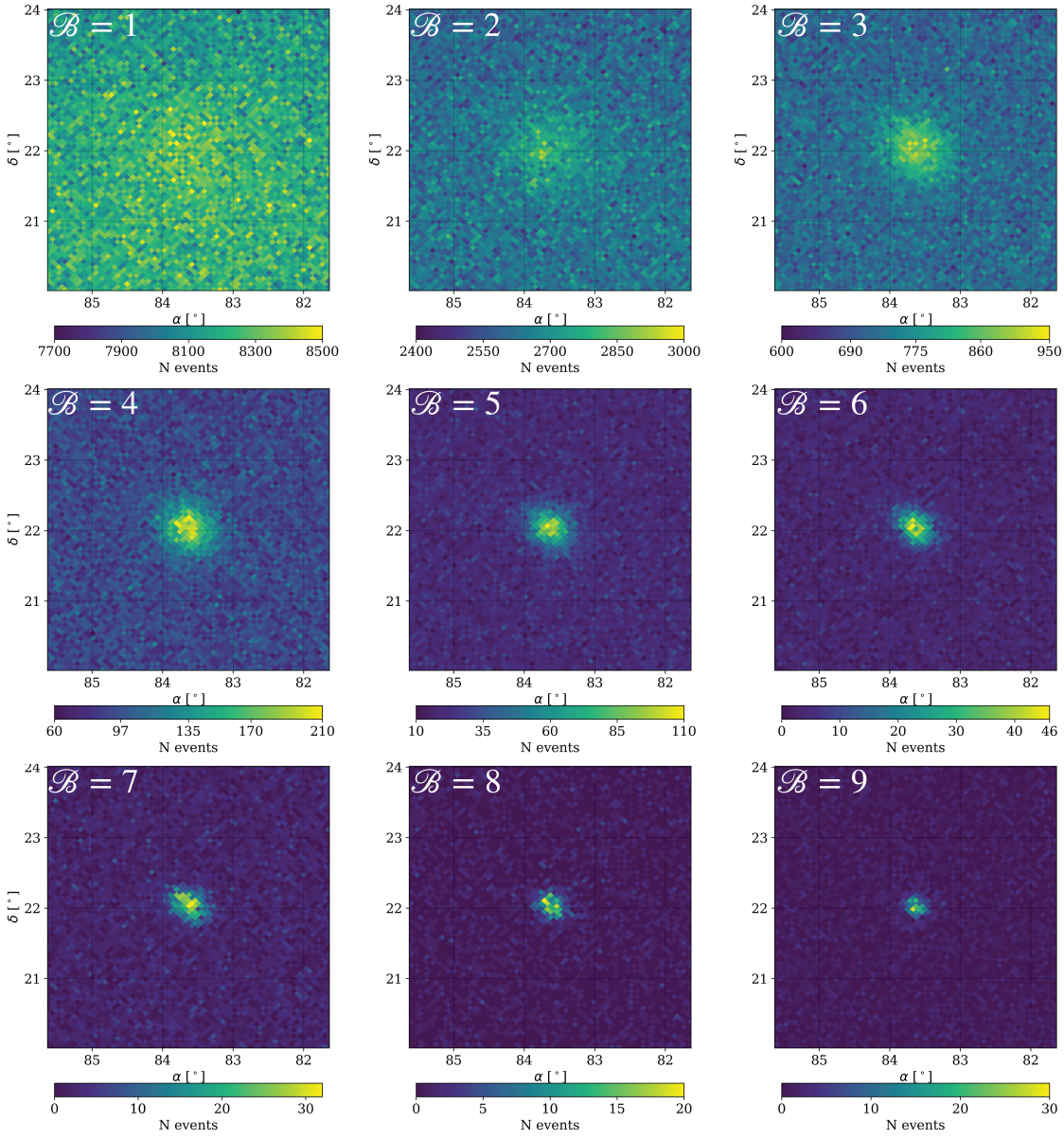

Figure 2.8: The Crab Nebula as seen on each $\mathcal{B}$ analysis bins defined in Table 2.1. This encompasses 1094 days of data. In general, the higher the $\mathcal{B}$ analysis bin number, the larger the shower footprint, the better the angular resolution and background rejection and the higher the energy of the primary gamma ray.

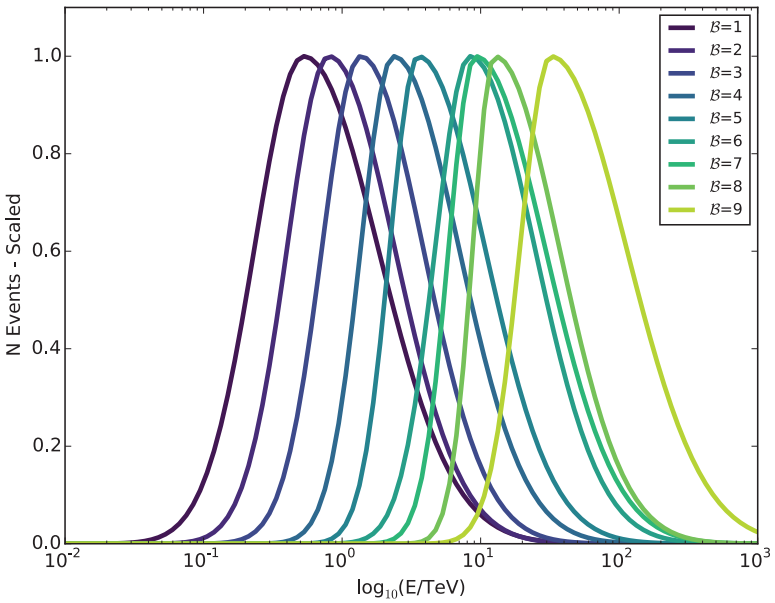

Figure 2.9: Normalized log-gaussian fit to the energy distribution of each analysis bin $\mathcal{B}$ (defined in Table 2.1). This assumes an SED proportional to $E^{-2.63}$ and a declination of 20°N, similar to the Crab Nebula. Reproduced from [54].

primary particle, as shown in Fig. 2.9. While more sophisticated analysis which account for the measured charge distribution and zenith angle can provide better energy resolution and dynamic range above 10 TeV, this parameter is enough to constrain the spectral index, and even energy cutoffs below a couple tens of TeVs.

Lastly, note that the first $\mathcal{B}$ bin starts at about 70 PMTs hit, which is greater than the multiplicity trigger condition described in Section 2.4. While events below the analysis threshold are real —i.e. not due to noise—, the current reconstruction is not good enough to use them to improve our sensitivity and the MC do not model this regime well enough. Recently the HAWC collaboration has made considerable progress improving both the reconstruction and simulation of these near threshold

events [55], however these new algorithms were not used for this work and are therefore not discussed.

2.6.2 Direction reconstruction

HAWC uses the timing of each hit to reconstruct the primary particle direction, as the timing profile matches the shower front. To first order, the shower front is described by a plane to which the direction of the primary particle is a normal. There is however a deviation from the plane shower front, or curvature, since particles arriving far from the core have gone on average through more distance and more scattering processes . In addition, the particle density decreases and the distribution is broader as you move away from the core, which increases the average time it takes for the first particle to be detected. The true shower front curvature and the "sampling" effect combined produce a delay as you move further from the shower core of about 0.2 ns/m, as shown in Figure 2.10d.

While this is a correction of 10–20 % compared to the total time it takes for an event to go through the detector, not accounting for this effect can lead to significant degradation of the angular resolution —i.e. compare $\arctan(0.2\text{ns} \times \text{c}) = 3.4^\circ$ to our angular resolution in Figure 2.11—.

In order to correct for the shower front curvature it is then required to have a good estimate of where the shower core is. This is approximately the location where the maximum concentration of detected PEs is, as can be easily determine for the sample event in Figure 2.10a. In order to determine the core a first guess is

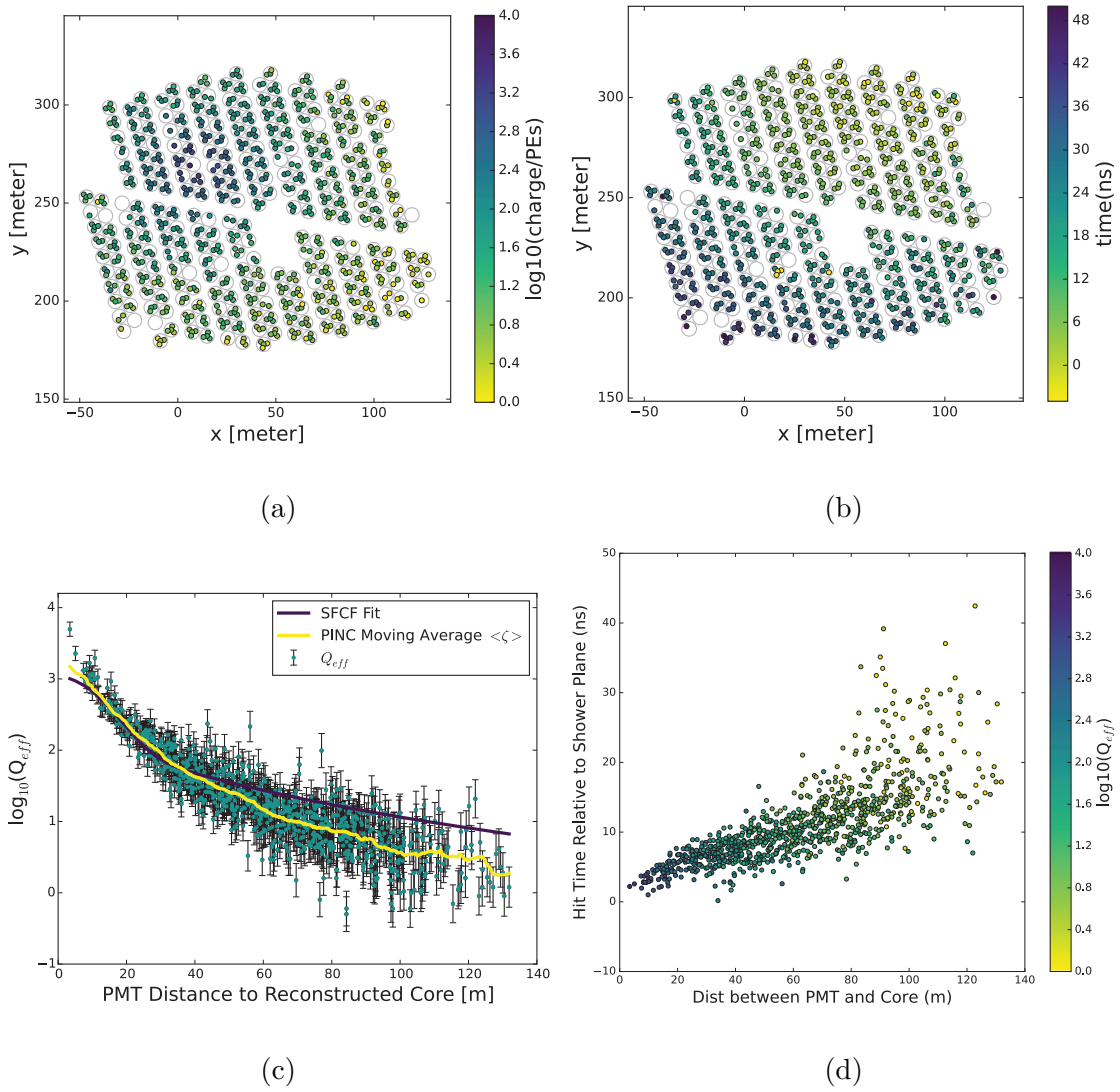

Figure 2.10: Large event sample with a high probability of being a gamma ray from the Crab Nebula. **(a)** Shows the effective number of PEs measured by each PMT (see Section 2.5). **(b)** Relative time at which each PMT was hit. **(c)** Lateral distribution of the measurements in (a) with respect to the core location. The SFCF fit corresponds to Eq. 2.1. The PINC parameter, discussed in Section 2.6.3, is the average charge in a given annulus around the core location. **(d)** Difference between the measured time in (b) and the one expected by a flat shower plane. Reproduced from [54].

obtained based on the center of mass of all the PMTs that detected signal weighted by the number of PEs detected. This is then used as the seed to fit the following monotonically decreasing radial function:

$$S_i(r) = A\left(\frac{1}{2\pi\sigma^2}e^{-r^2/2\sigma^2} + \frac{N}{(1/2 + r/r_m)^3}\right), \tag{2.1}$$

where S_i is the effective charge detected by the i-th PMT and its distribution is parametrized by r_m, the Molière radius of the atmosphere (set to 120 m); σ, the characteristic width near the core (set to 10 m); N, the weight of the tail compared to the core (set to 5×10^{-5}); and A, the overall normalization, which is set free, together with the core location in the ground.

This function was chosen since it is fast to evaluate while at the same resembles the lateral charge distribution (see Figure 2.10c). While the NGK function (see Section 1.2.2.1) more accurately represents this distribution, it contains gamma functions and exponents that are slow to evaluate, and it is indeterminate at the center, which causes convergence issues during the fit. This approximation is fast and provides a median core location error of a few meters providing the core landed inside the array, which is sufficient to correct for the shower front curvature. We call this algorithm SFCF (short for Super Fast Core Fit).

Once the core is determined the timing of the hit is corrected to account for the shower curvature. The correction is a function of both the radius from the core and number of PEs, which account both for the intrinsic curvature and sampling effects. This correcting function is determined from events near the Crab Nebula applying strict gamma-hadron cuts in order to have a pure gamma-ray sample of

event for which we know the direction. The correction is then the difference between the measured timing and the expected one based on flat plane hypothesis.

Once the curvature correction is applied, the direction is determined by a simple χ^2 fit to a plane. Finally, with the purpose of reducing the noise, hits within 50ns of the fitted shower plane are selected and use in a second pass of the core and plane fit.

2.6.3 Background rejection

Gamma rays account for only a very small fraction of the events detected by HAWC. Most extensive air showers are produced by charged cosmic rays. While HAWC does perform studies using cosmic rays [56–58], in this work cosmic rays represent a background signal.

We exploit the differences in the footprint left by a gamma ray with respect to a cosmic ray. As described in Section 1.2.2.1, gamma rays have a characteristic smooth and azimuthally symmetric lateral charge distribution around the core of the shower; a hadron shower on the other hand is typically not azimuthally symmetric, has clusters of particles far from the core and often contains multiple muons, which translates in large signals detected only in an individual tank. For example, compare Figure 2.7b, likely a hadron, to Figure 2.10, likely a gamma ray.

Two parameters are used to quantify these characteristics and identify hadrons. The first parameter, called compactness ($\mathcal{C}$), is defined as

$$\mathcal{C} = \frac{N_{\text{hit}}}{\text{CxPE}_{40}}\,, \tag{2.2}$$

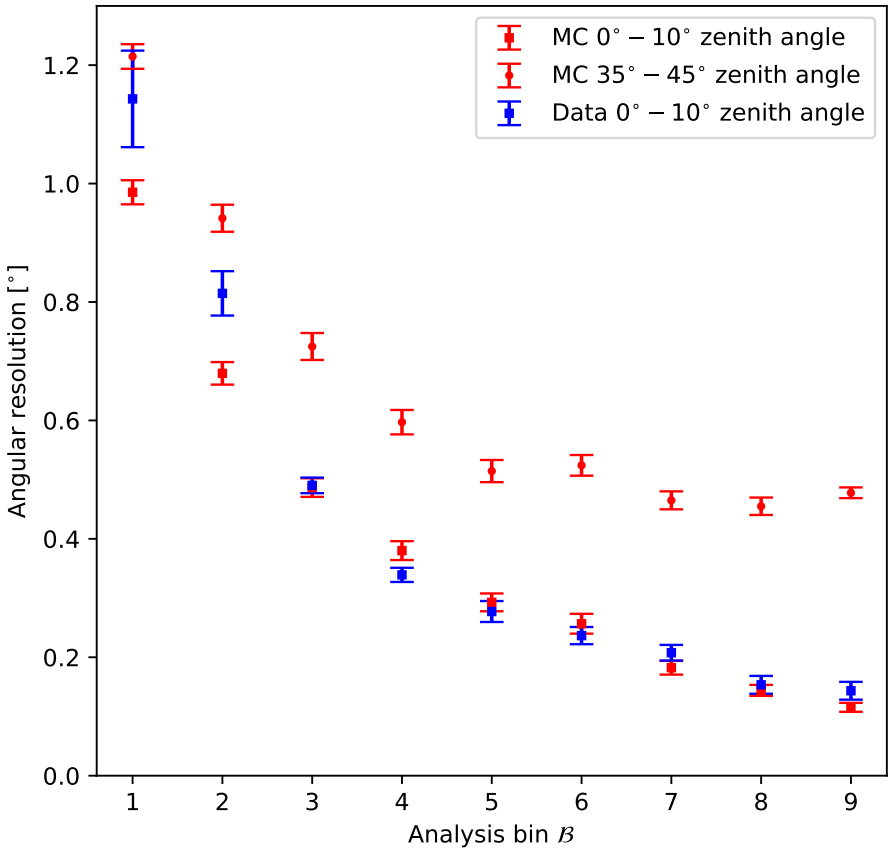

Figure 2.11: HAWC angular resolution near zenith and at the edge of our FoV, defined as the angular distance from the source location that contains 68 % of the events. This is plotted versus the analysis bins $\mathcal{B}$ proportional to the number of PMTs which detected a signal. The angular resolution predicted by Monte Carlo simulations is compared to the one measured on the Crab Nebula only for events near zenith, as the number of detected events at the edge of our FoV are not enough to accurately measure it.

where CxPE_{40} is the largest effective charge outside a radius of 40 m from the core and N_{hit} is the total number of PMT with a detected signal. Due to the presence of muons CxPE_{40} is typically larger for hadronic event than for gammas, while N_{hit} serves as a normalization factor to account for naturally occurring higher charge hit in large events. Gamma rays are then selected by using event with a high compactness value, as shown in Figure 2.12a. In the rare case that there are no hits outside a radius of 40 m from the core the event automatically passes the cut. These are usually small events with not enough information to provide gamma-hadron separation power anyways.

The other parameter, called PINC (short for Parameter for Identifying Nuclear Cosmic rays), quantifies how azimuthally symmetric the shower is. It is computed by taking the average effective charge of several annuli, with a width of 5 m, around the estimated core location and then comparing them with the charge measured by each individual PMT. The formula is

$$\mathcal{P} = \frac{1}{N} \sum_{i=0}^{N} \frac{(Q_i - \langle Q_i \rangle)^2}{\sigma_{Q_i}^2}\,, \tag{2.3}$$

where Q_i is the logarithm of the effective charge measured by the i-th PMT, $\langle Q_i \rangle$ is the average charge measured in the annulus where the PMT is located and $\sigma_{Q_i}^2$ is the standard deviation of Q_i, as previously measured from a sample of likely gamma-ray events coming with a direction consistent with the Crab Nebula. Note that this is essentially a χ^2 test, and as such gamma rays, which are azimuthally symmetric, result in $\mathcal{P} \sim 1$, while for hadrons $\mathcal{P}$ is typically larger. The PINC distribution and gamma-ray excess is shown in Figure 2.12b.

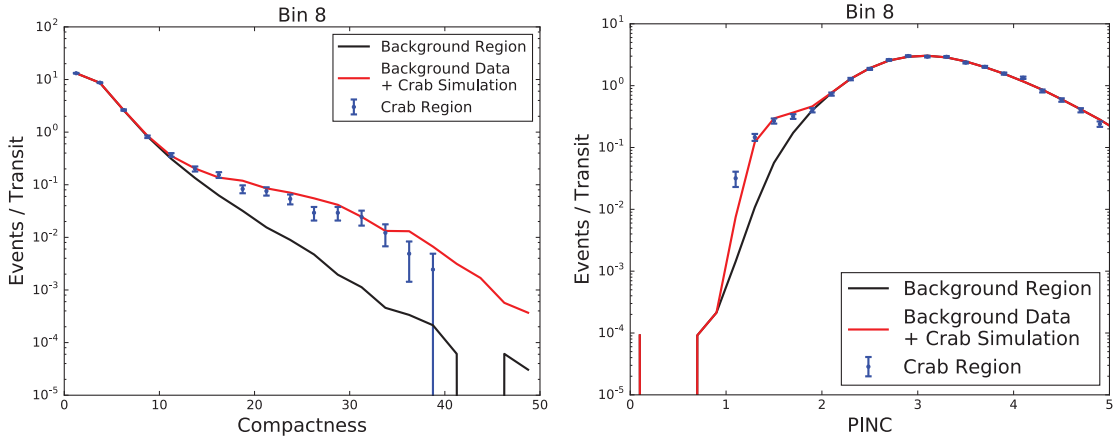

(a) (b)

Figure 2.12: Distribution of the two parameters used to discriminate between gamma-ray and cosmic-ray showers (for analysis bin $\mathcal{B} = 8$), compactness **(a)** and PINC **(b)**. The data points correspond to events detected in the vecinity of the Crab Nebula, while the black curve was obtained from events in a large annulus further away from the Crab and scaled down based on the solid angle ratio of both areas. Lastly the red curve correspond to background measurement plus the signal expectation from simulations. A clear excess can be observed at large compactness and low PINC values. Reproduced from [54].

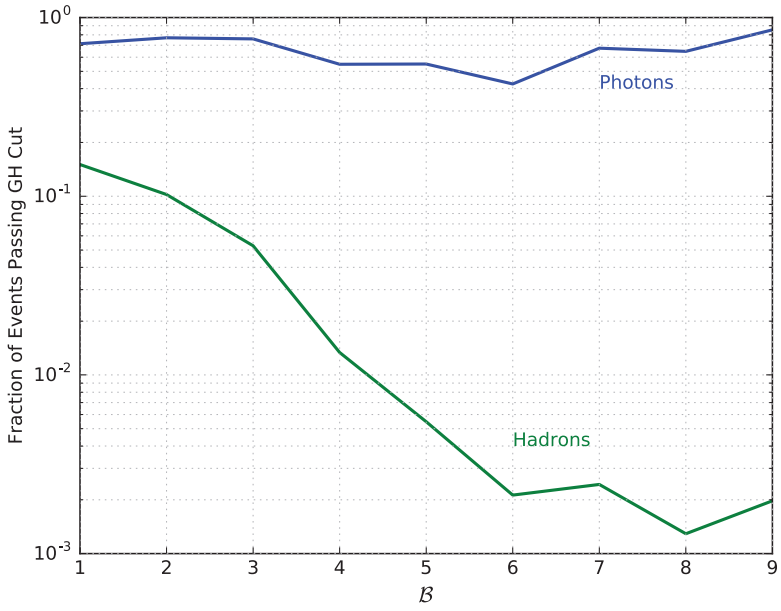

Figure 2.13: Fraction of gamma rays (estimated from simulation) and cosmic ray (measured) passing the gamma-hadron (GH) separation cuts for each analysis bin $\mathcal{B}$ defined in Table 2.1.

In order to select most gamma rays and reject as many hadrons as possible we must select events with low PINC and large compactness. The optimal cuts were determined based on the signal detected from the Crab using around one year of data. The optimal cuts depend on the shower size, and the values used for each analysis bin $\mathcal{B}$ are shown in Table 2.1. The fraction of gamma rays and hadrons passing this cut is showed in Figure 2.13.

In practice CxPE_{40} is more relevant for small low energy events, since the small number of PMT hits make it hard to differentiate an azimuthally symmetric shower from one that has more structure. For large high energy events PINC becomes a very powerful parameter, as any abnormality is easy to identify based on the information

contained in the rest of the PMTs hit.

2.7 Timing corrections and alignment

Good timing is crucial for a good angular resolution. As explained in Section 2.5, we require sub-nanosecond precision while the calibration system is only good to a few nanoseconds. In order to achieve this goal we should then make use of the cosmic-ray and gamma-ray data the experiment gathers.

The first step is to reconstruct many events and compute the time residuals. These are the average differences between the expected arrival time from the resulting fit using the whole detector and the measured arrival time at a given PMT. If a channel was miscalibrated —i.e. the time delay through a calibration component was different than expected—, then the time residual distribution will not be centered at zero. We use the time residuals to correct the timing and then repeat the procedure again. It takes a couple more iterations for this procedure to converge and the residual to be centered at zero.

While fixing the time residuals flattens the timing of the detector, this plane might still be tilted. This might be caused, for instance, if the cables are systematically slightly longer on one side of the detector than the other. In order to remedy this we correct the timing in such a way that the maximum density of reconstructed events is at zenith. This is where the atmosphere is the thinnest and has the least absorption, and therefore we expect the number of events to decrease as a function of zenith angle. This correction is of the order of $\sim 1^{\circ}$.

The HAWC absolute pointing is still off by $\sim 0.1^{\circ}$ after the zenith alignment, a quantity that, while small, is comparable to our angular resolution. This happens because cosmic rays are charged particles and therefore their trajectories can be bent by the Earth's magnetic field. To fix this we finally introduce another correcting tilt and require that the Crab Nebula be located at the known location. Note that while a tilt has only two degrees of freedom, the remaining degree of freedom represents a rotation around zenith and it's not needed since the locations of the PMT are surveyed to a very high precision —i.e. there is no need to align the north—.

These timing corrections remain fairly constant over time. They typically only need to be updated when there are significant changes to the detector, such as an upgrade of the electronics.

2.8 Detector simulation

Throughout this chapter it has been described how HAWC detects and reconstructs gamma rays of cosmological origin. This last section discusses the simulation of the detector, the key step that allows us to go from counts to the physical parameters of a source, such as flux and spectral energy distribution.

We simulate both gamma rays and different species of cosmic rays. The former is used compute the flux and spectral energy distribution of gamma-ray sources while the latter is currently used mostly for checks and simulation fine-tuning. While the simulation of cosmic rays can be used to estimate the background, as it was done during the HAWC design, we can now estimate the background to a greater precision

using data itself.

We perform a Monte Carlo simulation particle by particle. They are injected at the top of the atmosphere and then their propagation through the atmosphere simulates, tracking each individual secondary particle produced. This is followed by the simulation of their interaction with the detector and lastly of the PMT response.

The particle energy, core distance from the center of the detector and zenith angle are drawn from the following distributions:

$$\begin{aligned} \Psi(E) &\propto E^{-2} \\ R(r) &\propto 1 \\ Z(\theta) &\propto \sin(\theta)\cos(\theta)\,. \end{aligned} \tag{2.4}$$

The events are thrown uniformly in the azimuth coordinates, both for the core location and incoming direction.

It can be readily noted that the events are not thrown with the same physical distributions that we want to emulate. While the zenith distribution is approximately the same[3], the radial distribution emphasizes events near the detector and the energy distribution is typically harder than typical for sources in the HAWC energy range (and furthermore, depends on each source). It is done this way to have enough statistics for cases we are the most sensitive to, such as at high energy and inside the detector. This is called *importance sampling*, and requires us to weight

[3]The $\sin\theta$ term in the zenith angle distribution is proportional to the differential solid angle area and the $\cos\theta$ term is proportional to the projected area of the detector as seen by an incoming particle

each event appropriately after the simulation. This is described in Appendix A.

The primary particle is propagated through the atmosphere using the CORSIKA package [59]. CORSIKA simulates the development of extended air showers. Primary and secondary particles are tracked until they interact with an air nuclei or decay. The final output is a list of secondaries particles with location and momentum provided at an altitude of a few meters above HAWC.

The list of secondary particles is then injected into a model of the detector built on GEANT 4 [60]. GEANT 4 simulates the interaction of the secondaries with the components of the detector. For example, it simulates the conversion of MeV gamma rays into charged particles when they interact with the water; the production of Cherenkov photons by charged particles as the move through the water; and the propagation of such photons to the face of the PMTs. Many other details like the reflections of Cherenkov photons with the PMT face and tank walls are also taken into account. The final output is a list of photons that arrived at the photocathode of each PMT, including their relative location.

For each PMT we convert the list of photons that arrived at the photocathode into a single hit, with a charge and timing as it would have been registered by the data acquisition system. We call this DAQSim, and while it does not simulate the individual pulses nor the TOT, it reproduces the resulting time and charge distributions. The hit time is defined as the time when the first Cherenkov photon interacted with the photocatode. For each Cherenkov photon we assign a charge value based on a probability distribution which is dependent on the impact parameter —i.e. distance from the center of the photocathode—. This probability distribution was

measured in laboratory conditions and includes the probability that the photon does not produce a photoelectron at all. The mean of this distribution is matched to the mean of the TOT distribution for a single PE. The charge of the hit is simply the sum of the resulting charge for each Cherenkov photon.

Various DAQSim parameters are fine tuned using data from cosmic rays in order to reduce our systematic uncertainty. The photon to photoelectron efficiency conversion is tuned for each PMT based on muon signals. Muons barely lose energy as they travel through the tank, generating Cherenkov photons at a near constant rate and therefore provide a mono-energetic calibrating source. The minimum charge that would trigger the low voltage discriminator is tuned to reproduced the distribution of number of PMTs hit in an event. Lastly, the charge for big hits is modified slightly to match the measured PEs distribution. We believe the time distribution of photons from real EAS has a larger spread than the one from the calibration laser source causing a slightly erroneous TOT measurement.

In Figure 2.14 we show that the excess observed from the Crab Nebula agrees with the prediction from simulation.

2.9 Summary

In this section we presented the principles of operation of HAWC, a gamma-ray detector sensitive from $\sim$100 GeV to $\sim$100 TeV. HAWC observes gamma rays by detecting secondary shower particles that arrive at ground level. These are detected by means of the Cherenkov light produced when they travel through the water

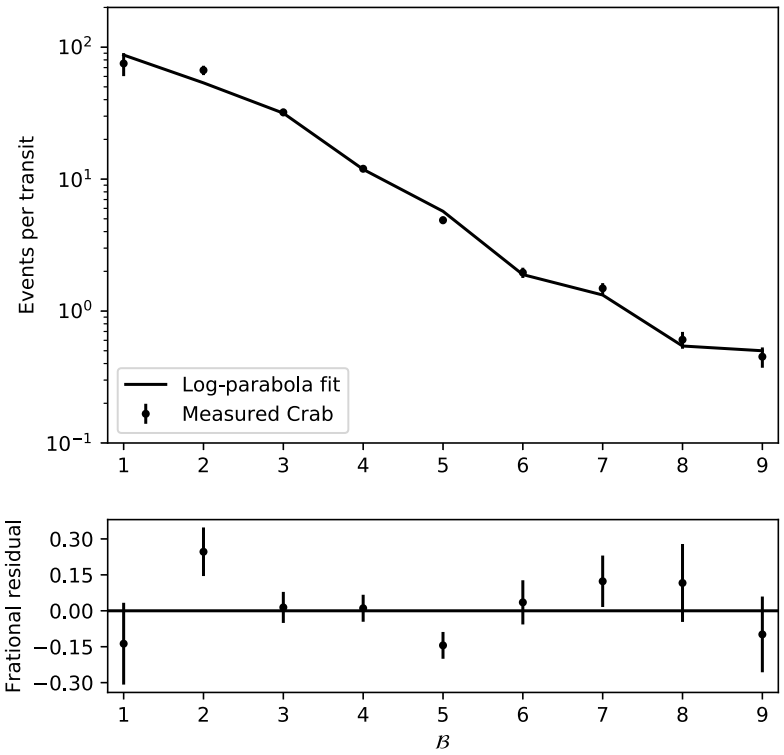

Figure 2.14: Measured photons from the Crab Nebula, after background subtraction for each bin. The signal is calculated fitting the Crab Nebula spectrum individually for each bin. The measurement is compared to the expectation from simulation assuming the all-bins fitted spectrum to a log-parabola —i.e $dN/dE = N(E/E_0)^{-\alpha-\beta\ln(E/E_0)}$, where N, α and β are free parameters.

contained in the tanks that make up the HAWC array, which is finally detected by photomultipliers. All these interactions are carefully simulated to infer the physical parameters of a source.

HAWC can achieve an angular resolution of up to $\sim 0.1^{\circ}$, for which timing needs to be calibrated through a series of steps to a achieve sub-nanosecond precision. HAWC has powerful background rejection capabilities, which are based on the smoothness and azimuthal symmetry present in gamma-ray showers but not in cosmic-ray induced showers. Both the angular resolution and gamma-hadron separation power depend heavily on the number of PMTs hit, so the data is separated into analysis bins based on that value (labeled by a $\mathcal{B}$ number).

Chapter 3: Analysis method

As seen in Chapter 2, the angular resolution and gamma-hadron separation power can vary between different events, improving dramatically as the size of the shower increases and a increased number channels that detect a signal. The number of large high-quality events is significantly lower than the number of smaller events, so simply combining them would result in a decrease in sensitivity. Simply disregarding lower-quality events, for which we have high statistics, would have the same effect. In order to accommodate this characteristic of the HAWC data, the collaboration developed the Likelihood Fitting Framework (LiFF) [61], a maximum likelihood analysis which allowed to divide the data into 9 analysis bins based on their size (labeled by a $\mathcal{B}$ number, see Section 2.6.1 and [54]), improving the sensitivity over a single bin analysis.

While LiFF has been successfully used in many studies, it was limited to a minimum time window of one transit ($\sim$6 hrs of exposure for each sky location during one day) because it assumed the exposure was constant during that period. While the HAWC response is highly dependent on zenith angle, a constant exposure is a good approximation for large timescale, months or years, since any downtime would tend to average out for all zenith angles. Analyses for daily times-scales typically

needed a correction factor to account for partial coverage [62], but still required the presence of data from most of the transit. Furthermore, since speed was not one of the design goals of LiFF, running it several times to look for emission in short timescales was time prohibited.

Searches for gamma-ray bursts, on the order of seconds, were performd by separate routines [63–65]. Due to the intense computer resources typically needed on this regime, and the data-taking rate of HAWC, this analyses used a single bin cut-and-count approach. Also known as ON/OFF analyses, they combine all the events instead of dividing the data based on shower size. While in general they result in a decrease in sensitivity with respect to a multi-bin maximum likelihood analysis, for most GRBs an analysis like the one performed by LiFF does not bring a significant increase in sensitivity over a single bin cut-and-count approach. The reason for this is that the bulk of GRB occur at very high redshifts and therefore their possible VHE emission is heavily attenuated by EBL (see Section 1.3). Since the size of an event is positively correlated with its energy (see Figure 2.9), this implies that most of the events from a typical GRB would fall into just a couple of $\mathcal{B}$ analysis bins, so in that case there would not be a great benefit from dividing the data based on the shower size.

The detection of gravitational waves by LIGO motivated the development of a new analysis framework. As discussed in Section 1.4.2, at least some gravitational waves are accompanied by gamma rays. Due to the detection range of current gravitational wave detectors, GRBs that can be simultaneously detected by them would need to occur at much lower redshifts than typical, and are therefore barely atten-

uated by EBL. Due to the scientific value of such observation, it became important to optimize our short timescales analyses for such events.

This new analysis framework, which we call ZEnith Band Response Analysis (ZEBRA) and present in this chapter, allows to perform a multi-bin maximum likelihood analysis for arbitrary timescales, from a fraction of a second to years. As shown in Figure 3.1, it significantly improves our sensitivity to GRBs with low redshift. It was also optimized for speed and relatively low computer resources in order to obtain the results from a search for gravitational wave counterparts within minutes after an alert is received. Furthermore, it bridged the gap between short and long timescale analyses, allowing us to study partial transits, and is versatile enough to be used to search and analyze multiple types of signals.

Chapters 4 and 5 contain two applications of ZEBRA. While some details might differ, most of the analysis is common to both studies. These will be mentioned in each individual chapter, and will reference sections in this one.

We first describe how we generate count sky maps, estimate the persistent background and keep track of the exposure (Section 3.1). Section 3.2 contains the mechanism to obtain the expected signal excess for a given hypothetical source, a necessary step to extract physical information from the count maps. In order to do that we use maximum likelihood analysis, discussed in Section 3.3.

In this work we search for emission for which we do not know either the location, the time, or both. Section 3.4 covers the search strategy we followed, which consisted of a grid search and overlapping time windows. This section also describes the way we deal with the "look-elsewhere effect" induced by this search

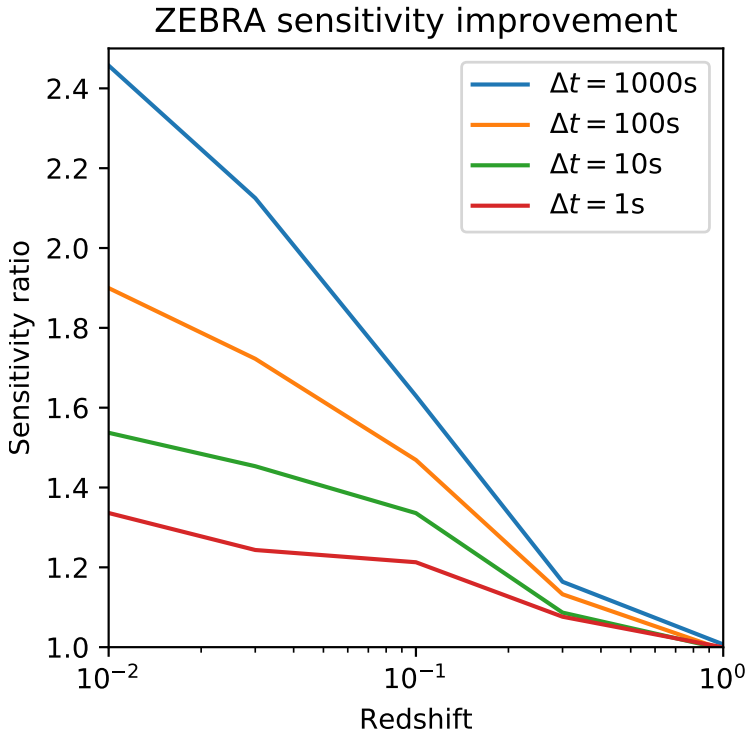

Figure 3.1: Sensitivity comparison between ZEBRA and a cut-and-count analysis. We define sensitivity as the flux that would result in a $>5\sigma$ detection 50 % of the time. We assume a simple power law spectrum with an index of -2. The increase in sensitivity arises from considering large events separate from smaller events. The event size is positively correlated with energy and the quality of the reconstruction. Because of this, the sensitivity gain decreases with redshift, as high-energy events are absorbed by EBL. Also, since large events occur less frequently, they are more likely to play a role in a detection the longer the time window. Although not shown here, an intrinsic cutoff at 1 TeV (100 GeV) would result in a similar effect as for a redshift of $z = 0.1$ ($z = 1$).

method.

Finally, in Section 3.5 we briefly review how we compute flux confidence intervals and upper limits in this work.

3.1 Map-making

Map-making is the process of going from potentially billions of events to a manageable set of maps which discretize the sky and contain the number of events reconstructed inside a given pixel. The grid used in this work is called HEALPix, and is described in Section 3.1.1. Map-making also involves keeping track of what periods of time were included in a given map (Section 3.1.2) and the estimation of how many of the events in a given pixels are background (Section 3.1.3), both needed to extract physical results from event counts.

Note that one map —including events and background— is produced for each analysis bin the data is divided into. Each step, such as the background estimation, is computed independently for each bin. For this work, we use the fractional hit binning scheme $\mathcal{B}$ defined in Table 2.1 (see Section 2.6.1), resulting in a set of 9 maps.

3.1.1 Hierarchical Equal Area isoLatitude Pixelization (HEALPix)

The Hierarchical Equal Area isoLatitude Pixelization (HEALPix) [66] is a scheme to divide a spherical surface into pixels of exact equal area. While originally developed to facilitate the fast and accurate harmonic analysis of Cosmic

Microwave Background (CMB) data, it has become a standard for skymaps and has been adopted by various other experiments, such as Fermi and LIGO. While not exclusively, HEALPix is also used extensively by the HAWC collaboration, and it was used for all the maps in this work.

Examples of HEALPix grids are shown in Figure 3.2. They are described by an N_{side} value and the numbering scheme. The grid is first divided in 12 base pixels, whose boundaries are shown with bold lines in Figure 3.2, which corresponds to $N_{side} = 1$. The edges of each pixel can be subdivided in two, $N_{side} = 2$, effectively dividing each pixel into 4. This process can be applied again on the resulting pixels to obtain a finer discretization, thus the name *hierarchical*. The value N_{side} corresponds to number of division of the boundaries of the original 12 base pixels, and is related to the interation step k, called order, by $N_{side} = 2^k$. The total number of pixels in the sphere is then $12N_{side}^2$. N_{side} is chosen such that the size of each bin is smaller than the typical angular resolution, therefore in this work we use 256, 512 and 1024 depending on the analysis bin (see Figure 2.11), which correspond to a characteristic pixel size of 0.23 deg, 0.11 deg and 0.057 deg respectively.

The pixels are arranged in parallel *rings* with their centers located at constant latitude values. There are a total of $4N_{side} - 1$ rings. Starting from the first ring at the north pole, $N_{ring} = 1$, each ring has $4N_{ring}$ pixels, increasing up to the N_{side}-th ring. The next $2N_{side} - 1$ rings all have $4N_{side}$ pixels, and then the number of pixels starts to decrease again, one per quadrant.

The numbering scheme can be either `RING` or `NESTED`. The former just labels the pixel starting from 0 at the top, increasing the number first by longitude and then

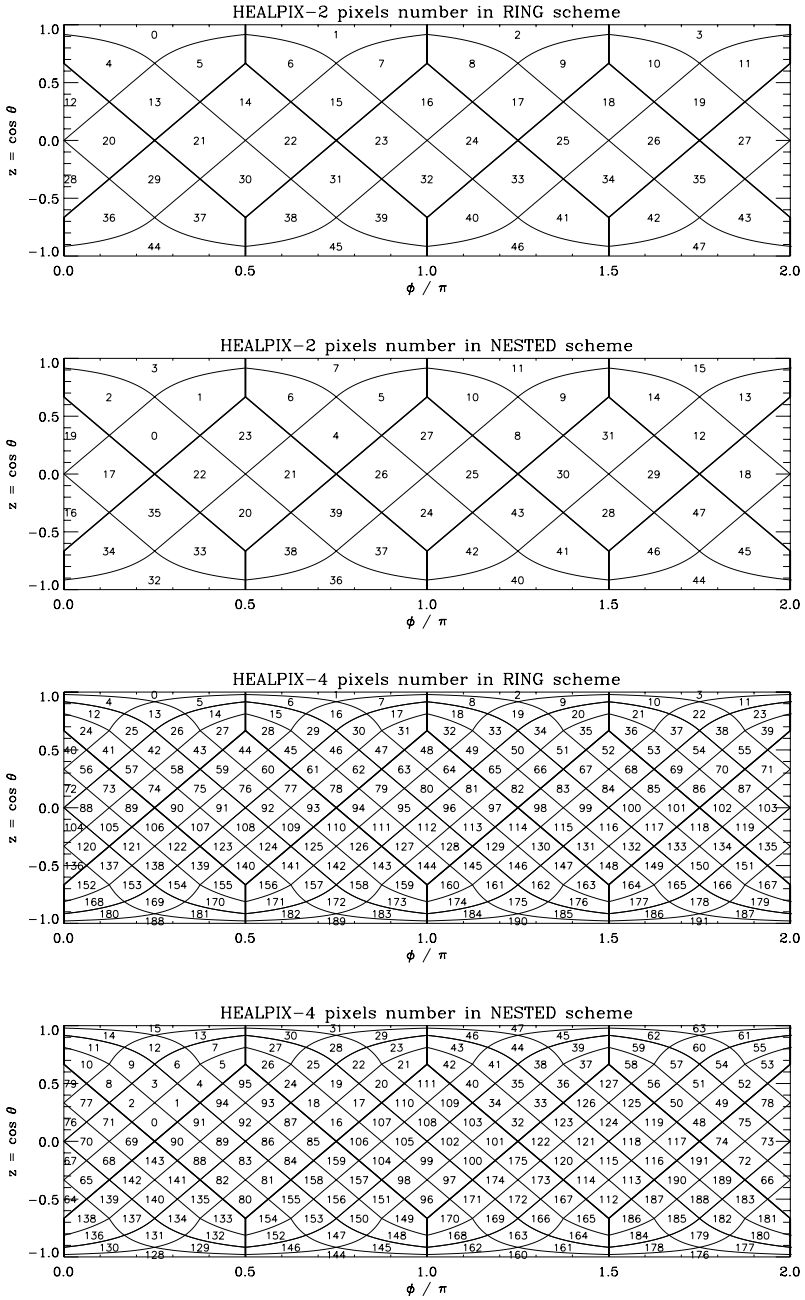

Figure 3.2: HEALPix grid in a cylindrical projection, for two different resolutions, $N_{side} = 2$ and $N_{side} = 4$. Both numbering schemes are shown for each. The boundaries of the 12 base pixels are highlighted with bold lines. Reproduced from [66](Fig. 4).

by latitude. This is the scheme we use more frequently as it simplifies operations involving convolutions along the constant latitude direction, which is natural for a ground-base experiment due to the Earth's rotation. The indices of the 12 base pixels is the same for both schemes, but in the `NESTED` scheme the index of each pixel of the next order p_{k+1} is related to the *parent* pixel of the previous one, which fully contains it, by $p_{k+1} \mod 4 = p_k$. This scheme is useful for algorithms involving nearest neighbors.

3.1.2 Tracking exposure

Since HAWC is mostly stable over time and operates with a high duty cycle, it is common in HAWC publications analyzing long periods of time (months or years) to assume that the exposure is uniform [54]. This is however not a good approximation in general for short periods since the effective area and angular resolution are highly dependent on the zenith angle. In this section we show how we systematically keep track of the exposure in order to be able to analyze arbitrary timescales.

This task can be simplified by noticing that because of the high data-taking rate of HAWC ($\sim$25 000 Hz) the time in between events is much shorter than the typical downtime period, which is of at least a couple minutes —e.g. during a run restart—. We then consider a period of time as downtime if the delay between two events is greater than 1 s. This has the further advantage of making less error prone to track downtime due to quality cuts —e.g. an incomplete operating detector can cause data exclusion.

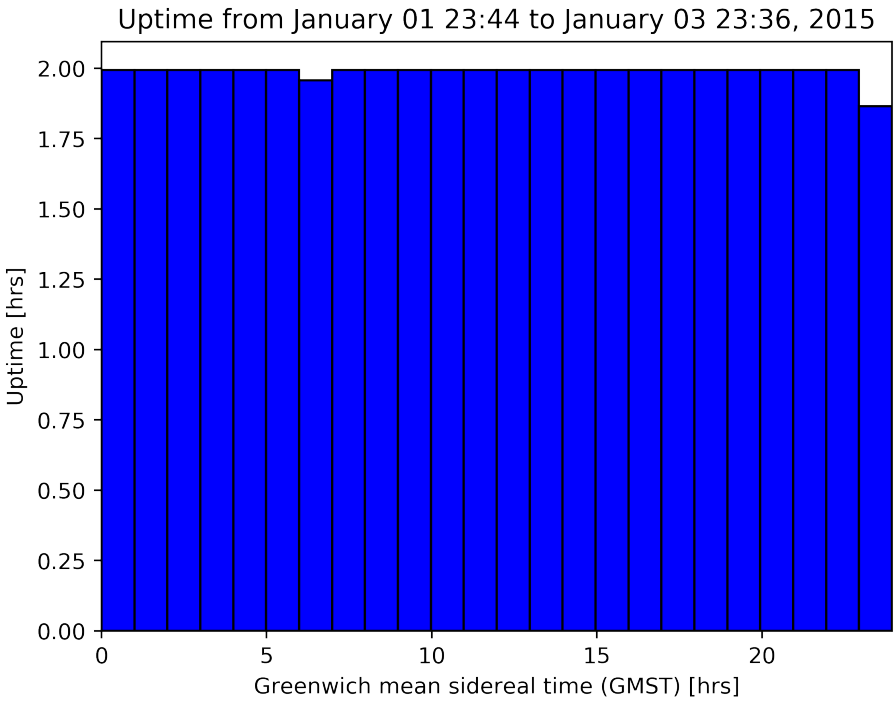

Figure 3.3: Typical uptime, covering two sidereal days. The y-axis represents the amount of time HAWC was on during the GMST bin in the x-axis.

Since the field of view of HAWC at any given time is completely determined by the Earth's rotation, it is enough to keep track of downtime only as a function of sidereal time (as opposed to the exposure for every point in the sky). This is exemplified in Fig. 3.3 in which a sidereal day was divided into 24 time windows, each 0.9972 hrs long, and we tracked the cumulative amount of time HAWC was taking data during each of these time windows. Since this example covers 2 days most of these time windows contain 1.9945 hrs, which indicates HAWC was taking data continuously. The two sources of downtime in this case are a run restart and quality cuts.

We eventually want to convolve the uptime with the detector response, in

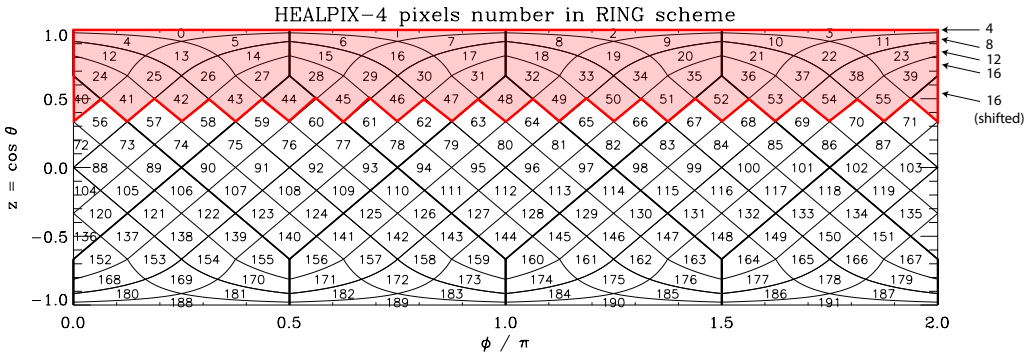

Figure 3.4: HEALPix grid for $N_{side} = 4$ and `RING` scheme (see Figure 3.2). Any given ring has the same longitude discretization as one of the rings in the shaded region

local coordinates, in order obtain the detector response for a given sky location and period of time. Since we do this convolving along the rings in the HEALPix grid, we discretize a sidereal day in the same way the HEALPix rings discretize the longitude from 0 to 2π. In order to do it efficiently we only fill and use the rings in the *north cap*, as shown in Figure 3.4. The longitude discretization of any given ring is the same as one of the first $N_{side} + 1$ rings, the $(N_{side} + 1)$-th ring having the same resolution as the previous one but shifted by half a pixel. The maximum time resolution for maps with a N_{side} of 256, 512 and 1024 is then 84 s, 42 s and 21 s, respectively.

3.1.3 Background estimation

The majority of the events detected by HAWC are cosmic rays, a statement that remains true even after applying the hadron rejection cuts discussed in Section 2.6.3. The expected number of events from this persistent background then needs

to be estimated. We use a modified version of the method called *direct integration*, developed to analyze Milagro data [67]. This method consists of convolving the normalized local direction probability distribution with the all-sky rate. The local distribution is mostly constant over time and its relative variation due to cosmic ray anisotropy is of the order of $\sim 10^{-3}$ [58].

The background is then computed as

$$\begin{aligned} \mathrm{bkg}(\mathrm{RA}, \mathrm{Dec}) &= \int \mathrm{rate}\,(t)\, \mathrm{P}(\mathrm{HA}, \mathrm{Dec}) dt \\ &= \int \mathrm{rate}\,(t)\, \mathrm{P}(\mathrm{t} - \mathrm{RA}, \mathrm{Dec}) dt \ , \end{aligned} \tag{3.1}$$

where rate(t) stands for the all-sky rate versus time after cuts and $\mathrm{P}(\mathrm{HA}, \mathrm{Dec})$ is the normalized direction probability distribution in local coordinates, called local acceptance or local efficiency. We bin this in hour angle —with respect to the Greenwich meridian— and declination since the former is related to right ascension by a shift in time, allowing for an easy convolution and prevents numerical artifacts due to finite pixel size. This is illustrated in Figure 3.5.

In the same manner as uptime (see Section 3.1.2), we bin the all-sky rate histogram in several different ways in order to perform a convolution required by direct integration along constant declination lines in a HEALPix grid without artifacts due to the finite size of the pixels. One subtlety is that this needs to be done in current epoch coordinates —as opposed to, for example, J2000—, such that the shift versus time of the local coordinates is only along the direction of the HEALPix rings.

In the original *direct integration* the rate and local acceptance were estimated directly from histograms filled during the same period of time considered in the

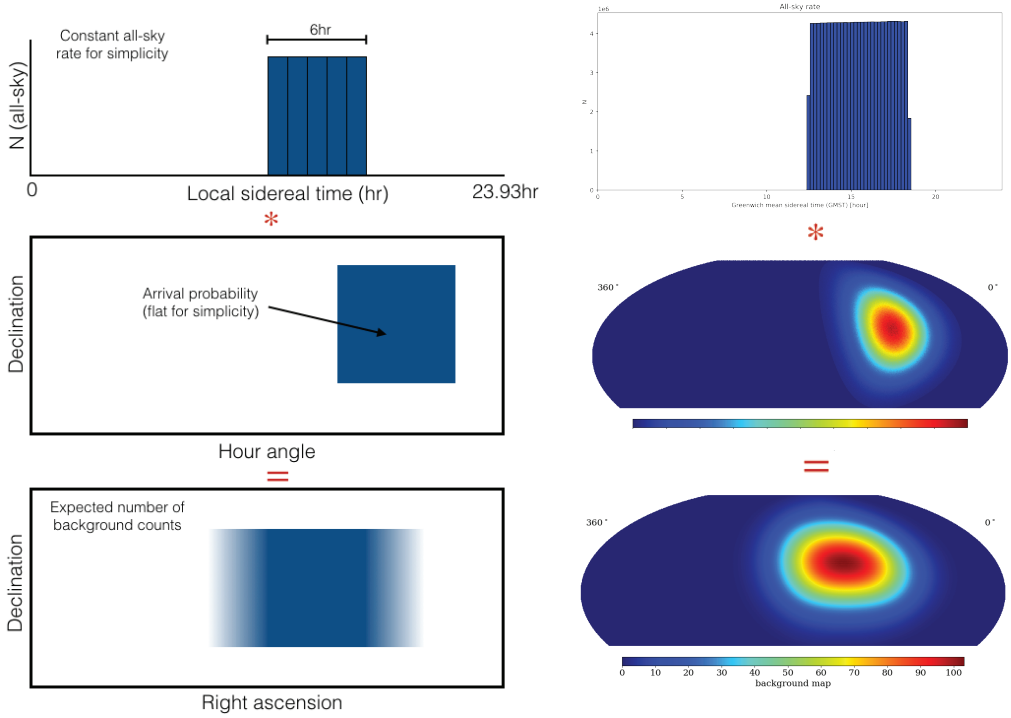

Figure 3.5: Background calculation example. On the left a simplified representation and on the right an example with real data. The top two plots are histograms of the total number of events (after cuts) detected in a given sidereal time window. We bin this histogram in several different ways according to the set of rings in the *north cap* of a HEALPix grid, same as we do for uptime (see Section 3.1.2), although here we show only one. The two plots in the middle represent the normalized probability distribution of arrival direction in local coordinates (hour angle and declination). Note how this is centered at the HAWC's coordinates (HA is conventionally positive towards the west). The bottom two plots are the convolution of the top and middle set of plots, and represent the expected number of background counts for the integrated period in a given pixel.

counts map. While this results in a very precise estimation of the background it is not always possible to do nor needed. When we enter the low statistics regime the counts are not enough to estimate the rate and local acceptance. This might happen when when we analyze short periods of time or for high energy analysis bins with strong gamma-hadron cuts. While we still estimate these two components from data, we sometime need to integrate for a longer period of time in order to get acceptable statistics. Under certain analysis cuts the number of background events is so scarce that not even an integration over multiple days is enough to approximate the local acceptance probability distribution. When this happens, since we know the probability distribution should be fairly continuous, we first smooth the local acceptance using splines. In extreme case when this is not enough we also average over azimuth. This assumes that the local acceptance is mostly dependent on zenith, that is, on the thickness of the atmosphere and projected area of the detector, and that the acceptance due to the specific geometry of the array is negligible. It is worth noting that the cases when this assumptions are needed are precisely the ones which do not need a very precise estimation of the background as the fluctuations of the different realizations of the background are much larger than the error on its estimated value.

The presence of a source affects the background estimation. This is particularly important for strong continuous sources, as depicted in Figures 3.6, where the signal can become a non-negligible part of its own background. In order to address this a region around the source is masked out when filling the local acceptance map, which is later corrected by the fraction a particular pixel spent inside the masked region.

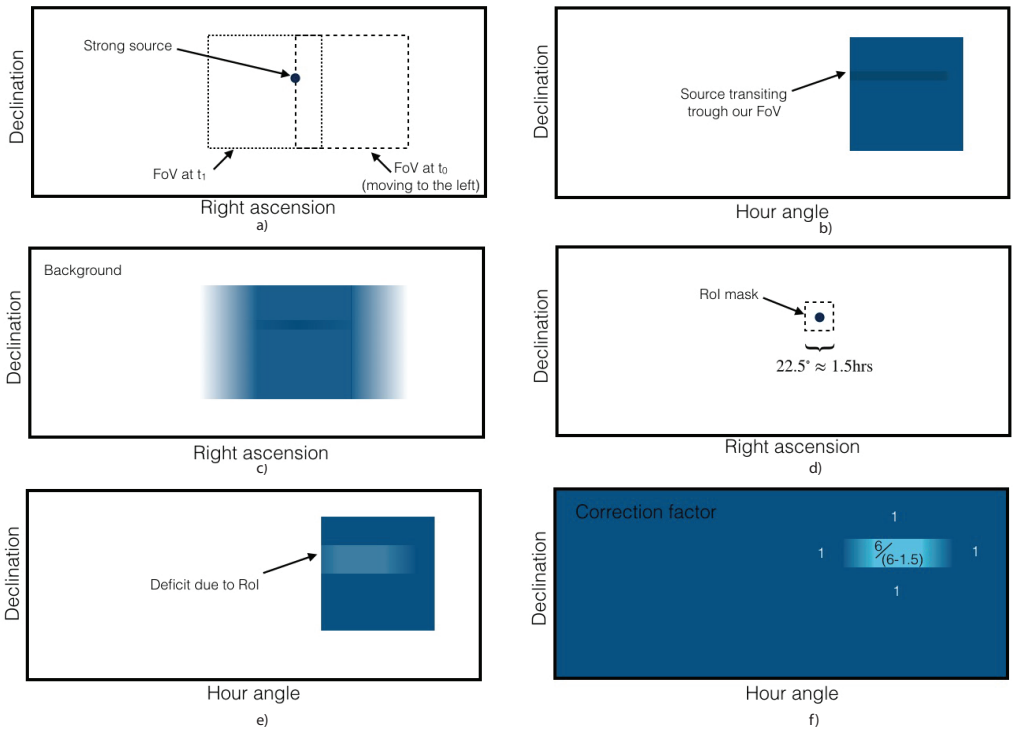

Figure 3.6: Schematic representation of the effect of a source in the background estimation and the removal of the contamination. **a)** Location of a sample strong source as the FoV moves through the sky during the integration period shown in Figure 3.5. **b)** Effect of the source in the local acceptance map. The probability distribution shows an excess along the path the source travels in the FoV. **c)** Effect of the source in the background estimate, which shows an excess compared of what it would have been if the source were not present. The effect of this artifact peaks at the location of the source. **d)** Masked region around the source. **e)** Since we masked out a region of the sky there will be a deficit in the local acceptance map. **f)** We correct for this multiplying each pixel by the ratio between the time it spent in and out of the exclusion mask. In this case the total integration time was 6 hrs, and the RA width of the exclusion mask was 1.5hr, so the maximum correction factor is $6/(6-1.5)$.

3.2 Source modeling and detector response

After we are done with the map-making step we have a count of the total number of events whose reconstructed directions fell inside a given pixels, for each analysis bin, together with an estimate of the number of events that are background counts. The next necessary ingredient to do our analysis is the expected number of counts for a given hypothetical source with a given location, spectrum and time period during which it emitted. This serves two purposes: first, it allows us to estimate physical parameters based on our event counting, such as flux normalization and spectral index; and second, as we'll see in Section 3.3, it allows to use our knowledge on how the counts on each pixel and each analysis bin relate to each other, if produced by a real source, to perform a more sensitive analysis.

The bulk of the source modeling is described in Section 2.8, when we randomly throw gamma-ray particles, simulate their propagation through the atmosphere, then through the HAWC detector, followed by the simulation of the PMT response and finally reconstructed with the same algorithm we use to reconstruct data. We could in principle run one of these simulations for each hypothetical source location and spectrum we want to test but it would extremely impractical. For example, we need to update our spectrum model continuously when fitting a parameter, and the location when doing a search. Instead we summarize the results of our MC simulations in a series of histograms, collectively called *detector response*, and *reweight* them appropriately as needed to simulate a hypothetical spectrum based on the canonical spectrum used in the MC.

The detector response consists of a series of matrices as depicted in Figure 3.7, 2D histograms of the energy of the primary particle and the difference between the real and the reconstructed incoming direction $\Delta\theta$. The sum of all the entries in the matrix for a given analysis bin is the total number of expected events per unit of time. The projection into the 1D $\Delta\theta$ histogram is the point spread function (PSF). We can also obtain the energy distribution of a given analysis bin by projecting it into the other axis.

The detector response uses this matrices instead of the keeping only these projections —PSF and energy distribution— since there is a non-negligible correlation between the energy and $\Delta\theta$. While our ability to reconstruct the direction depends mostly on the fraction of PMTs hit, the uncertainty in the curvature of the shower front and the core location deteriorate our angular resolutions for events which core is not totally contained inside the HAWC array. For a given fraction of PMTs hit, this happens more frequently for high energy showers which produce larger shower whose tail can trigger the detector even if they land far from the edges of the array.

Each of these detector response matrices is filled with events thrown with an spectral energy distribution (SED)

$$\Psi(E) \propto E^{-2}\,, \tag{3.2}$$

which is arbitrary but closed to what you would expect from a physical source. As explained in Appendix A, we can obtain the response for a new SED $\Phi(E)$ by weighting each bin in the response matrix by

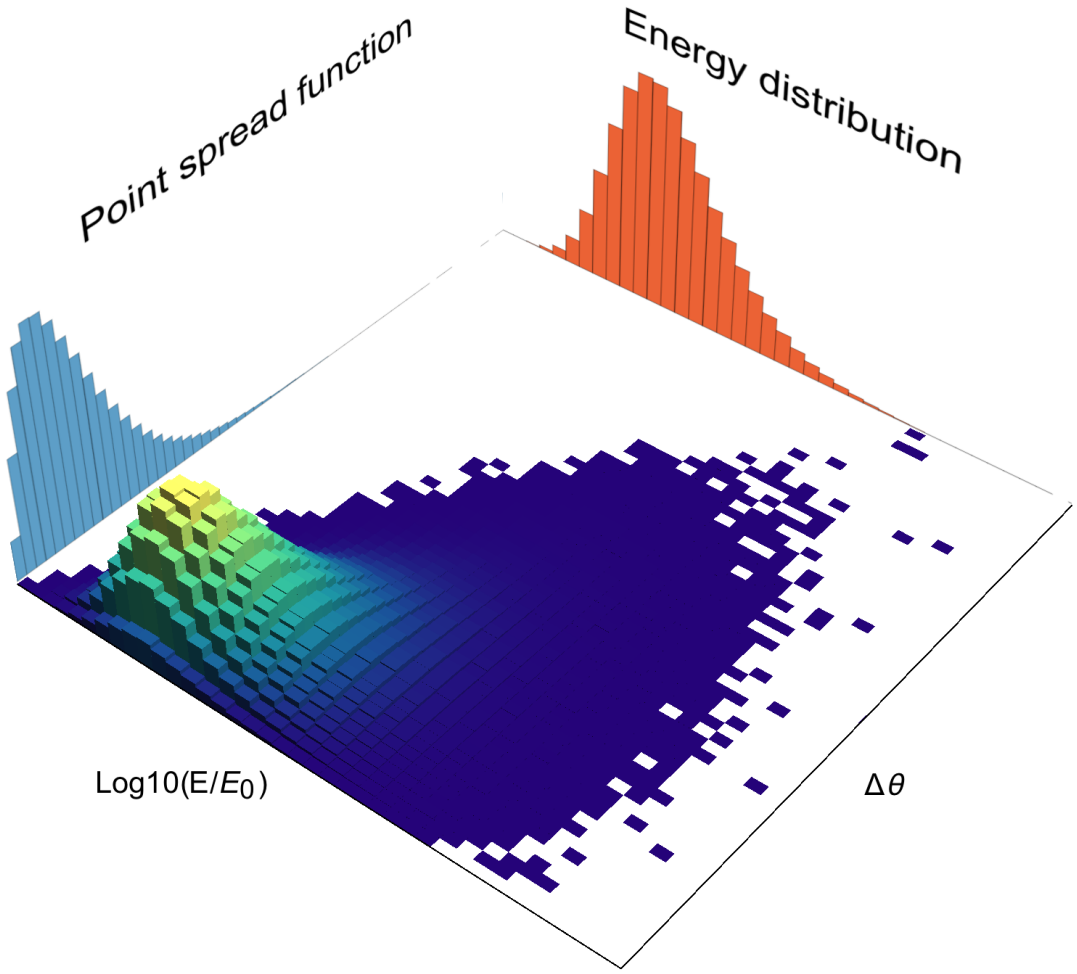

Figure 3.7: Example of a detector response matrix, a 2D histogram of the logarithm of the true energy (the constant E_0 is an arbitrary reference energy value) versus the angle reconstruction error $\Delta\theta$. The projected histograms, which are the sum of the 2D histogram in one dimension, provide us with the PSF and energy distribution. Note that they were artificially scaled to fit the plot. The sum of all bins corresponds to the total expected excess. This example doesn't correspond to real data and the units are arbitrary.

$$w = \frac{\Phi(\hat{E})}{\Psi(\hat{E})}\,, \tag{3.3}$$

where $\hat{E}$ is the energy of the center of the bin. Note that since we are weighting the sum of events instead of applying the weight event-by-event we introduce a numerical error. We chose the binning in energy fine enough (0.01 in log-space) such that this error is negligible ($\sim$1 % in flux).

The response of the experiment depends strongly on the zenith angle. The acceptance near zenith is greater, due to the atmosphere being thinner and the projected area of the detector being larger. The angular resolution also depends on the zenith angle and the size of the shower, as seen in Figure 2.11. Because of this we have a detector response matrix for each analysis bin $\mathcal{B}$ and each zenith range. For this work the zenith was arbitrarily divided into 10 zenith bins with the following edges: 0°, 9°, 13°, 17°, 20°, 24°, 27°, 30°, 34°, 40°, 50°. These were mostly chosen so that the response matrices were well populated based on the statistics on the available Monte Carlo simulation.

In order to avoid artifacts in the skymaps, the response at a given zenith angle is obtained by a linear interpolation between the nearest two zenith band centers —note that the center for the first zenith angle band is the zenith itself—. The PSF is interpolated as well as the total expected excess. For the former this means adding both histograms with a weight, proportional to the expected excess, and normalizing the result.

Unless we are simulating a short burst of a few seconds, we need to take into

account the zenith angles a source emits from as it transits our FOV. This is achieved by integrating over all the zenith angles the source transited:

$$\begin{aligned} \mathrm{N(RA, Dec)} &= \int \mathrm{on}\,(t)\,\frac{dN}{dt}\,(\theta(t))\,dt \\ &= \int \mathrm{on}\,(t)\,\frac{dN}{dt}(\mathrm{t} - \mathrm{RA}, \mathrm{Dec})dt\ , \end{aligned} \tag{3.4}$$

where N is the total expected excess for a source at a given (RA,Dec) coordinate; on$(t) = 1$ when we were taking data and is zero otherwise; dN/dt is the expected excess per unit time at a given zenith angle in the source path $\theta(t)$. This path can also be expressed in (RA,Dec) coordinates, in which case the declination remains constant and RA has a constant shift versus time. As the similarities of Eq. 3.1 and Eq. 3.4 suggest, this is implemented the same way as for direct integration, discussed in Section 3.1.3. That is, by convolving along HEALPix rings, with the uptime histogram explained in Sections 3.4 taking the role of the all-sky rate histogram. The PSF is obtained by weighting by the expected rate at a given zenith angle, that is

$$\mathrm{PSF}(r; \mathrm{RA}, \mathrm{Dec}) = \int \mathrm{on}\,(t)\,\frac{dN}{dt}\,(\theta(t))\,\mathrm{PSF}(r; \theta(t))dt\,, \tag{3.5}$$

where PSF(r) represents the probability of reconstructing an event at an angular distance r from the true position of the source.

3.3 Maximum likelihood analysis

Given a set of maps and a detector response, our first goal is to estimate the physical parameters of a source. We do this using a *forward-folding* technique,

that is, we take a hypothetical source with various physical parameters we want to determine and then convolve it with the detector response. We proceed to compare the result with the data and vary the parameters until we obtain the best fit. The best fit is defined by the values that maximize the likelihood function $\mathcal{L}(\mathbf{a};\mathbf{x})$, that is, the probability of obtaining a series of measurements $\mathbf{x}$ given a set of parameter values $\mathbf{a}$.

In our case the parameters can be source position, spatial extension, spectral index, normalization, etc. The measurements are the number of count in each pixel, p, in the map for each analysis bin $\mathcal{B}$ (see Section 2.6.1). For computational efficiency we only include the nearby pixels that can potentially matter. These counts d_i are independent from each other and Poisson distributed, therefore

$$\mathcal{L}(\mathbf{a};\mathbf{d}) = \prod_{\mathcal{B}}\prod_{p} \frac{(b_{\mathcal{B}p} + s_{\mathcal{B}p}(\mathbf{a}))^{d_{\mathcal{B}p}} \exp\left(-b_{\mathcal{B}p} - s_{\mathcal{B}p}(\mathbf{a})\right)}{d_{\mathcal{B}p}!}\,, \tag{3.6}$$

where $b_{\mathcal{B}p} + s_{\mathcal{B}p}(\mathbf{a})$ is the expected number of observed count given the parameters, with $b_{\mathcal{B}p}$ being the background counts estimated as discussed in Section 3.1.3 and $s_{\mathcal{B}p}$ the expected signal counts computed as discussed in Section 3.2.

The best estimate for the free parameters, $\hat{\mathbf{a}}$, correspond to the values that maximize the likelihood, that is

$$\max \mathcal{L}(\mathbf{a};\mathbf{d}) = \mathcal{L}(\hat{\mathbf{a}};\mathbf{d})\ . \tag{3.7}$$

Besides estimating a parameter, another common task is to compare a null model against an alternative. For example, to check if a source changed its spectral index during a flare, or check if a detected candidate is consistent with a previously

known source. To do this we look at the likelihood ratio between competing models:

$$TS = 2 \log \frac{\mathcal{L}(\hat{\mathbf{b}}; \mathbf{d})}{\mathcal{L}(\hat{\mathbf{a}}; \mathbf{d})} , \tag{3.8}$$

where $\mathbf{b}$ are the free parameters of the alternative model, and $\mathbf{a}$ those of the null hypothesis, which must be a subset of $\mathbf{b}$. In other words, the two model must be nested, which means that there is a set of values that reduce the alternative model to the null hypothesis.

TS stands for *test statistic*, and we use it to make decisions of whether or not the data is consistent with the null hypothesis. When the sample size approaches infinity, Wilks' theorem [68] guarantees TS becomes asymptotically distributed as a χ^2 distribution with a number of degrees of freedom equal to the difference in free parameters between the null and alternative hypothesis. A large sample size cannot always be assumed though, but nevertheless TS can still be used for decision making based on its simulated distribution. However, as we'll see in this work, even for our finite sample size case TS does not depart greatly from the Wilks' theorem prediction.

The case where the only free parameter is the flux normalization deserves a special mention as is the most used in this work. This happens when we are searching for the existence of a source against a background-only hypothesis and the details of the spectral shape are either known or not important. In a blind search, or when the uncertainty in time or position is large, we need to solve this case so many times that the minimizer algorithm needs to be optimized. In this case $s_i(\mathbf{a})$ can be expressed as $e_i f$, where e_i are constants and f is the flux normalization.

This simplification allows us to study analytically the properties of the likelihood function, and as explained in Appendix B, maximize TS with a very simple but at the same time very fast and robust method.

Assuming a source hypothesis and using the detector response while doing the search offers an increase in sensitivity with respect to a simpler cut-and-count analysis. On the latter, we would sum all the data and background values in the pixels near a testing location and sum the log-likelihoods of each analysis bin as if they were independent measurements. First, this involves discarding part of the signal, the tails of the PSF. Even choosing an optimal radius of integration there is a $\sim$10 % decrease in sensitivity because of this, as explained in Appendix C.1. Also, note that this would be equivalent to floating the normalization for each analysis bin $\mathcal{B}$, as opposed to forcing all values to be linked according to an assumed spectrum and floating only the normalization. This causes TS to be distributed approximately as a χ^2 with 9 degrees of freedom, instead of just one, increasing the threshold for a significant detection. In other words, the effective number of trials would increase since we would consider unphysical combinations of flux values for each analysis bin. As long as the assumed spectrum does not depart significantly from the real spectrum, it is better to use the detector response information in our search.

3.4 Search strategy

In the previous section we explained the method we used to test the hypothesis of the presence of a source over a background only hypothesis. When searching for

an unknown source, we typically assume a given spectral shape and let the flux normalization f float, with $f = 0$ being the null hypothesis. Eq. 3.6 simplifies to

$$\begin{aligned} TS(f) &= 2\log\frac{\mathcal{L}(\mathbf{b}=\{f\};\mathbf{d})}{\mathcal{L}(\mathbf{a}=\{f=0\};\mathbf{d})} \\ &= 2\sum\log\frac{(b_i+e_i f)^{d_i}\exp\left(-e_i f\right)}{b_i^n}\,. \end{aligned} \tag{3.9}$$

Using this formalism we integrate over a given period of time. f is the average flux normalization over that period, b_i is the total expected background for each pixel/analysis bin and d_i the integrated counts in that period. In general however, when we search for an unknown source we do not know the time or duration of the possible emission.

We use a sliding time window that is advanced by a fraction of its width each step. Oversampling improves the sensitivity of the search by increasing the probability of integrating the signal over the optimal time window. In order to do this efficiently, given a time window width δt, the size of the steps is always $\delta t/n$, where n is an integer. While the overlap between time windows could be arbitrary, a fractional overlap of $(n-1)/n$ allows for an implementation of a buffer where you can add or remove data from in time intervals of $\delta t/n$. A toy example for a simple counting experiment is shown in Figure 3.8.

After a TS value is computed for each step of the moving time window, we compute the independent local maxima. This is defined as a point in time such that there is no other local maximum with a greater TS value $n-1$ steps around. Two time windows that are apart by n steps are completely independent, as a single event could not have possibly be included in both.

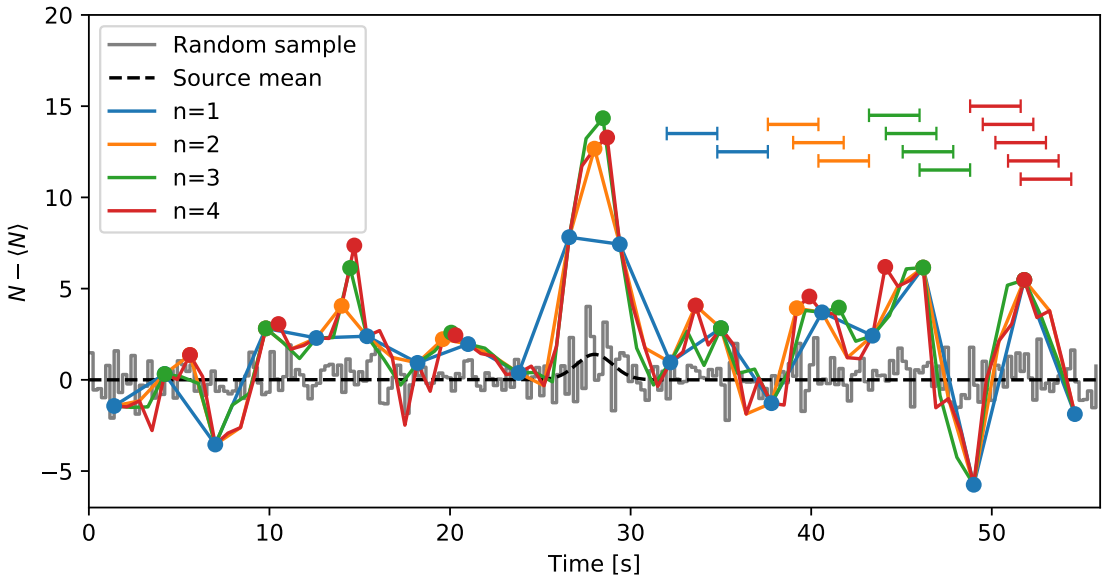

Figure 3.8: Sliding time window example for a simple counting experiment. This corresponds to a Gaussian background with a rate of 10 Hz, with a strong signal injected with a total of 15 counts and a standard normal distribution in time. The width of the time window was optimally chosen for a Gaussian signal (2.8 times the width, see Appendix C.2). This time window is slid in time in steps of $\delta t/n$ producing a moving sum, shown for $n = 1$, 2, 3 and 4. The independent relative maxima are shown for each n as points, which indicate that there is no other location with a greater value $n - 1$ steps around. In this toy example $TS = (N - \langle N \rangle)^2/B$, where B is the background rate times the width of the time window.

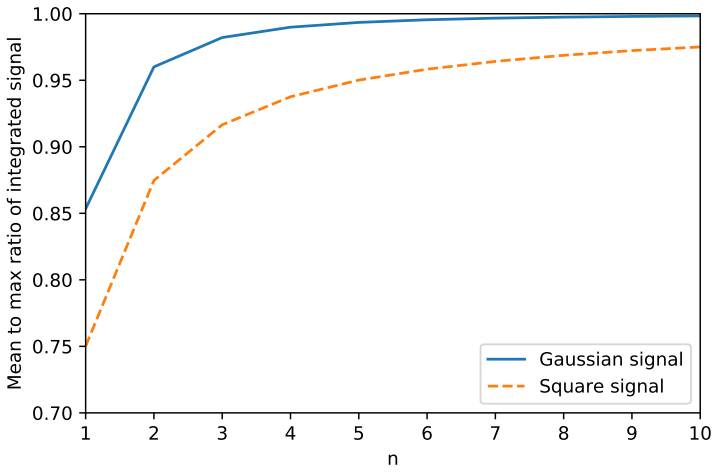

Figure 3.9: Ratio between the average and the maximum possible integrated signal in a time window versus the number of steps n per time window width. This is shown for a Gaussian and a square signal versus time. The optimal time window width was used for each case: 2.8 times the width of the Gaussian (see Appendix C.2), and the width of the square signal, respectively.

Having overlapping time windows rapidly increases the average signal you can expect to integrate in the best time window, increasing your chances of detecting a source. The actual improvement depends on the shape of the signal, in most cases unknown, but in general we can expect to have a big improvement using $n \sim 5$ and diminishing returns afterward. This is shown in Figure. 3.9.

Besides increasing the average integrated signal, having overlapping windows also increases the number of trials, which then increases the TS threshold needed for detection. For non-overlapping time windows the number of trials equals the

number of time windows searched. The false alarm rate (FAR) is then equal to

$$\mathrm{FAR}(x) = \frac{\Delta T}{\delta t}\mathrm{P}(TS > x)\,, \tag{3.10}$$

where ΔT is the total time period searched, δt is the width of the time window and $P(TS > x)$ is the probability of obtaining at least one event with a $TS > x$. In the Gaussian regime, using Wilks' theorem we know that $TS \sim \chi^2_{n=1} \sim \exp\left(-TS/2\right)$, so computing $P(TS > x)$ is straightforward.

When we have overlapping time windows the upper limit on the number of trials is the total number of steps, in which case we could multiply Eq. 3.10 by n. However since we are only considering independent local maxima and the neighbor time steps are highly correlated the FAR does not increase linearly with respect to Eq. 3.10 as we increase n. As exemplified in Fig. 3.10 the TS threshold rises slowly as we increase the number of steps per time window. Since the change in the mean flux threshold goes like $\sqrt{TS}$, the sensitivity of the search improves by having overlapping windows.

The motivation to run simulations to obtain the distribution of TS is twofold. On one side the effect of having overlapping time windows cannot simply be computed analytically. On the other, this accounts for the possibility that the TS distribution, even in the non-overlapping case, can deviate from Wilks' theorem when we have a small number of events.

One problem that arises however is that, due to limited computer resources, it might be difficult to simulate enough samples to have enough statistics up to the 5σ threshold. In order to remedy this we extrapolate the results using a χ^2 with

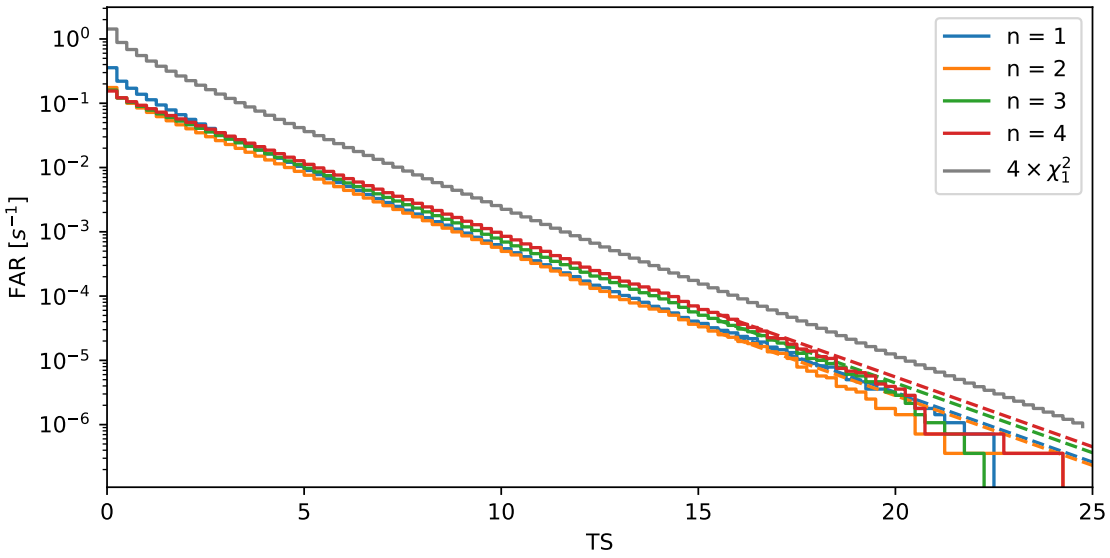

Figure 3.10: False alarm rate for the simple counting experiment shown in Figure 3.8. This was obtained by simulating a month of such pseudo-experiment, running a time sliding window with different overlaps and finding the independent local maxima. The dashed lines correspond to the $\chi^2_{k=2}$ extrapolation. The gray line corresponds to the conservative FAR obtained considering every time step as independent in an overlapping time window search with 4 steps per time window. Note that for $n > 1$ only independent local maxima are considered, which explains a slightly lower FAR than for $n = 1$ in some regimes, especially at low TS values.

a number of degrees of freedom equal to the free parameters in the search —e.g. NDF = 2 in this case, since we float the flux normalization and the point in time—, as it were in the regime where Wilks' theorem applies. The normalization is fixed to match the tails of the simulated results. While this approximation might not hold up for TS values much greater than the maximum simulated one, it is likely to hold up to the 5σ threshold. The precision of higher significance values is not important as a detection can be claimed in any case.

During a search, besides not knowing the time of the event, the sky localization uncertainty might be larger than the angular resolution of HAWC. In that case we repeat the analysis in a grid, specifically we change the source location hypothesis to be the center of each of the pixels in a HEALPix grid (see Section 3.1.1). Following the same principle as for overlapping time windows, we simulate this search on background-only randomly generated maps to obtain the FAR, which is lower than the conservative approach of assuming every pixels independent. An example is shown in Figure 3.11.

Figure 3.11 also contains the FAR for various timescales. Most of the time the exact shape of the signal is not known so we need to account for various possibilities. Due to limited computer resources, and the fact that the total searched time duration can be dependent on the timescale, we conservatively assume each timescale tried as an independent trial. After the analysis for all N timescales is done, we estimate the expected number of events $\langle n \rangle$ with a TS greater than a given independent local

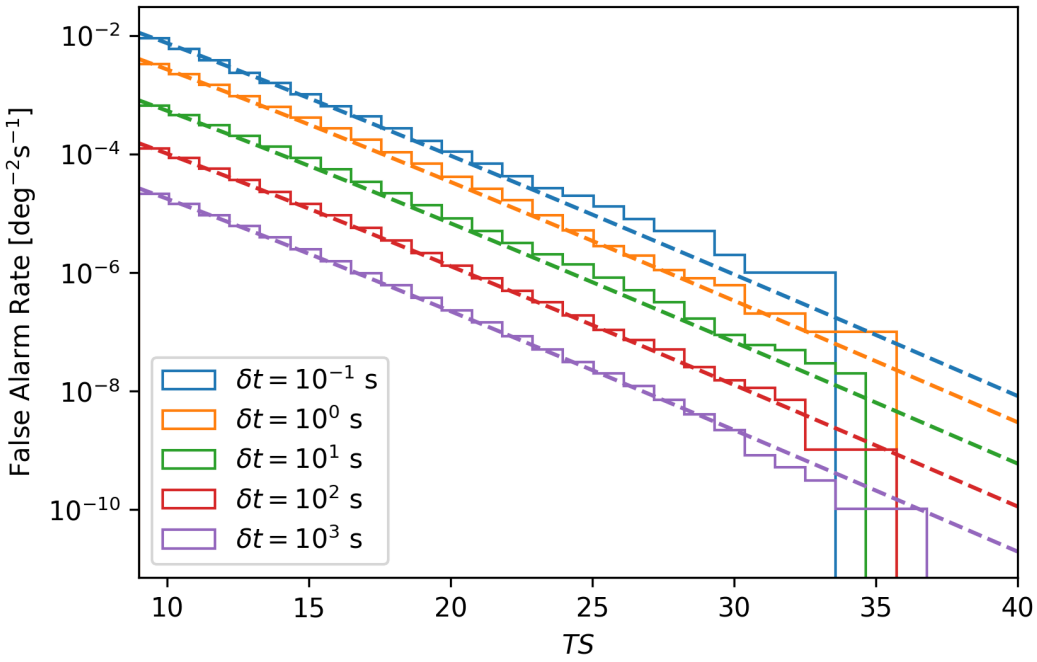

Figure 3.11: False alarm rate per solid angle are for various timescales. The dashed lines are the $\chi^2_{k=4}$ extrapolation. The FAR per δt is similar for every δt, but it deviated slightly in the regime where the probability of having at least one event is low. Due to the variable angular resolution versus zenith the FAR is higher for events near zenith. Since we have limited computed resources we perform this simulation only at zenith and therefore the results are conservative. This plot corresponds to time windows overlapping by 90% and HEALPix $N_{\text{side}} = 512$.

maximum for each timescale as

$$\langle n \rangle_{\delta t} = \mathrm{FAR}_{\delta t} \times \Delta T_{\delta t} \times A \times N \,, \tag{3.11}$$

where $\Delta T_{\delta T}$ is the total search duration for the timescale δt and A is the total search area —in the case of a grid search, where FAR is expressed per unit solid angle area—. Note that when $\langle n \rangle \ll 1$, then $\langle n \rangle$ is approximately the p-value —or a conservative higher value—. The significance S is then obtained by expressing the p-value in standard deviations using a standard normal cumulative distribution

$$S = \sqrt{2}\mathrm{erf}^{-1}(1 - 2p) \tag{3.12}$$

where erf^{-1} is the inverse of the error function and p is the p-value. A single tailed distribution is chosen since we only consider local maxima (not minima).

3.5 Flux upper limits

Even when a search returns a null result we can still estimate a range of flux values that are consistent with our data. In this work we take a frequentist approach and provide a confidence interval with a certain confidence level (C.L.) α such that, if the observations were to be repeated, a fraction α of the computed intervals would contain the true flux value. This is estimated by simulating the distribution of measured flux values obtained under the assumption of a given true flux value and then selecting a range that covers a fraction α of the distribution. We use the Feldman-Cousins ordering principle [69] to select this range, which consists off sorting in ascending order based on the ΔTS between the true flux value and

the value that maximizes TS. This is restricted to physically allowed values —i.e. positive flux. Figure 3.12 exemplifies this procedure. We report the upper bound of the confidence interval as an upper limit, and omit the lower bound as it is either exactly zero or negligible for a null detection.

Since we do a forward folding analysis, estimating the flux confidence interval requires us to assume a spectrum. When the spectrum choice is not clear we have two options. One is to report the limit at (or integrated from) a given *pivot energy*, a point that is not very sensitive to the spectral assumption. This is typically between 1–10 TeV.

Another possibility is to set *quasi-diferential* limits, that is, limits for various energy intervals. For each interval we assume a spectrum but require that the hypothetical source only emits in this energy range —i.e. we introduce hard cutoffs on both sides— and proceed to find the flux normalization bounds, as previously described. Although we assume a power law with an index of -2, because we use a narrow energy range (typically half a decade in energy) the result is very insensitive to the actual shape of the assumed spectrum. While doing a full forward-folding analysis and testing various models would result in better constraints, this provides spectrum-independent data points that can then be used by members of the community to test their own models.

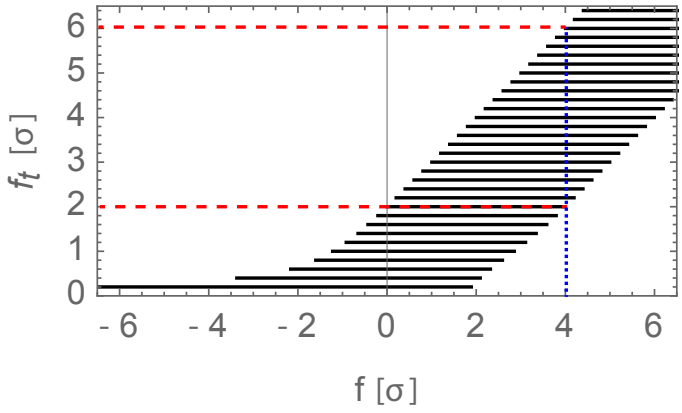

Figure 3.12: Example of Feldman-Cousins confidence band construction for the case when the flux f is distributed as a Gaussian of width σ. Each black horizontal bar represents the set of flux values that you would obtain 95 % of the time assuming a given true flux f_t. Note that there are various ways to satisfy this condition, the Feldman-Cousin prescription is to select the lowest possible ΔTS between f_t and a value f_{max} which maximizes TS within the physical bounds. In this case $f_{max} = f$ if $f \geq 0$ and $f_{max} = 0$ otherwise. The confidence interval (between the dashed red lines) for a given measured flux (at the blue dotted line) corresponds to the set of all f_t whose 95 % range includes the measured value. Note that for large flux values it becomes a standard central confidence interval (2σ around the measured value), while for low values and under-fluctuations the lower bound vanishes and the upper bound becomes a regular upper limit.

3.6 Summary

We presented a generalized multi-bin maximum likelihood ratio analysis to study HAWC data in arbitrary timescales, from a fraction of a second to years. It consists off a forward folding technique with takes the full response of the detector into account. The background is estimated using data. It can be used to fit multiple physical parameters of a source, such as flux, spectral shape and location. It can also be utilized to look for possible emission when either the time or the location is not known. In this case, an appropriate trials correction factor is applied. This analysis has been optimized to be able to run it on-site, and represents an improvement over previous cut-and-count analyses for short-timescales used by the HAWC Collaboration.

Chapter 4: Search for VHE gamma-ray counterparts of gravitational-wave events

As discussed in Sections 1.4.2 and 1.5.2, at least some gravitational waves are accompanied by the emission of gamma-rays. Motivated by this, in this chapter we present a search for VHE gamma-ray counterparts of gravitational waves events using HAWC data. These GW events were detected by LIGO and Virgo during the campaigns described in Section 4.1. In Section 4.2 we describe some details of this analysis, with the bulk of the data analysis framework already discussed in Chapter 3. Section 4.3 contains the sensitivity and expectations of this analysis, followed by the actual results and their discussion (Sections 4.4 and 4.5).

4.1 Gravitational wave data

We have followed up the gravitational wave events detected during three LIGO and Virgo observations runs. The first observing run (O1) took place from September 12th, 2015, until January 19th, 2016. During O1 only the two LIGO detectors participated, with a BNS rage of $\sim$60 Mpc. Three gravitational wave events were detected, all consistent with BBH mergers, including the first ever direct detection of gravitational waves: GW150914. These events were announced between February

and June, 2016.

The second observing run (O2) lasted from November 30th, 2016, to August 25th, 2017. During this period LIGO had a BNS range of 80–100 Mpc. The Virgo detector joined the observing run on August 1st, 2017, with a BNS range of ∼25 Mpc, enabling the possibility of considerably constraining the sky localization of some events. Eight gravitational wave events were detected, including the first BNS merger, GW170817, whose electromagnetic counterpart was successfully followed by many observatories. This was possible thanks to the efforts during this run to rapidly communicate, after human vetting, the detection of events to a network of electromagnetic observers (including HAWC). The events detected during O1 and O2 are part of the GWTC-1 catalog [70], which includes events that were not previously disseminated to the network of electromagnetic observers.

The third observing run (O3) started on April 1st, 2019, and is still ongoing at the time of this work. LIGO-Livingston has been operating with a BNS sensitivity of ∼140 Mpc, LIGO-Hanford at ∼110 Mpc and Virgo at ∼50 Mpc. During this observing run the LIGO Scientific Collaboration and Virgo Collaboration (LVC) have provided public alerts when they detect an event. Also, automatic preliminary alerts are sent with a low latency of a few minutes, which might later be retracted after human vetting. These events are named with a preliminary suffix "S", after *superevent*, which indicates they each are a collection of the different events detected by more than one analysis pipeline believed to correspond to the same source.

In this work we present the HAWC follow-up of all the 11 events in GWTC-1, as well as any confirmed O3 superevent announced through the Gamma-ray Co-

ordinates Network (GCN). In total there are 25 announced events. From these, GW170817 and S190425z are firmly associated with a BNS merger with a high signal-to-noise ratio; S190510g is also associated with a BNS merger, although there is a 58 % chance of being caused by noise due to its low signal-to-noise ratio; the nature of S190426c is not clear, while there is a strong evidence for one of the component being a neutron star, it is not clear if the companion is also a neutron start of a black hole. All other events are consistent with BBH mergers. This is summarized in Tables 4.1 and 4.2.

For the events in GWTC-1 the sky localization and distance estimation provided in the supplemental material is used. The latest publicly available estimations by LVC as of June 1st, 2019, were used for the O3 superevents.

4.2 Analysis

In this analysis we look for localized short-duration emission inconsistent with the smooth and relatively constant cosmic-ray background. As discussed in Section 2.6.1, we separate our data into 9 analysis bins based on the number of channels that detect light from a shower, which is a proxy for their energy and quality (angular resolution and gamma-hadron separation power). Gamma-hadron separation cuts are applied on each set of events, as defined in Table 2.1. The residual background was computed by convolving the normalized arrival distribution in local coordinates with the all-sky rate versus time, as described in Section 3.1.3. Due to the short timescales searched and the low rate of events passing the gamma-hadron separation

GW event	Progenitor	t_0 [UTC]	Zenith RA [deg]	Probability in FoV	Area analyzed [deg]
GW150914	BBH	09:50:45.4	43.2	0 %	0
GW151012	BBH	09:54:43.44	71.8	39 %	672
GW151226	BBH	03:38:53.64	51.5	32 %	441
GW170104	BBH	10:11:58.60	159.7	49 %	349
GW170608	BBH	02:01:16.50	189.4	0 %	0
GW170729	BBH	18:56:29.30	134.2	5 %	409
GW170809	BBH	08:28:21.75	347.6	1 %	27
GW170814	BBH	10:30:43.53	23.2	0 %	0
GW170817	BNS	12:41:04.42	58.8	0 %	0
GW170818	BBH	02:25:09.08	265.4	0 %	0
GW170823	BBH	13:13:58.51	73.0	30 %	640

Table 4.1: Summary of gravitational wave events during O1 and O2. "Zenith RA" corresponds to the right ascension of HAWC zenith at the time of the trigger (the declination is constant, 19.0°). We include the integrated sky localization probability in the area we analyzed (95 % GW sky localization probability containment and 45° from zenith), as well as the solid angle area it covered.

GW event	Progenitor	t_0 [UTC]	Zenith RA [deg]	Probability in FoV	Area analyzed [deg]
S190408an	BBH	18:18:02.28	13.7	80 %	375
S190412m	BBH	05:30:44.16	185.3	95 %	211
S190421ar	BBH	21:38:56.24	76.8	0 %	0
S190425z	BNS	08:18:05.01	240.1	25 %	3502
S190426c	BNS (49 %) mass gap (24 %) NSBH (13 %) noise (13 %)	15:21:55.35	347.3	28 %	314
S190503bf	BBH	18:54:04.28	47.3	1 %	10
S190510g	BNS (42 %) noise (58 %)	02:59:39.28	175.0	4 %	772
S190512at	BBH	18:07:14.40	44.5	0 %	0
S190513bm	BBH	20:54:28.74	87.4	46 %	407
S190517h	BBH	05:51:01.83	224.9	22 %	391
S190519bj	BBH	15:35:44.39	13.4	75 %	746
S190521g	BBH	03:02:29.45	186.5	46 %	378
S190521r	BBH	07:43:59.46	257.1	70 %	441
S190602aq	BBH	17:59:27.09	63.2	55 %	919

Table 4.2: Summary of gravitational wave events during O3 at the time of this work See also Table 4.1. The probabilities for different progenitors are listed when there is not a clear candidate.

cuts, the all-sky rate was averaged over a bin-dependent period of time around each analyzed time window —2 min for $\mathcal{B} = 1 - 5$, 8 min for $\mathcal{B} = 6$, 13 min for $\mathcal{B} = 7$, 50 min for $\mathcal{B} = 8$ and 30 min for $\mathcal{B} = 9$— which achieves at least a <10 % statistical error in the background estimation.

We searched using eight time window widths, $\Delta t = 0.3\,\mathrm{s}$, 1 s, 3 s, 10 s, 30 s, 100 s, 300 s and 1000 s. These are motivated by the typical GRB timescales observed in high-energy gamma rays. They were chosen to be separated by around half-decade to account for the uncertainty in the typical timescale at VHE. The time windows are shifted by $0.2\Delta t$, as explained in Section 3.4, starting at $t_0 - 5\Delta t$ and stopping at $t_0 + 10\Delta t$, where t_0 corresponds to the time of coalescence of the binary merger. This assumes the emission duration is of a similar order of magnitude as the delay with respect to the coalescence. Also, short duration events happening after a large delay would be hard to statistically link to the GW observations. While we expect gamma-ray emission to occur after coalescence, we analyze also a period of time previous to the GW trigger to allow for possible unexpected phenomena.

Using the maximum likelihood analysis described in Section 3.3 we search in the region that contains 95 % of the GW sky localization posterior probability, and is within the HAWC FoV —defined here as between 45° from zenith—. This is done by changing the location of the source hypothesis on each pixel of a HEALPix grid with a spacing of ∼0.11° (see Section 3.1.1). Figures 4.1 and 4.3a show the HAWC FoV in comparison with a typical and a well-localized event, respectively. We assume a spectral index of -2, consistent with Fermi-LAT measurements [22], and consider EBL attenuation according to the distance estimate provided by the

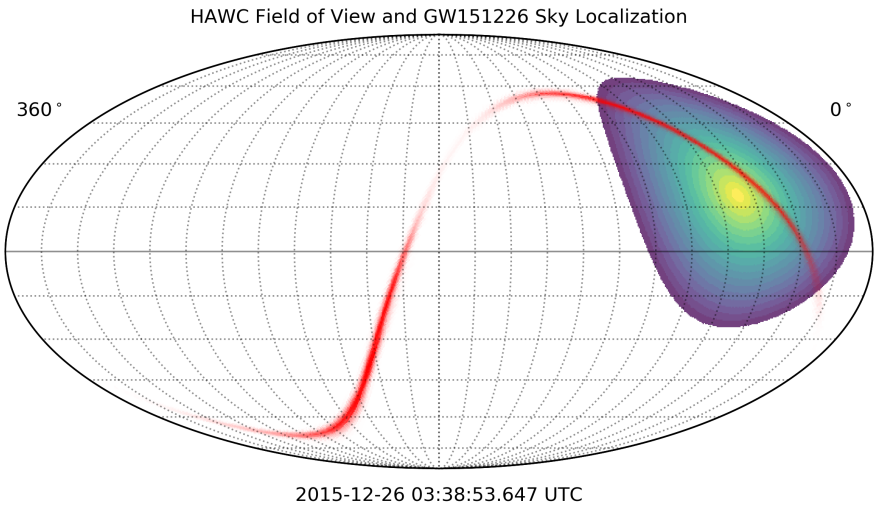

Figure 4.1: Sky Localization of GW151226 and the HAWC field of view at trigger time. The red region represents the GW event location, with a transparency proportional to quantile of the contained probability up to a given sky location starting from the most probable coordinate. This is the typical shape and area for the localization of a high signal-to-noise event contained only by two detectors. The disc represents the HAWC FoV at the time of the trigger, which is moving left (colors are arbitrary but indicate that the HAWC sensitivity decreases as we move away from zenith).

LVC.

The total number of trials from the search on each timescale are corrected for using simulation, as explained in Section 3.4. This takes into account the fact that the results between contiguous time windows and neighbors pixels are not independent. However, due to limited computer resources the trials from the different timescales are considered independent. Due to the same constrains, the effect of the trials is computed using our point spread function at zenith, were we have the best

Figure 4.2: Sky Localization of GW170817 and the HAWC field of view at trigger time. This is a BNS well localized event (using three detectors). The color convention is the same as in Fig. 4.1, and in addition the black dot represents the actual location as determined by its optical counterpart. The location entered the HAWC field of view 8.2 hrs after the trigger.

angular resolution. The effect of these two choices result in a p-value conservative by a factor of $\sim$2 , which has only small impact in our sensitivity[1].

Since the start of O3 this analysis is performed automatically on-site after receiving a GCN Notice. The latency is of a few minutes to $\sim$30 min depending on area covered by the GW sky localization. The HAWC Collaboration routinely informs the community of these results in a timely manner through GCN Circulars. The goal of the online analysis is to support the search of small field of view instruments, specially in the case of a detection.

We do not present an analysis here for events which sky localization did not overlap with the HAWC FoV at the time of the GW trigger, except for GW170817. The exception is motivated by the fact that it was a BNS merger which electromagnetic counterpart has been well-studied from radio to gamma-rays. We analyze this event integrating the data during the following transit starting $\sim$8.2 hrs after

[1]For example, assuming no trials, there is a factor of 2 in p-value for $\sqrt{TS} = 5$ and $\sqrt{TS} = 5.13$. This difference is even lower for the higher threshold required by trials. Since the flux is proportional to $\sqrt{TS}$, this shows there is no impact in sensitivity by being being conservative even by a factor of $\sim$2 in our false alarm rate estimation.

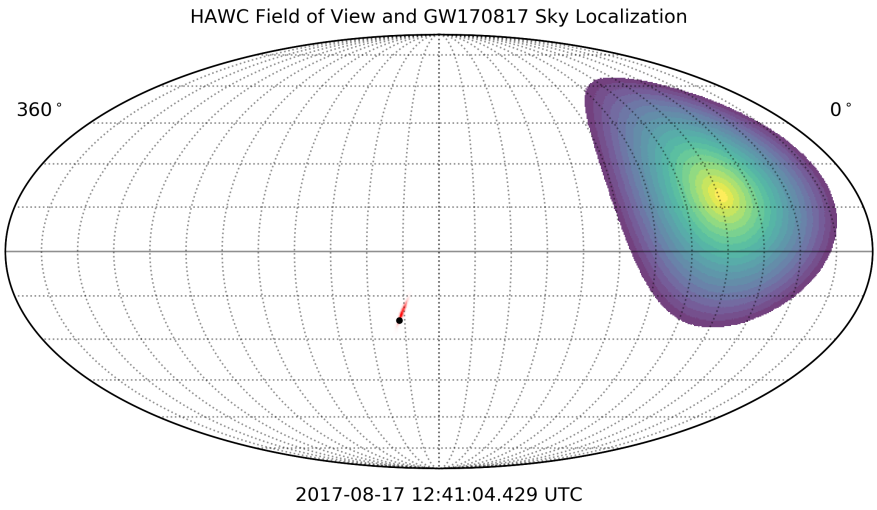

(a)

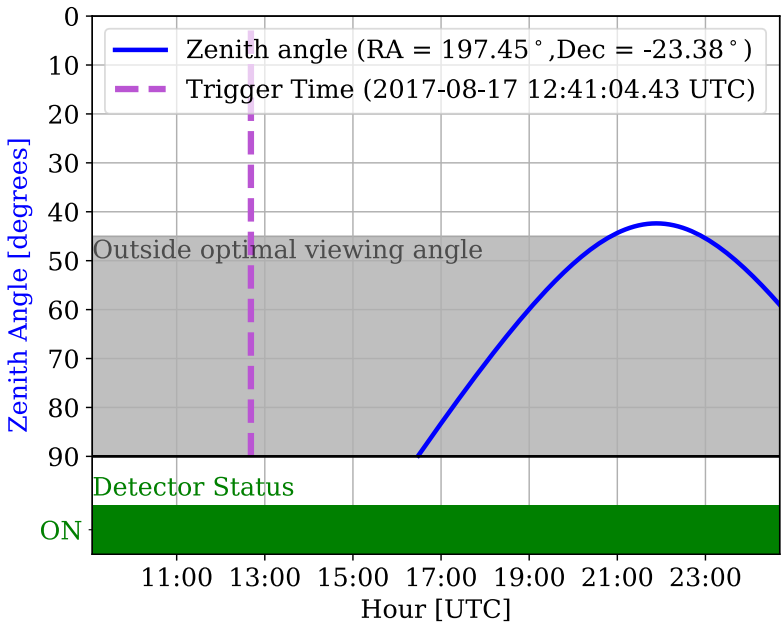

(b)

Figure 4.3: **(a)** Sky Localization of GW170817 and the HAWC field of view at trigger time. This is a BNS well localized event (using three detectors). The color convention is the same as in Fig. 4.1, and in addition the black dot represents the actual location as determined by its optical counterpart. The location transited briefly the edge of the HAWC field of view 8.2–10.23 hrs after the trigger, as shown in **(b)**.

coalescence (see Figure 4.3b).

4.3 Sensitivity and expectations

Here we explore the chances of HAWC of detecting a counterpart of a gravitational wave event. The most likely scenario for such detection is the BNS merger with a axis of rotation approximately aligned with the line of sight, which would be seen as a short GRB (see Section 1.4.2). It is not clear what is the typical timescale of the prompt emission for such signal at VHE, as it has never been measured. However, in order to get a sense of the HAWC capabilities compared to past measurements, in Figures 4.4 and 4.5 we show the sensitivity to 1s and 100s burst compared to Fermi-LAT observations.

Since the sensitivity of HAWC varies greatly versus energy, and its energy range is in a regime where a cutoff is expected, either intrinsic or due to EBL, we compute a quasi-differential sensitivity in half-decade intervals. We conservatively assume that the source only emits over a half-decade window in energy and define the sensitivity as the flux in this interval that would result in a $\sqrt{TS} > 5$ detection at least 50 % of the time. A spectrum with a index of -2 was assumed, but since the energy windows are narrow the results depend only very weakly on this assumption. These values are computed also for various zenith angles.

In order to make sense of these values we compared them with the short GRBs published in the second Fermi-LAT GRB catalog [71]. It comprises ten years of data and 186 events, although only 17 are short GRBs. The Fermi Collaboration

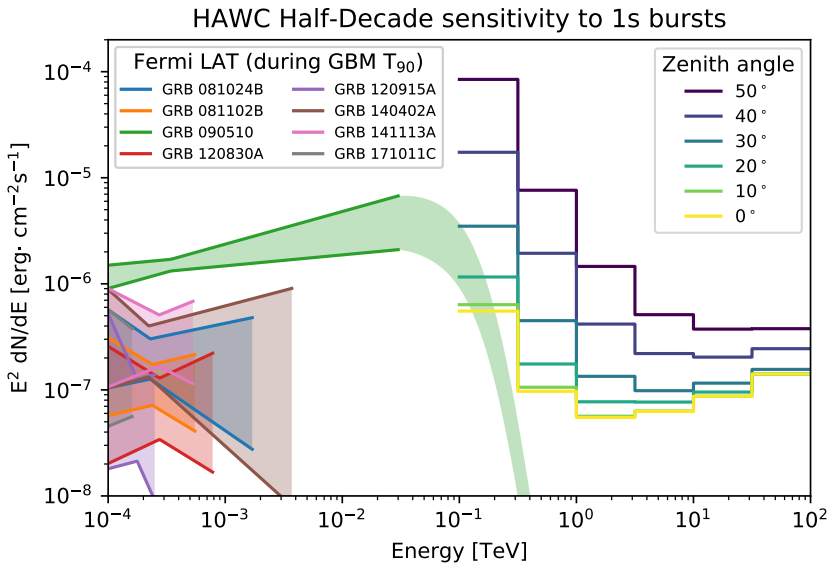

Figure 4.4: HAWC quasi-differential sensitivity to 1s bursts as a function of the zenith angle, defined as the mean flux in a given half-decade that would result in at least a 5σ detection half of the time. For reference we include the spectrum for the short GRBs detected by the Fermi-LAT as measured in the Fermi-GBM T90 window, which is of the order of 1s, reported in [71]. The redshift is known only for GRB 090510 ($z = 0.9$); its spectrum was extrapolated using a simple power law and attenuated by EBL.

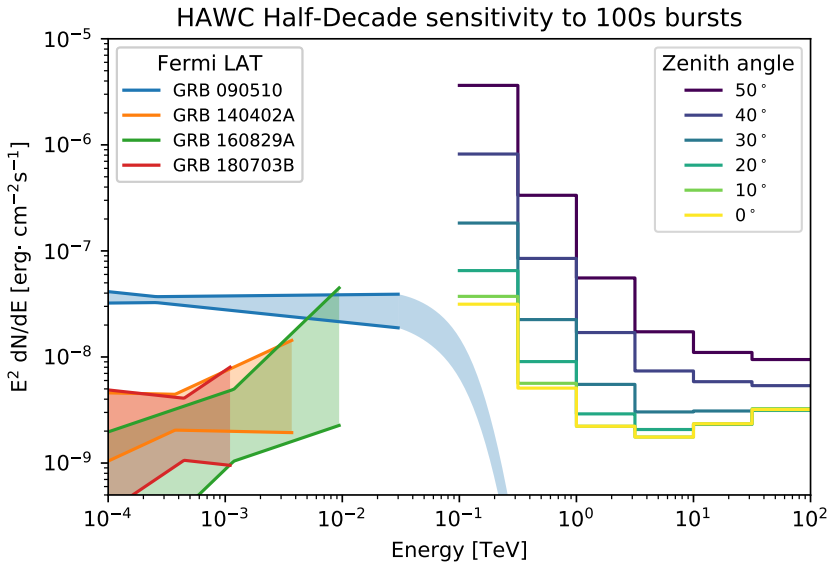

Figure 4.5: HAWC quasi-differential sensitivity to 100s bursts. Similar to Figure 4.4, but here we show for reference the spectra measured by the Fermi-LAT for GRBs with a duration >70 s (the longest being 170 s).

reported the measured spectrum during various time windows, here we consider the GBM T_{90} —containing 90 % of the emission detected by the GMB— and the LAT time window —the time between the first and last event detected associated with the burst. In Figure 4.4 we compare the 1 s burst sensitivity to the Fermi-LAT spectrum measured in the GRB T_{90} window. We chose this reported value over the one in the LAT time window since the latter is not necessarily optimal for HAWC. Although the number of passing events is low for these timescales, HAWC is still background dominated and is more sensitive to the peak flux rather than the total fluence. Note that since the emission detected by Fermi-LAT is typically delayed compared to the one measured by Fermi-GBM, this is not expected to be the optimal 1 s window. Roughly half of the short GRBs do not have a measured HE emission

during this period. In Figure 4.5 we compare the 100 s burst sensitivity to GRBs with a duration in the LAT time window between >70 s.

It is not straightforward to extrapolate the spectrum measured by Fermi-LAT into the HAWC energy range. Except for GRB 090510, the range for which Fermi-LAT measurements are constraining is at least an order of magnitude below, and there could be an intrinsic cutoff in the VHE range. GRB 090510 is also the only one whose redshift has been measured ($z = 0.9$). For this GRB we show the extrapolated spectrum assuming only attenuation by EBL. We can see that a good portion of the short GRBs could have been detected by HAWC if they had happened at a favorable zenith angle and there were neither an intrinsic nor extrinsic attenuation. In addition to EBL not playing an important role for GRBs occurring in the BNS range of current gravitational wave detectors, one could reasonably expect that nearby GRBs of this kind would result in an observed flux one or two orders of magnitude higher than typical short GRBs, which are ten times farther (see 4.6). This last conjecture might not stand though, as shown by GRB 170817A for which Fermi-GBM recorded an ordinary flux [72] in spite of being the closest GRB with a measured distance to date. Despite these caveats, this shows that for a short GRB occurring in the volume detectable by LIGO-Virgo and in the HAWC FoV, we should be able to either detect it or set a meaningful constraint.

In order to see how often this can happen, first let us consider the current BNS range of the LIGO detector, 140 Mpc. While this is the average over all possible orientation, a BNS accompanied by a GRB should be pointing towards the Earth, which means that horizon for such event is ∼1.5 times further (see Figure 1.9b),

about 210 Mpc ($z = 0.046$)[2]. It remains to see how many short GRBs occur within this distance.

The local rate of short GRB can be estimated based on the rate of BNS mergers and average jet opening angle, both of which are not precisely known. The detection of GW170817 sets a local BNS merge rate of 110–3840 $\mathrm{Gpc^{-3}yr^{-1}}$ [70]. This is consistent with previous estimates based on galactic binary pulsars of 10–10^4 $\mathrm{Gpc^{-3}yr^{-1}}$ [73]. The opening angles for short GRBs, measured by identifiying a jet break during the X-rays afterglow [74], is on average $\sim 6°$ [3] —albeit the sample is very small ($N = 10$). Using the BNS merger rate and the average opening angle we can estimate a local rate of short GRBs to be between 0.3 $\mathrm{Gpc^{-3}yr^{-1}}$ and 10 $\mathrm{Gpc^{-3}yr^{-1}}$. This is mostly consistent with the redshift distribution of short GRBs detected by Swift shown in Figure 4.6.

Using the short GRB rate and the LIGO BNS range during O3 we can estimate that a rate of gravitational waves accompanied by GRBs of 0.01–0.4 $\mathrm{yr^{-1}}$. Considering the size of the HAWC FoV —covering 15 % of the sky—, the simultaneous observation rate is 0.001–0.06 $\mathrm{yr^{-1}}$. While admittedly a small number, this search is merited based on the scientific value of a single of such events and the fact that HAWC is the only VHE gamma-ray observatory currently operating with a wide field of view.

[2]Note that HAWC detects Markarian 421 and Markarian 501 [62], which are at a similar distance ($z = 0.031$ and $z = 0.033$ respectively)

[3]Note that the detection of GRB 170817A has led to consider off-axis emission, from viewing angles as wide as $\sim 30°$. See [75] and references therein.

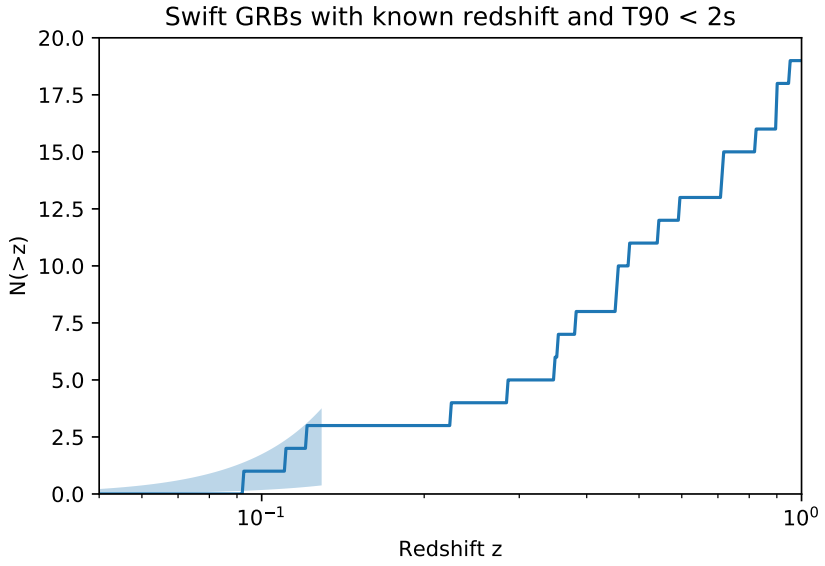

Figure 4.6: Redshift distribution of short GRBs detected by Swift over 14.5 yrs [76]. The shaded area corresponds to expected number of detections based on a local rate of short GRBs between $1\,\mathrm{Gpc^{-3}yr^{-1}}$ and $10\,\mathrm{Gpc^{-3}yr^{-1}}$. This accounts for the field of view of Swift and the fraction of GRBs with unknown redshift. It assumes $N(>z) \propto z^3$, which is only valid for short distances.

4.4 Results

HAWC was taking data in normal operations during all gravitational wave events detected by LIGO and Virgo during O1, O2 and O3. Out of 25, the sky localization for 18 has at least a partial overlap with the HAWC FoV. The area and the percentage of the sky localization probability distribution observed for each one of them is summarized in Tables 4.1 and 4.2.

The results for all 18 events that were analyzed are consistent with expectations from background. The upper-limits we can set depend by orders of magnitudes on the specific location of interest (highly dependent on zenith angle), the energy range, the timescale and the point in time. However, the maximum $\sqrt{TS}$ at any location, time, event or timescale was $\sqrt{TS} = 5.1$ (p-value of 1.0 after trials) which corresponds to a 95 % UL of no more than a factor of 1.5 greater than sensitivity shown in Figures 4.4 and 4.5. In terms of fluence between 0.1–1 TeV, the upper limit varies between $2 \times 10^{-7}\,\mathrm{erg\,cm^{-2}}$ —at zenith, $\Delta t = 0.3s$— and $3 \times 10^{-4}\,\mathrm{erg\,cm^{-2}}$ — 45° zenith angle, $\Delta t = 1000s$—

The location of GW170817 (RA,Dec = 197.45°,−23.3815°), on the other hand, is known to a high precision since the electromagnetic counterpart was found. However, this location was not in our FoV at the time of coalescence (see Figure 4.3a). We search for emission from this location during the immediate transit following the GW trigger, from t_0+8.20 hrs to t_0+10.23 hrs. Note that this location transited at the edge of our FoV, which causes a reduced sensitivity and limited observation time. The result was consistent with background. We set an upper limit of

$1.5 \times 10^{-8}\,\mathrm{ergs\,cm^{-2}\,s^{-1}}$ between 100 GeV and 1 TeV during this period and compare it to other short GRBs detected by Fermi-LAT in Figure 4.7.

4.5 Discussion

We have shown that HAWC has the sensitivity to either detect or meaningfully constrain the VHE gamma-ray emission of possible counterparts of gravitational waves between the LIGO and Virgo binary neutron star merger range. We have performed a search in short timescales for such counterparts on the 18 events which sky localization overlapped with our FoV, out of the 25 events announced by the LIGO-Virgo between September 12th, 2015, and June 1st, 2019. No significant excess was observed.

The non-detection of a VHE gamma-ray counterpart is however consistent with expectations as the intrinsic rate of GRBs associated with a GW event is $<1\,\mathrm{yr^{-1}}$. GW170817 is the only event with an electromagnetic counterpart identified so far, and was not in the HAWC field of view. We placed upper limits for the emission between 8.20 hrs and 10.23 hrs after the gravitational wave trigger. These are consistent with the extrapolation of high-energy measurement by Fermi-LAT.

Starting the observation run O3, this analysis was performed automatically at the HAWC site with a latency of the order of minutes after the alert is received. As a wide-field-of-view HAWC can potentially promptly constrain the sky localization from tens or hundreds of squared degrees to $<1\,\mathrm{deg^2}$, helping the observation of the electromagnetic counterpart by sensitive narrow field of view instruments at various

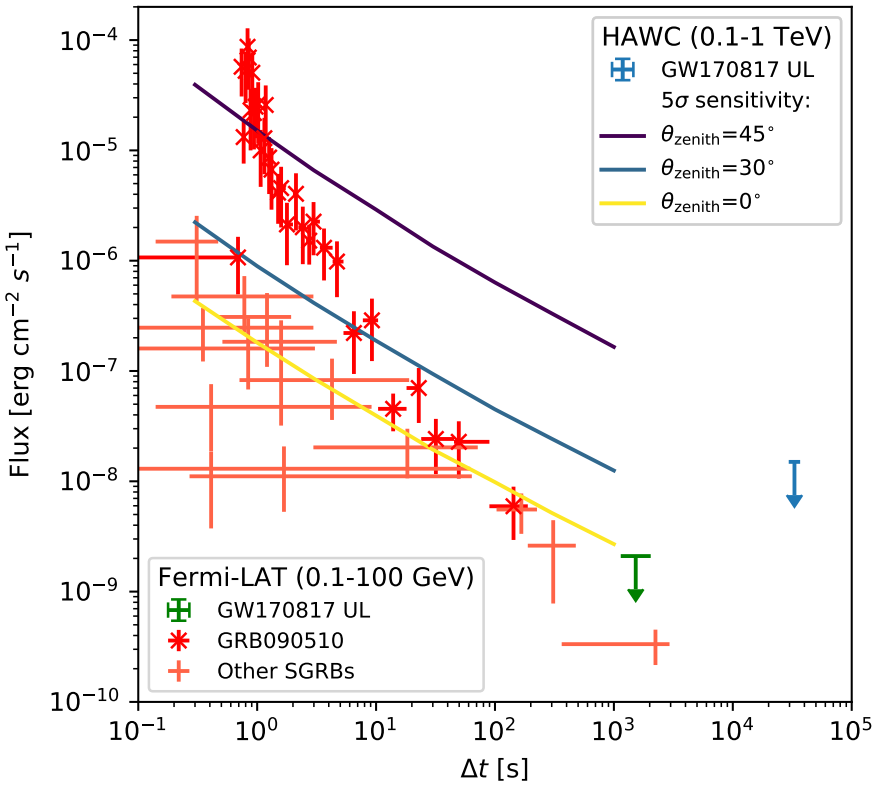

Figure 4.7: HAWC 95 % C.I. upper bound on GW170817 between 100 GeV and 1 TeV during the following transit (blue), from $\Delta t = t - t_0 = 8.20$ hrs to $\Delta t = 10.23$ hrs where t_0 is the time of coalescence. This is compared to the Fermi-LAT UL between 100 MeV and 100 GeV (green) between Δt =1153 s to Δt =2027 s, and Fermi-LAT measurements for previously detected short GRBs (red) [77]. The multiple Fermi-LAT measurements of GRB090510 are highlighted. The HAWC sensitivity (0.1–1 TeV) is shown as a function of the width Δt of the search time window.

wavelength. These efforts will continue.

Chapter 5: Search for VHE gamma-ray emission from the neutrino source candidate TXS 0506+056

In Sections 1.4.1 we describe how hadronic models of active galactic nuclei (AGN) predict the emission of neutrinos accompanying gamma rays, and the connection that this implies for the sources of charged cosmic rays. Also in Section 1.5.1 we discussed the difficulty of resolving neutrino sources, which led to efforts to correlate them in time with transient gamma rays. The correlation of a high energy neutrino with a gamma-ray flare from the blazar TXS 0506+056, reviewed in Section 5.1, represents the most notable result of these efforts to this date.

Prompted by these observations, in this chapter we use HAWC data to look for VHE gamma-ray emission from the direction of TXS 0506+056, both around the time of detection of this high energy neutrino and from a lower energy neutrino flare found in archival data starting in 2014. The latter search illustrates some unique capabilities of HAWC, enabled through its wide field of view and high duty cycle, as no other VHE gamma-ray experiment collected simultaneous data.

5.1 Neutrino flares from the direction of the blazar TXS 0506+056

On September 22nd, 2017, 20:54:30 UTC, IceCube detected a very-high energy ($\sim$290 TeV) track-like neutrino (IceCube-170922A) localized at (RA, Dec = $77.43^{+0.95}_{-0.65}$ deg, $+5.72^{+0.50}_{-0.30}$ deg) [78]. Shortly after, the community was alerted [79]. A few hours later Fermi-LAT reported that one of the sources they had previously detected, TXS 0506+056 (RA, Dec = (77.35°, 5.69°), $z = 0.336$ [80]), was consistent with the location reported by IceCube and was showing a flaring state above 100 MeV starting in April 2017 [81]. The chances of a random coincidence between a gamma-ray flare and a high energy neutrino such as this was estimated to be 3σ based on previous neutrino alerts and the frequency of similar flares [78].

This prompted observations from several other observatories at multiple wavelengths. In particular, it was detected by MAGIC at VHE (>400 GeV) from September 28th to October 4th, 2017. Observations after October 4th were prevented by the full Moon, and when they resumed observations of this source on October 18th it was found in a low state [82]. VERITAS and HESS also performed follow-up observation during this period, but did not detect the source. However, VERITAS continued observing up to February 6, 2018, and finally detected it with a data set 35 hours long [83].

Motivated by this, the IceCube collaboration looked at archival data for other neutrinos from the direction of TXS 0506+056 [84]. No other neutrino that would have passed the selection criteria for a high energy alert such as the one from September 22nd, 2017 was found. However, they also performed a maximum likelihood

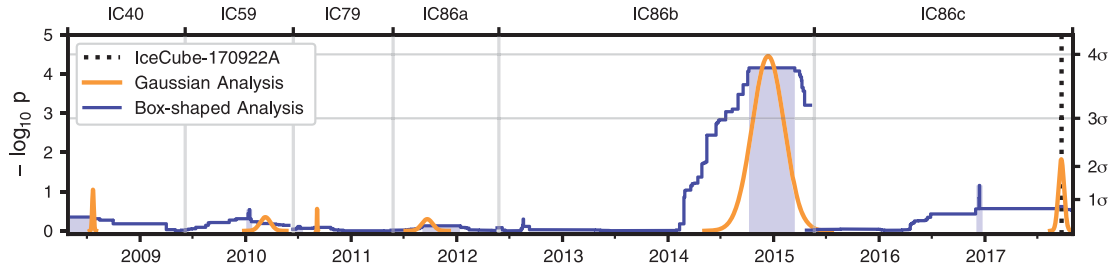

Figure 5.1: IceCube time dependent flare analysis of TXS 0506+056. The orange curves correspond to best fit Gaussian-shaped profiles, with the height indicating the p-value. The blue curve corresponds to the edges of the box-shaped fitted windows centered at different points in time, with a shaded region highlithing the most significant window. The different time periods correspond to the varying size of the detector, data-taking condition and event selection. Reproduced from [84].

analysis including lower energy events and assuming a source hypothesis at the location of TXS 0506+056. As shown in Figure 5.1, another neutrino flare was found starting late 2014 with a significance of 3.5σ post-trials. Two hypotheses for the distribution of emission versus time were used, Gaussian and box shaped. In the latter, the flare is estimated to start on October 7, 2014 and end on March 15, 2015.

During this period of time however there was no elevated emission in Fermi-LAT data [85]. There are no VHE observations by IACTs during this period. In the following section we present the results of the HAWC observations.

5.2 HAWC observations

The sky location of the IceCube neutrino IC-170922A was not in the field of view of HAWC at the time of the trigger. After receiving the alert we searched in three time windows. First, integrating the transit before and after the alert (from September 22, 2017 08:37 UTC to September 23, 2017 14:25 UTC). Second, from September 9, 2017 09:28 to October 6, 2017 13:34, except from September 19, 2017 14:41 to September 21, 2017 08:41. The gap in data taking was caused by a power outage due to an earthquake near the HAWC site. This period of time was chosen based on the reported flare period by Fermi-LAT. Third, we integrated our archival data, from November 26, 2014 to August 27, 2017. No excess was found on any timescale. Assuming a power law with an index of -3.9 (reported by MAGIC) these observations set 95 % CL limits on the integral flux >1 TeV of $3.6 \times 10^{-12}\,\mathrm{cm}^{-2}\mathrm{s}^{-1}$, $2.1 \times 10^{-12}\,\mathrm{cm}^{-2}\mathrm{s}^{-1}$ and $1.6 \times 10^{-13}\,\mathrm{cm}^{-2}\mathrm{s}^{-1}$, respectively. Also, limits for half-decade intervals in energy are shown in Figure 5.2 for the last two described periods. Under the same assumption, our updated archival limit from 26 November, 2014 to May 23, 2018, is $8.2 \times 10^{-14}\,\mathrm{cm}^{-2}\mathrm{s}^{-1}$.

We also analyzed the neutrino flare found in archival data from October 7, 2014 to March 15, 2015 (box-like analysis). Although HAWC took data since the start of this period, data previous to 26 November, 2014 correspond to an incomplete HAWC detector with changing configurations. We therefore analyzed the data from November 26, 2014 to March 15, 2015, over which the detector operated with a duty cycle of 94 % for a total observation time of 609.72 hrs. We found no significant

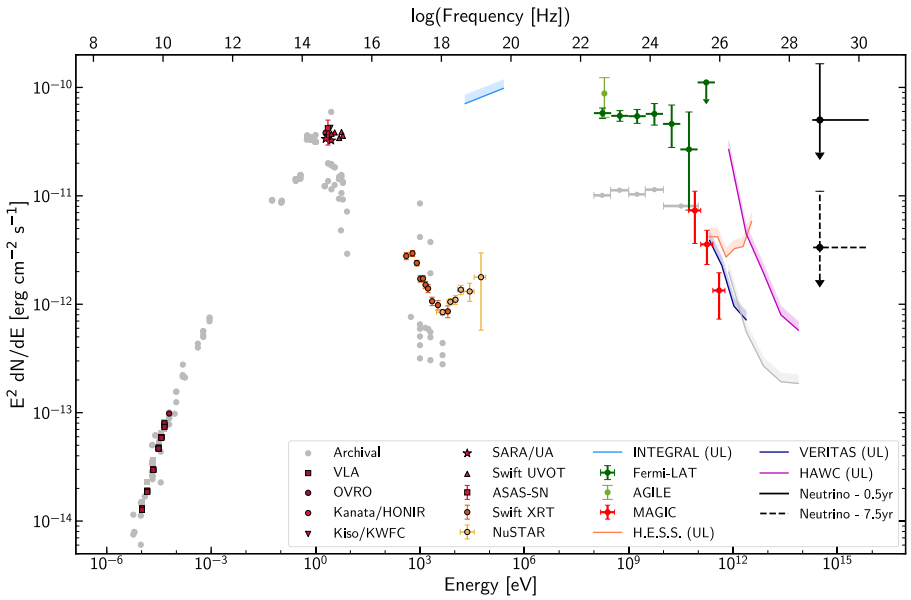

Figure 5.2: Multi-messenger and multi-wavelength observation of TXS 0506+056 around the time of around IceCube-170922A. HAWC limits between September 9, 2017 to October 6, 2017 are shown in purple, and limits from archival data from November 26, 2014 to August 27, 2017 are shown below in grey. Reproduced from [78].

excess, and set the upper-limits for half-decade intervals in energy shown in Figure 5.3.

5.3 Discussion

We searched for VHE gamma-ray emission from two significant neutrino flares by IceCube from the direction of the blazar TXS 0506+056. Thanks to the prompt alert of the detection a high energy neutrino in September 2017, there is data from multiple telescopes across the electromagnetic spectrum for the flare detected around this time. The upper-limits obtained by HAWC are consistent with the detected flux reported by the MAGIC Collaboration.

Contemporaneous electromagnetic data for the ∼150 days neutrino flare found in archival data, starting October 2015, is more scarce. In particular, there are no gamma-ray observations in the VHE regime by IACTs. We searched for emission in archival HAWC data and found no significant excess. By assuming a simple hadronic model with $p\gamma$ interactions and no losses due to intrinsic absorption at the source (see Section 1.4.1) we can infer the gamma-ray emission spectrum based on the observed neutrino emission, fitted to a power law [84], as shown in Figure 5.3. We can see that it is mostly inconsistent with an extrapolation into the HAWC energy range including absorption due to EBL.

However, the inferred gamma-ray spectrum from neutrino observation is not expected to continue as a power law for several decades in energy. The actual spectral energy distribution (SED) depends on the population of protons and target

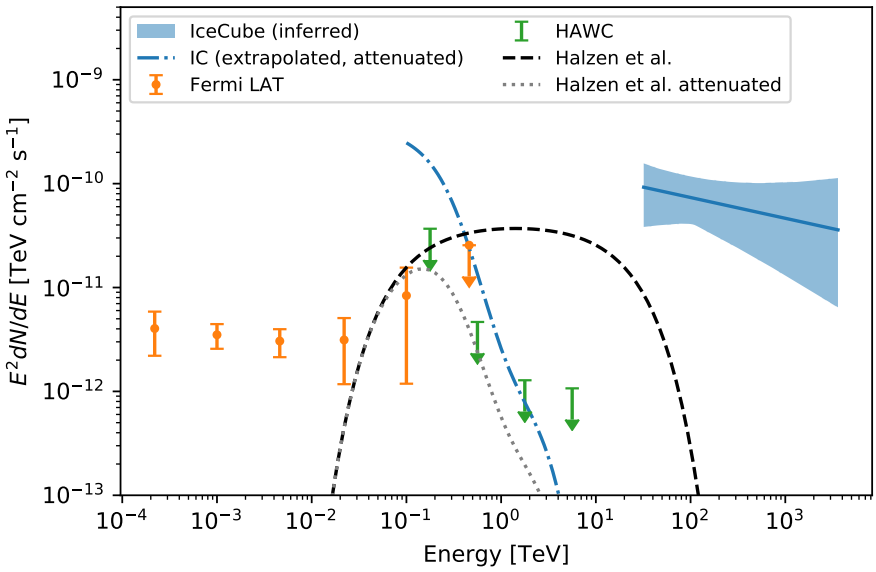

Figure 5.3: HAWC 95 % upper limits on TXS 0506+056 2014-2015 neutrino flare (green). Fermi LAT measurements during this period are shown in orange [85]. The inferred gamma-ray spectrum based on neutrino measurements by IceCube [84] assuming a $p\gamma$ scenario is shown in solid blue. The best fit is extrapolated to the HAWC energy range, attenuated by EBL and shown in a blue dot-dashed line. For reference, we show one of the phenomenological models proposed by Halzen et al. [86]. The black dashed line corresponds to the intrinsic spectrum (after reprocessing) and the gray dotted line is the expected observed spectrum after EBL attenuation.

photons, neither of them straightforward to model. Furthermore, strong neutrino flares such as this one require a large number of target photons, which in turn introduce a large internal attenuation factor for VHE gamma rays [86].

Halzen et al. [86] proposed a phenomenological model consisting of a power law with an index of -2 and a cutoff on both sides, as shown in Figure 5.3. The normalization is set to be consistent with the total energy of the inferred SED —i.e. it assumes no losses after the >30 TeV gamma rays are reprocessed to lower energies by $\gamma\gamma$ interactions. The low energy cutoff was set to 100 GeV based on the observed emission by Fermi-LAT. High-energy cutoffs from 500 GeV to 20 TeV are consistent with Fermi data >10 GeV, although only the latter is shown. HAWC data is also consistent with this description and provides a similar level of constraint.

The full energy range of the Fermi-LAT data cannot be reproduced with this model though. Halzen et al. considered the idea that the emission <10 GeV could be caused by interaction of the emitted photons with the CMB, however this required a value of the Intergalactic Magnetic Field (IGMF) lower than the one measured by Fermi-LAT. The fact that there is no gamma-ray brightening at the time of the neutrino flare represents a challenge for the modeling of this source [87]. Models through *pp* interactions, in which the jet interacts with a dense cloud have been proposed [88], which consider the possibility of observing TeV emissions during this kind of flare for sources at low redshift.

Attenuation by the EBL limits the ability of HAWC to place stronger limits on sources at relatively large redshift such as TXS 0506+056. There is however a clear connection between neutrinos detected by IceCube and gamma rays by HAWC, in

their corresponding energy range, so the possibility of a joint detection remains. The HAWC Collaboration routinely follows up high energy neutrino events, and is analyzing the correlation between integrated VHE gamma-rays and neutrino emission.

Chapter 6: Final remarks: conclusion and future work

We have developed an analysis framework that enables to search and study transient signals in HAWC data of arbitrary timescales. It consists off a maximum likelihood technique which allows to separate the data into multiple analysis bins, each containing events of similar angular resolution and background contamination, and therefore increasing the sensitivity over a simpler cut-and-count analysis. The algorithm implementation was optimized for speed, low resource utilization and robustness in order to be feasible to run using the computer resources at the HAWC site and obtain results with a reasonable latency. This work presented the application of this framework to search for very-high-energy gamma-ray counterparts of gravitational wave events and the candidate neutrino source TXS 0506+056.

We searched for the possible short-duration prompt emission correlated in location and time with gravitational waves detected by LIGO and Virgo between September 12th, 2015 and June 1st, 2019. The sky localization of 18 out of 25 events has at least a partial overlap with the HAWC field of view. The results from all of them are consistent with background expectations. This implies a fluence upper limit for points in the HAWC field of view between 0.1–1 TeV of $2 \times 10^{-7}\,\mathrm{erg\,cm^{-2}}$ to $3 \times 10^{-4}\,\mathrm{erg\,cm^{-2}}$, depending on the event, sky location and timescale.

This null result is however consistent with the low rate of gravitational waves that are expected to be accompanied by a gamma-ray bursts (<1 per year of observations). The source location of the only gravitational wave with a confirmed electromagnetic counterpart, GW170817, was not in the HAWC field of view at the time of the event. We however showed HAWC should otherwise be able to either detect or meaningfully constrain the very-high-energy emission of an event within the binary neutron star merger horizon of current gravitational wave detectors.

We also looked for emission from the blazar TXS 0506+056 around the detection of the high-energy neutrino IceCube-170922A, as well as the neutrino flare identified in an archival search by IceCube between September 2014 and March 2015. Flux upper limits around September, 2017 are consistent with the spectrum measured by the MAGIC telescope. HAWC flux upper bounds on the 2014-2015 neutrino flare extend the Fermi-LAT high-energy limits and provides a similar level of constraint, accounting for attenuation by the extragalactic background light. While this rules out a direct extrapolation of IceCube measurements to the HAWC energy range, it is consistent with the consideration of a break in the spectrum and strong attenuation by the high density of target photons necessary to explain the neutrino flux in photomeson processes.

The applications of this framework naturally extend beyond the ones presented in this work, some of which are already being explored by the HAWC Collaboration. For example, the daily all-sky monitoring and blind search for flares; the study of time-dependent correlations of the AGN measurements by HAWC with x-rays and other wavelengths; and the search for VHE prompt emission from all detected GRBs.

The latter makes use of recent developments in the reconstructions of low energy events (<1 TeV) and divides the data into events landing inside and outside the detector to improve the sensitivity (events inside the array can be better reconstructed than the ones landing outside). These are some of the expected improvements to the analysis presented in this work.

Among other desired improvements for this framework is the ability to perform a real-time all-sky search for bursts. While the implementation has been heavily optimized for speed, it falls short of the requirement for this. Most of the CPU time is spent looping through the pixels in the map, which cannot be further optimized and requires a change of strategy. One possibility is to do an unbinned analysis, looping through the individual events instead, whose numbers for ∼1 s timescales are lower than the number of pixels. This has been explored and besides being feasible to implement would bring a ∼10 % improvement in sensitivity. An unbinned analysis is however not fast enough for the speed requirements of a real-time all-sky analysis, the path forward seems to be to reduce the searched locations based on a preliminary cut-and-count analysis such as the one currently in place [63].

The detection of the VHE gamma-ray emission of transients associated with gravitational waves and neutrino events is challenging. However, as we have shown in this work, our studies suggest that in the future HAWC can play an important role in their multi-wavelength and multi-messenger picture.

The identification of transients correlated in time has played a fundamental role in multi-messenger observations. Wide-field-of-view instruments are expected to keep playing an important role in making them possible. The methods described

in this work are of general applicability and can help to improve the sensitivity of future instruments.

Appendix A: Simulation weighting

The goal of weighting simulation events is to mimic the distribution of energy, core location an direction expected from a real source from the corresponding unphysical distribution described in Section 2.8. These distributions are $\Psi(E)$, $R(r)$ and $Z(\theta)$, were E stands for energy, r is the distance from the center of the detector and θ is the zenith angle. Note that events are thrown symmetrically in azimuth. This distributions are normalized such that

$$\int \Psi(E)R(r)Z(\theta)\ dA\ d\theta\ d\phi\ dE = 1\,, \tag{A.1}$$

where A stands for area in the ground and ϕ for azimuth. We typically want to compute the rate of observed events dN/dt for a given spectrum $\Phi(E)$, that is

$$\frac{dN}{dt} = \int \Phi(E)\cos\theta\sin\theta dA d\theta d\phi dE\,, \tag{A.2}$$

where $\cos\theta$ comes from the dot product of the incoming direction of the shower and the differential area of the detector, and the $\sin\theta$ from the solid angle differential area.

First, note that using a sample $\{x_1 \ldots x_N\}$ obtained from a probability distribution $f(x)$, and a weighting function $w(x)$, we have

$$\int w(x)f(x)dx = \langle w(x)f(x)\rangle \approx \frac{1}{N}\sum_{i=1}^{N} w(x_i)\,, \tag{A.3}$$

that is, we can approximate the weighted average of $f(x)$ by taking the average of the weighted function at locations randomly sampled from the $f(x)$ distribution.

In our case we randomly thrown N_t events that have an energy E_i, distance to the center r_i and zenith angle θ_i, therefore for a general weighting function of this parameters $w(E_i, r_i, \theta_i)$ we have

$$\frac{1}{N_t}\sum_{i=1}^{N_t} w(E_i, r_i, \theta_i) \approx \int w(E, r, \theta)\Psi(E)R(r)Z(\theta)\ dA\ d\theta\ d\phi\ dE\,, \tag{A.4}$$

We can then compare Eq.A.4 to Eq. A.2 and see that we can choose $w(E, r, \theta)$ such that the right-hand side of both equations match, that is

$$w(E, r, \theta) = \frac{\Phi(E)}{\Psi(E)}\frac{\cos\theta\sin\theta}{Z(\theta)}\frac{1}{R(r)}\,, \tag{A.5}$$

and then can compute dN/dt by summing the weight for each thrown event that passed our cuts:

$$\frac{dN}{dt} \approx \frac{1}{N_t}\sum_{i=1}^{N_t} w(E_i, r_i, \theta_i)\,. \tag{A.6}$$

Appendix B: Fast flux normalization fit

In Section 3.3 it was discussed the maximum likelihood forward folding analysis use in this work to physical source parameters, such as localization and spectral index. In general the problem consists in maximizing this function

$$\mathcal{L}\left(\mathbf{a};\mathbf{d}\right) = \prod_i \frac{\left(b_i + s_i(\mathbf{a})\right)^{d_i} \exp\left(-b_i - s_i(\mathbf{a})\right)}{d_i!}\,, \tag{B.1}$$

where $\mathbf{d}$ is the set of counts observed and $b_i + s_i(\mathbf{a})$ is the counts that are expected given a set of free parameters $\mathbf{a}$; b_i is the estimated the background counts and s_i the expected signal counts. This is the same as Eq. 3.6 but we've flattened the indices. Also in Section 3.3 it was discussed how we can test whether the hypothesis testing by comparing the maximum likelihoods of two different nested hypothesis, for which we define a test statistic (see Eq. 3.8)

$$TS = 2\log\frac{\mathcal{L}(\hat{\mathbf{b}};\mathbf{d})}{\mathcal{L}(\hat{\mathbf{a}};\mathbf{d})}\,, \tag{B.2}$$

where $\hat{\mathbf{a}}$ and $\hat{\mathbf{b}}$ is the set of parameters that maximize the likelihood for the null and alternative hypothesis, respectively. While this works in general, a very common scenario is to test for the presence of a source against the background-only null hypothesis with the flux normalization as the only free parameter. This is for example performed extensively during a blind search. It is then of special interest

to find a way to optimize the algorithm for this case. Furthermore, even minimizing algorithms for more parameters can be improved if for a given set of parameters the flux normalization minimization can be performed quickly.

For the background-only null hypothesis leaving only the flux normalization as free parameter $s_i(\mathbf{a})$ can be expressed as $e_i f$, where f is the flux normalization and e_i are a series of constants corresponding to the expected excess per unit flux in a given analysis bin and pixel. The null hypothesis is then simply $f = 0$. This simplification will allow us to study analytically the properties of the likelihood function, and justify the use of Newton's method to maximize it.

While one of the simplest minimization algorithms, Newton's method is also very fast converging. It is however seldom used by itself since its convergence can strongly depend on the initial estimate: if it is not near the solution the algorithm can overshoot and diverge, can get trapped in a stationary point or converge to a local maximum. We will show however that the method applied to this case is very robust.

We begin with our test statistic, simplified to

$$\begin{aligned} TS(f) &= 2\log\frac{\mathcal{L}(f;\mathbf{d})}{\mathcal{L}(f=0;\mathbf{d})} \\ &= 2\sum\log\frac{(b_i+e_if)^{d_i}\exp\left(-b_i-e_if\right)}{d_i!} - 2\sum\log\frac{b_i^{d_i}\exp\left(-b_i\right)}{d_i!} \\ &= 2\sum\log\frac{(b_i+e_if)^{d_i}\exp\left(-e_if\right)}{b_i^n} \\ &= 2\sum\left(d_i\frac{b_i+e_if}{b_e} - e_if\right) . \end{aligned} \tag{B.3}$$

First, note that we can compute any derivative analytically

$$\begin{aligned} TS'(f) &= 2\sum\left(d_i\frac{e_i}{b_i+e_if}-e_i\right) \\ TS''(f) &= -2\sum\left(d_i\frac{e_i^2}{(b_i+e_if)^2}\right) \\ TS^{n>1}(f) &= (-2)^{n-1}\sum\left(d_i\frac{e_i^n}{(n-1)!(b_i+e_if)^n}\right)\,, \end{aligned} \tag{B.4}$$

Then, note that the second derivative is always negative, which means that $TS'(f)$ is monotonically decreasing. As a consequence it can only have a single root, and therefore $TS(f)$ can only have one maximum, the global maximum. In general, an even derivative is always negative and an odd derivative always positive, except for the first derivative, which flips sign once at the root.

The Taylor expansion of $TS'(f)$ around f_0 is

$$TS'(f) = \sum_{m=0}^{\infty}\frac{TS^{m+1}(f_0)}{m!}(f-f_0)^m\,. \tag{B.5}$$

And the iteration step in the Newton's method is

$$f_{n+1} = f_n - \frac{TS'(f_n)}{TS''(f_n)}\,. \tag{B.6}$$

Expanding around f_n and evaluating at f_{n+1} we have

$$\begin{aligned} TS'(f_{n+1}) &= \sum_{m=0}^{\infty}\frac{TS^{m+1}(f_n)}{m!}\left(f_{n+1}-f_n\right)^m \\ &= \sum_{m=0}^{\infty}\frac{TS^{m+1}(f_n)}{m!}\left(-\frac{TS'(f_n)}{TS''(f_n)}\right)^m\,. \end{aligned} \tag{B.7}$$

It follows that as long as at the starting point $TS'(f_0)$ is positive, then all $TS'(f_n)$ will remain positive and convergence is guaranteed. This is graphically

depicted in Figure B.1. Lastly, since we are only interested in positive physical values of f we can always start at $f_0 = 0$ and check the sign of $TS'(0)$. If positive, the minimization will converge; if negative, we can stop the algorithm as we are sure the solution is unphysical.

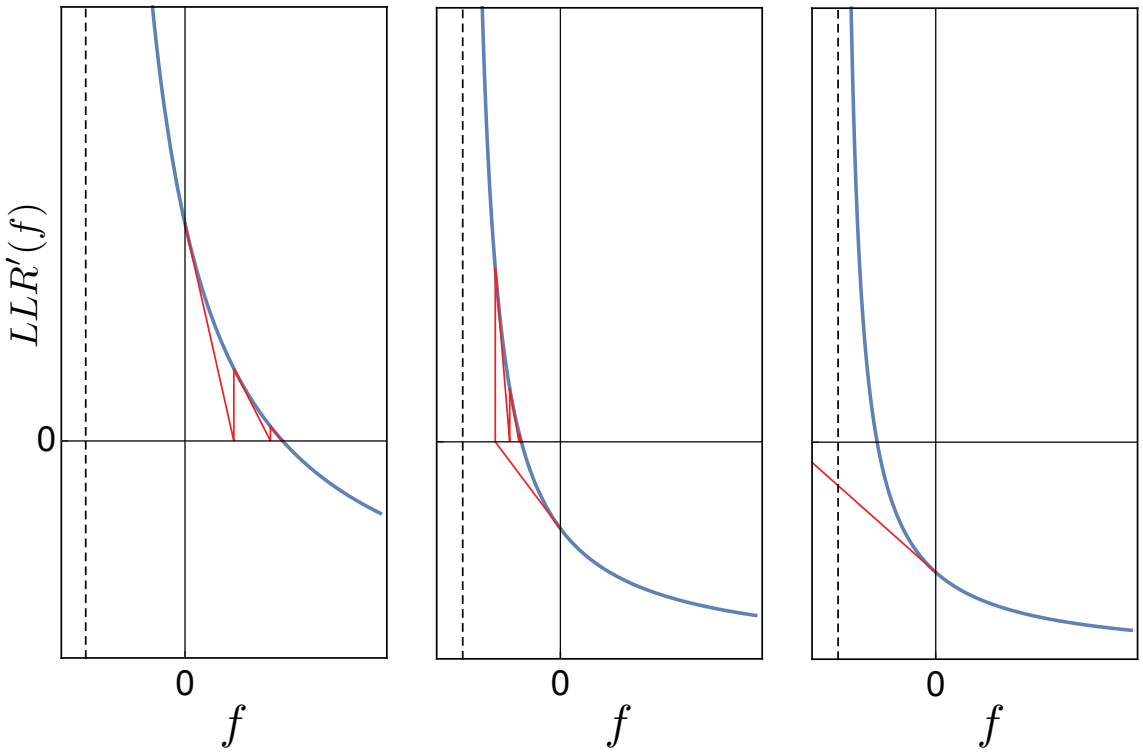

Figure B.1: Graphically, the Newton algorithm approximate $TS'(f)$ by its tangent line and finds the intersection with the x-axis. As explained in the text, $TS'(f)$ always has the same general shape, and convergence is guaranteed starting at $f_0 = 0$ as long as the solution is positive, as it the first case (from left to right). Otherwise, the algorithm can diverge into a region where $TS(f)$ is undefined, as in the last case.

Appendix C: Optimal cut calculation

A very common task is to find the optimal cut or integration bin such that you keep as much signal and remove as much background as possible, thus increasing your sensitivity. Here are some of such calculation mentioned in this work.

C.1 Optimal radius given a Gaussian PSF

Assume a flat background and a PSF of the form

$$PSF(r,\theta) = \frac{N}{2\pi\sigma^2}\exp\left(-\frac{r^2}{2\sigma^2}\right), \tag{C.1}$$

where r is the angular distance from the source, θ the azimuthal angle, σ is a constant and N is the normalization. Assuming we are in the Gaussian regime, in a cut-and-count analysis the significance of a detection is

$$\begin{aligned} s(R) &= \frac{S}{\sqrt{B}} \\ &= \frac{N\int_0^R \exp\left(-\frac{r^2}{2\sigma^2}\right) r dr}{\sigma^2\sqrt{2\pi\int_0^R brdr}} \\ &= \frac{N\left(1-\exp\left(-\frac{R^2}{2\sigma^2}\right)\right)}{\sqrt{\pi}bR}, \end{aligned} \tag{C.2}$$

where R is the radius of integration. Numerically solving for $s'(R) = 0$ we find that the optimal radius is $R_{opt} = 1.585\sigma$, and $s(R_{opt}) = 0.254N/\sigma\sqrt{b}$.

If instead of a cut-and-count analysis we divide the sky into small pixels and sum the squares of the contribution of each independently, including the tails, in the limit of infinitesimally small pixels the significance is

$$\begin{aligned} s_{max} &= \sqrt{2\pi \int_0^\infty \frac{S(r)^2}{B(r)} r dr} \\ &= \sqrt{2\pi \int_0^\infty \frac{\left(\frac{N}{2\pi\sigma^2} \exp\left(-\frac{r^2}{2\sigma^2}\right)\right)^2}{b} r dr} \\ &= \frac{N}{2\sigma\sqrt{\pi b}} \,. \end{aligned} \tag{C.3}$$

We thus gain $s_{max}/s(R_{opt}) - 1 = 10\%$ in sensitivity by using the PSF and consider the tails, assuming the PSF is indeed Gaussian.

C.2 Optimal time window for a Gaussian signal

Given a constant background rate and signal distributed in time as

$$f(t) \propto \exp\left(-\frac{t^2}{2\sigma^2}\right) , \tag{C.4}$$

where σ is a constant, we want to compute the optimal time window over which we integrate the signal.

Assuming we are in the Gaussian regime, the significance of the detection is

$$\begin{aligned} s(dt) &= \frac{S}{\sqrt{B}} \\ &\propto \frac{\int_{-\delta t/2}^{\delta t/2} f(t)\ \delta t}{\sqrt{\int_{-\delta t/2}^{\delta t/2} b\ dt}} \,, \\ &= \frac{\sqrt{2\pi}\sigma \mathrm{erf}\left(\frac{\delta t}{2\sqrt{2}\sigma}\right)}{\sqrt{b dt}} \end{aligned} \tag{C.5}$$

where dt is the time windows width and b is the background rate. Using the change of variable $\delta t' = \delta t/\sigma$ and numerically solving $s'(\delta t') = 0$, the significance is maximized when $\delta t = 2.8\sigma$, which integrates 84 % of the signal.

Bibliography

[1] P. Morrison. On gamma-ray astronomy. *Il Nuovo Cimento (1955-1965)*, 7(6):858–865, Mar 1958.

[2] D. J. Thompson. Space detectors for gamma rays (100 MeV-100 GeV): From EGRET to Fermi LAT. *Comptes Rendus Physique*, 16:600–609, August 2015.

[3] F. Schmidt and J. Knapp. Corsika shower images. 2005.

[4] M. de Naurois and L. Rolland. A high performance likelihood reconstruction of γ-rays for imaging atmospheric Cherenkov telescopes. *Astroparticle Physics*, 32:231–252, December 2009.

[5] United States Committee on Extension to the Standard Atmosphere. *U.S. standard atmosphere, 1976*. National Oceanic and Amospheric [sic] Administration : for sale by the Supt. of Docs., U.S. Govt. Print. Off., 1976.

[6] K. Kamata and J. Nishimura. The Lateral and the Angular Structure Functions of Electron Showers. *Progress of Theoretical Physics Supplement*, 6:93–155, 1958.

[7] K. Greisen. Cosmic Ray Showers. *Annual Review of Nuclear and Particle Science*, 10:63–108, 1960.

[8] P.K.F. Grieder. *Extensive Air Showers: High Energy Phenomena and Astrophysical Aspects - A Tutorial, Reference Manual and Data Book*. Astrophysics and space science library. Springer Berlin Heidelberg, 2010.

[9] Planck Collaboration et al. Planck 2018 results. VI. Cosmological parameters. *arXiv e-prints*, July 2018.

[10] A. G. Riess, S. Casertano, W. Yuan, L. M. Macri, and D. Scolnic. Large Magellanic Cloud Cepheid Standards Provide a 1% Foundation for the Determination of the Hubble Constant and Stronger Evidence for Physics beyond ΛCDM. *The Astrophysical Journal*, 876:85, May 2019.

[11] R. C. Gilmore et al. Semi-analytic modelling of the extragalactic background light and consequences for extragalactic gamma-ray spectra. *Monthly Notices of the Royal Astronomical Society*, 422:3189–3207, June 2012.

[12] C. M. Urry and P. Padovani. Unified Schemes for Radio-Loud Active Galactic Nuclei. *Publications of the Astronomical Society of the Pacific*, 107:803, September 1995.

[13] G. Fossati et al. Multiwavelength Observations of Markarian 421 in 2001 March: An Unprecedented View on the X-Ray/TeV Correlated Variability. *Astrophysical Journal*, 677:906–925, April 2008.

[14] Ahnen, M. L. et al. Long-term multi-wavelength variability and correlation study of markarian 421 from 2007 to 2009. *A&A*, 593:A91, 2016.

[15] A. A. Abdo et al. Fermi Large Area Telescope Observations of Markarian 421: The Missing Piece of its Spectral Energy Distribution. *The Astrophysical Journal,*, 736:131, August 2011.

[16] Lorenzo Sironi, Maria Petropoulou, and Dimitrios Giannios. Relativistic jets shine through shocks or magnetic reconnection? *Monthly Notices of the Royal Astronomical Society*, 450(1):183–191, 04 2015.

[17] T.K. Gaisser. *Cosmic Rays and Particle Physics*. Cambridge University Press, 1990.

[18] K. Murase, Y. Inoue, and C. D. Dermer. Diffuse neutrino intensity from the inner jets of active galactic nuclei: Impacts of external photon fields and the blazar sequence. *Physical Review D*, 90(2):023007, July 2014.

[19] Markus Boettcher. Progress in multi-wavelength and multi-messenger observations of blazars and theoretical challenges. *Galaxies*, 7(1), 2019.

[20] R. W. Klebesadel, I. B. Strong, and R. A. Olson. Observations of Gamma-Ray Bursts of Cosmic Origin. *The Astrophysical Journal*, 182:L85, June 1973.

[21] P. Narayana Bhat et al. THE THIRDFERMIGBM GAMMA-RAY BURST CATALOG: THE FIRST SIX YEARS. *The Astrophysical Journal Supplement Series*, 223(2):28, apr 2016.

[22] M. Ackermann et al. THE FIRSTFERMI-LAT CATALOG OF SOURCES ABOVE 10 GeV. *The Astrophysical Journal Supplement Series*, 209(2):34, nov 2013.

[23] M. Ackermann et al. Fermi-lat observations of the gamma-ray burst grb 130427a. *Science*, 343(6166):42–47, 2014.

[24] R. Atkins et al. *The Astrophysical Journal*, 533(2):L119–L122, apr 2000.

[25] Razmik Mirzoyan. First time detection of a grb at sub-tev energies; magic detects the grb 190114c. The Astronomer's Telegraph, 2019.

[26] Edna Ruiz-Velasco. Discovery of late-time vhe emission from a gamma-ray burst afterglow by h.e.s.s. CTA Science Symposium, 2019.

[27] D. A. Frail et al. Beaming in Gamma-Ray Bursts: Evidence for a Standard Energy Reservoir. *The Astrophysical Journal*, 562:L55–L58, November 2001.

[28] P. Mészáros. The Fireball Model of Gamma-Ray Bursts. *Progress of Theoretical Physics Supplement*, 143:33–49, 2001.

[29] Hjorth Jens. *Gamma-ray Bursts. The Gamma-Ray Burst - Supernova Connection.* Cambridge Astrophysics. Cambridge University Press, 2012.

[30] A. S. Fruchter et al. Long γ-ray bursts and core-collapse supernovae have different environments. *Nature*, 441:463–468, May 2006.

[31] B. Paczynski. Gamma-ray bursters at cosmological distances. *The Astrophysical Journal Letters*, 308:L43–L46, September 1986.

[32] D. Eichler, M. Livio, T. Piran, and D. N. Schramm. Nucleosynthesis, neutrino bursts and gamma-rays from coalescing neutron stars. *Nature*, 340:126–128, July 1989.

[33] Krzysztof Belczynski et al. A study of compact object mergers as short gamma-ray burst progenitors. *The Astrophysical Journal*, 648(2):1110–1116, sep 2006.

[34] B. P. Abbott et al. Multi-messenger observations of a binary neutron star merger. *The Astrophysical Journal*, 848(2):L12, oct 2017.

[35] B. D. Metzger and E. Berger. What is the Most Promising Electromagnetic Counterpart of a Neutron Star Binary Merger? *The Astrophysical Journal*, 746:48, February 2012.

[36] Michele Maggiore. *Gravitational waves.* Oxford Univ. Press, Oxford, 2008.

[37] IceCube Collaboration. Evidence for High-Energy Extraterrestrial Neutrinos at the IceCube Detector. *Science*, 342:1242856, November 2013.

[38] M. G. Aartsen et al. Multimessenger observations of a flaring blazar coincident with high-energy neutrino IceCube-170922A. *Science*, 361:eaat1378, July 2018.

[39] B. P. Abbott et al. Observation of Gravitational Waves from a Binary Black Hole Merger. *Physical Review Letters*, 116(6):061102, February 2016.

[40] B. P. Abbott et al. Prospects for observing and localizing gravitational-wave transients with Advanced LIGO, Advanced Virgo and KAGRA. *Living Reviews in Relativity*, 21:3, April 2018.

[41] J. Veitch et al. Parameter estimation for compact binaries with ground-based gravitational-wave observations using the LALInference software library. *PHYSICAL REVIEW D*, 91(4):042003, February 2015.

[42] V. Kalogera and G. Baym. The Maximum Mass of a Neutron Star. *The Astrophysical Journal Letters*, 470:L61, October 1996.

[43] W. M. Farr et al. The Mass Distribution of Stellar-mass Black Holes. *The Astrophysical Journal*, 741:103, November 2011.

[44] T. B. Littenberg, B. Farr, S. Coughlin, V. Kalogera, and D. E. Holz. Neutron Stars versus Black Holes: Probing the Mass Gap with LIGO/Virgo. *The Astrophysical Journal Letters*, 807:L24, July 2015.

[45] R. Perna, M. Chruslinska, A. Corsi, and K. Belczynski. Binary black hole mergers within the LIGO horizon: statistical properties and prospects for detecting electromagnetic counterparts. *Monthly Notices of the Royal Astronomical Society*, 477:4228–4240, July 2018.

[46] LIGO Collaboration. Advanced LIGO. *Classical and Quantum Gravity*, 32(7):074001, mar 2015.

[47] L. S. Finn and D. F. Chernoff. Observing binary inspiral in gravitational radiation: One interferometer. *Physical Review D*, 47:2198–2219, March 1993.

[48] B. Kiziltan, A. Kottas, M. De Yoreo, and S. E. Thorsett. The Neutron Star Mass Distribution. *The Astrophysical Journal*, 778:66, November 2013.

[49] J. Abadie et al. TOPICAL REVIEW: Predictions for the rates of compact binary coalescences observable by ground-based gravitational-wave detectors. *Classical and Quantum Gravity*, 27(17):173001, September 2010.

[50] Hamamatsu Photonics. Photomultiplier tubes: basics and applications. 20107.

[51] Hamamatsu Photonics. Large photocathode area photomultiplier tubes. 2016.

[52] George M. Hale and Marvin R. Querry. Optical constants of water in the 200-nm to 200-μm wavelength region. *Appl. Opt.*, 12(3):555–563, Mar 1973.

[53] HAWC Collaboration. Measurement of the Crab Nebula at the Highest Energies with HAWC. *arXiv e-prints*, May 2019.

[54] A. U. Abeysekara et al. Observation of the crab nebula with the HAWC gamma-ray observatory. *The Astrophysical Journal*, 843(1):39, jun 2017.

[55] Zhixiang Ren. *Improve the Low Energy Sensitivity of the HAWC Observatory*. PhD thesis, The University of New Mexico, 12 2018.

[56] A. U. Abeysekara et al. All-sky measurement of the anisotropy of cosmic rays at 10 TeV and mapping of the local interstellar magnetic field. *The Astrophysical Journal*, 871(1):96, jan 2019.

[57] A. U. Abeysekara et al. Constraining the $\overline{p}/p$ ratio in tev cosmic rays with observations of the moon shadow by hawc. *Phys. Rev. D*, 97:102005, May 2018.

[58] A. U. Abeysekara et al. Observation of anisotropy of TeV cosmic rays with two years of HAWC. *The Astrophysical Journal*, 865(1):57, sep 2018.

[59] D. Heck et al. *CORSIKA: a Monte Carlo code to simulate extensive air showers.* February 1998.

[60] S. Agostinelli et al. Geant4 - a simulation toolkit. *Nuclear Instruments and Methods in Physics Research A*, 506:250–303, July 2003.

[61] P. W. Younk et al. A high-level analysis framework for HAWC. *arXiv e-prints*, August 2015.

[62] A. U. Abeysekara et al. Daily Monitoring of TeV Gamma-Ray Emission from Mrk 421, Mrk 501, and the Crab Nebula with HAWC. *The Astrophysical Journal Letters*, 841:100, June 2017.

[63] J. Wood. An All-Sky Search for Bursts of Very High Energy Gamma Rays with HAWC. *arXiv e-prints*, January 2018.

[64] J. Wood. Results from the first one and a half years of the HAWC GRB program. *arXiv e-prints*, January 2018.

[65] R. Alfaro et al. Search for very-high-energy emission from gamma-ray bursts using the first 18 months of data from the HAWC gamma-ray observatory. *The Astrophysical Journal*, 843(2):88, jul 2017.

[66] K. M. Gorski et al. HEALPix: A framework for high-resolution discretization and fast analysis of data distributed on the sphere. *The Astrophysical Journal*, 622(2):759–771, apr 2005.

[67] R. Atkins et al. Observation of TeV gamma rays from the crab nebula with milagro using a new background rejection technique. *The Astrophysical Journal*, 595(2):803–811, oct 2003.

[68] S. S. Wilks. The large-sample distribution of the likelihood ratio for testing composite hypotheses. *Ann. Math. Statist.*, 9(1):60–62, 03 1938.

[69] G. J. Feldman and R. D. Cousins. Unified approach to the classical statistical analysis of small signals. *Physical Review D*, 57:3873–3889, April 1998.

[70] B. P. Abbott et al. GWTC-1: A Gravitational-Wave Transient Catalog of Compact Binary Mergers Observed by LIGO and Virgo during the First and Second Observing Runs. *arXiv e-prints*, November 2018.

[71] M. Ajello et al. A decade of gamma-ray bursts observed by fermi-LAT: The second GRB catalog. *The Astrophysical Journal*, 878(1):52, jun 2019.

[72] A. Goldstein et al. An Ordinary Short Gamma-Ray Burst with Extraordinary Implications: Fermi-GBM Detection of GRB 170817A. *The Astrophysical Journal Letters*, 848:L14, October 2017.

[73] J. Abadie et al. TOPICAL REVIEW: Predictions for the rates of compact binary coalescences observable by ground-based gravitational-wave detectors. *Classical and Quantum Gravity*, 27(17):173001, September 2010.

[74] Z.-P. Jin et al. Short GRBs: Opening Angles, Local Neutron Star Merger Rate, and Off-axis Events for GRB/GW Association. *The Astrophysical Journal*, 857:128, April 2018.

[75] Y.-C. Zou et al. Determining the Lorentz Factor and Viewing Angle of GRB 170817A. *The Astrophysical Journal Letters*, 852:L1, January 2018.

[76] NASA. Swift grb table. 2019.

[77] Fermi-LAT Collaboration. Fermi-LAT observations of the LIGO/Virgo event GW170817. *arXiv e-prints*, October 2017.

[78] IceCube Collaboration et al. Multimessenger observations of a flaring blazar coincident with high-energy neutrino IceCube-170922A. *Science*, 361:eaat1378, July 2018.

[79] Erick Blaufuss and Claudio Kopper. Icecube-170922a - icecube observation of a high-energy neutrino candidate event. 2017.

[80] S. Paiano, R. Falomo, A. Treves, and R. Scarpa. The Redshift of the BL Lac Object TXS 0506+056. *The Astrophysical Journal Letters*, 854:L32, February 2018.

[81] Y. Tanaka, S. Buson, and D. Kocevski. Fermi-lat detection of increased gamma-ray activity of txs 0506+056, located inside the icecube-170922a error region. 2017.

[82] S. Ansoldi et al. The Blazar TXS 0506+056 Associated with a High-energy Neutrino: Insights into Extragalactic Jets and Cosmic-Ray Acceleration. *The Astrophysical Journal Letters*, 863:L10, August 2018.

[83] VERITAS Collaboration et al. VERITAS Observations of the BL Lac Object TXS 0506+056. *The Astrophysical Journal Letters*, 861:L20, July 2018.

[84] IceCube Collaboration et al. Neutrino emission from the direction of the blazar TXS 0506+056 prior to the IceCube-170922A alert. *Science*, 361:147–151, July 2018.

[85] Fermi-LAT collaboration et al. Investigation of two Fermi-LAT gamma-ray blazars coincident with high-energy neutrinos detected by IceCube. *arXiv e-prints*, January 2019.

[86] F. Halzen, A. Kheirandish, T. Weisgarber, and S. P. Wakely. On the Neutrino Flares from the Direction of TXS 0506+056. *The Astrophysical Journal Letters*, 874:L9, March 2019.

[87] X. Rodrigues, S. Gao, A. Fedynitch, A. Palladino, and W. Winter. Lepto-hadronic Blazar Models Applied to the 2014-2015 Flare of TXS 0506+056. *The Astrophysical Journal Letters*, 874:L29, April 2019.

[88] K. Wang, R.-Y. Liu, Z. Li, X.-Y. Wang, and Z.-G. Dai. Jet-cloud/star interaction as an interpretation of neutrino outburst from the blazar TXS 0506+056. *arXiv e-prints*, September 2018.